Institut für Robotik und Mechatronik	BJ.: 2015
	IB.Nr.: 572-2015/34

DIPLOMARBEIT

MODELING AND CONTROL OF A FLEXIBLE STRUCTURE FOR ROBOTIC SURGERY

Freigabe:	Der Bearbeiter:	Unterschriften
	David Fehrenbach	
	Betreuer:	
	Dipl.-Ing. Bastian Deutschmann	
	Der Institutsdirektor	
	Dr. Alin Albu-Schäffer	

Dieser Bericht enthält 81 Seiten, 42 Abbildungen und 11 Tabellen

Ort: Oberpfaffenhofen	Datum:	Bearbeiter:	Zeichen:

Technische Universität München

MedTech
Lehrstuhl für Medizintechnik

Masters-Thesis

by Mr Cand.-Ing. David Fehrenbach

Student Number: 3608626

Discipline: Mechanical Engineering

Modelling and Control of a Flexible Structure for Robotic Surgery

Supervisor:
Dipl.-Ing. Andreas Robeck
Partner:
Dipl.-Ing. Bastian Deutschmann
issued: 01.10.2014
submitted: 31.03.2015

Name Surname

Name Surname

MedTech Lehrstuhl für Medizintechnik der TU München, Prof. Dr. med. Dr.-Ing. habil. Erich Wintermantel
Boltzmannstrasse 15, 85748 Garching, Telefon +49 (0)89 289 16701, Telefax +49 (0)89 289 16702,
http://www.medtech.mw.tum.de

20 keywords:

classical beam theory, Euler-Bernoulli beam theory, Timoshenko beam theory, continuous robots, compliant mechanism, MIRS, NOTES, endoscopic surgery, catheterize, larygeal surgery, dynamic analysis, static analysis, influence of shear, constant curvature, elastomer, material testing, finite element model, Frenet-Serret, position controller, tendon routing

This thesis has not been published previously in its entirety or in part for obtaining any qualification neither in-country nor offshore.

By submitting this thesis, I declare that the entirety of the work contained therein is my own, original work, that I am the sole author thereof (save to the extent explicitly otherwise stated). A violation of this rule may result in legal consequences.

Garching, March 31, 2015

Name Surname

MedTech Lehrstuhl für Medizintechnik der TU München, Prof. Dr. med. Dr.-Ing. habil. Erich Wintermantel
Boltzmannstrasse 15, 85748 Garching, Telefon +49 (0)89 289 16701, Telefax +49 (0)89 289 16702,
http://www.medtech.mw.tum.de

Abstract

Introduction Tongues and other mammalian organs are composed almost entirely out of muscles that realize motion such as bending, extension and torsion in a highly complex way. Within the robotic context, such structures are called continuous robots. They consist of a continuum that provides structural support and flexibility necessary for motion at the same time. The necessary actuators are placed in a certain pattern around them, depending on their type and properties. We assumed that planar motion of such a continuum can be modelled as the transverse motion of an elastic beam by the use of the classical beam theories. In the present work, we aimed to investigate those beam theories, built up a testbed with a compliant mechanism and, furthermore, implement a position controller to command the transverse motion.

Methods The equations of motions for the Euler-Bernoulli and Timoshenko beam theory were established using the Lagrangian formalism and solved analytically. As a proof, a modal analysis using the finite element method was carried out. The kinematics to describe the mechanism's tip position for a concentrated tip moment were described using differential geometry. To verify the results, a testbed was built up consisting of a compliant mechanism and actuators which allowed the introduction of a moment or a transverse shear force at the mechanism's tip. The compliant mechanism itself was designed in a way, that we were able to observe a significant difference between the two beam theories. We used silicone as the material of the mechanism's continuum. To investigate the elastic properties of this elastomer, we conducted standardised and modified material tests, such as the compression or 3-point-bending test.

results Within the material tests, the Young's modulus showed a non-linear behaviour, while the Poisson's ratio was found to be a constant. The accuracy of the tip angle using the Timoshenko theory and those material parameters never exceeded an error of 2% for the actuation via tip moment. Using the constant curvature approximation, we achieved a tip position accuracy with a maximum error of 4% for the lateral deflection and 12% for the axial compression of the mechanism. With higher pretension in the tendons, the results lost accuracy. By the use of the proposed position controller, we achieved an accuracy of 22% for a commanded tip angle.

discussion We aimed to built up a testbed for a continuous robot and proofed accuracy for the tip angle and lateral position using the Timosehnko theory. In x-direction, the accuracy was lower. The reasons for those inaccuracy were found to be geometrical non-linearities resulting from the loading condition in the testbed, tendon elasticity and friction.

Conclusion Further steps are investigations concerning tendon elasticity and friction to improve accuracy of the position controller. As well, one should consider the use of the exact or Cosserat beam theory to include the undefined load case which was found to have influence for higher deflections.

Danksagung

Meine Dankbarkeit gilt in größtem Maße Prof. Dr. Dr. Erich Wintermantel, der durch sein Engagement mein Interesse für die Medizintechnik geweckt hat. Durch ihn wurde mir die Möglichkeit zuteil, in Kooperation mit dem Lehrstuhl für Medizintechnik der TU München diese Abschlussarbeit zu verfassen.

Gleichermaßen danke ich Prof. Dr. Alin Albu-Schäffer, Leiter des Instituts für Robotik und Mechatronik des Deutschen Zentrums für Luft- und Raumfahrt in Oberpfaffenhofen, für die Möglichkeit, in der Medizintechnikgruppe forschen zu dürfen.

Besonders bedanken möchte ich mich bei meinem persönlichen Betreuer, Dipl.-Ing. Bastian Deutschmann für die Überwachung und Korrektur meiner Arbeit. Sein großes Engagement hat maßgeblich zum Gelingen dieser Arbeit beigetragen. Entscheidende Ideen wurden gemeinschaftlich erarbeitet, diskutiert und umgesetzt. Zu jeder Zeit stand er mir unterstützend zur Seite. Weiterhin bedanke ich mich bei Dipl.-Ing. Andreas Robeck für die Korrektur und Koordination der Arbeit von seiten des Lehrstuhls.

Ich möchte mich recht herzlich bei Jens Reinecke und Bernhard Vodermayer für ihre stets freundliche Unterstützung und Hilfbereitschaft in Fragen zur Mechanik, zum 3D-Druck und zur Kunststoffverarbeitung bedanken.

Die hervorragende handwerkliche Kompetenz der beteiligten Werkstätten war in großem Maße für das Gelingen dieser Arbeit verantwortlich. Dort, wo das Verständnis des angehenden Ingenieurs endete, waren die Mitarbeiter der institutsinternen Werkstätten mit Rat und Tat aus langjähriger Berufserfahrung immer zur Stelle.

Außerdem möchte ich allen Studentinnen und Studenten, Kolleginnen und Kollegen innerhalb der Forschungsgruppe für die Unterstützung, Freundschaft und Aufmunterung in allen Phasen der Arbeit danken.

Besonders großer Dank gilt meinen Eltern und meiner Familie, die mich finanziell und wichtiger noch, moralisch während meiner Studienzeit unterstützt und aufgebaut haben.

Zuletzt spreche ich meinen Dank meiner Freundin Anna Hin aus, die meinen Weg stets begleitet hat. In allen Situationen konnte ich mich auf ihre Hilfe verlassen, was nicht zuletzt zum Gelingen dieser Arbeit beigetragen hat.

Glossary

CC constant curvature. 13, 33, 34, 39, 57, 63–65, 67, 73, 74, 79–81

DOF degrees of freedom. 10, 18, 19

EAP electro active polymers. 6

FEM finite element method. 37, 38, 81

FTE force transmission error. 49–51

IR infra-red. 44

MIRS minimally invasive robotic surgery. 2, 5, 10, 11

NOTES natural orifice translumeal endoscopic surgery. 10, 11

ODE ordinary differential equation. 17, 20, 21

SDE shear deformation error. 31–33, 70, 71, 81

SMA shape memory alloy. 6, 10

TCP tool center point. 44

Contents

1 Introduction

1.1 Biological Inspiration

The human tongue is one of nature's most impressing masterpieces, which we use in various ways to interact with our environment. The capabilities of the tongue reach from sensing and feeling to communicating and even transporting emotions through caresses. Though, one of the most important capabilities of the human and mammalian tongues are their use as manipulators and speech generators.

Tongues and other mammalian organs, for example the elephant's trunk, are composed almost entirely out of muscles, which achieve both movement and support with these structures [1, 2]. Those organs are called muscular hydrostats and arrange muscles in a way, that every dimension can be actively controlled, which allows bending, extension, compression and torsion in a highly complex and controlled way [2, 3, 4, 5]. Therfore, these muscular hydrostats may be the biological pendant to what robotic scientist call continuous robots. While the appearance of rigid serial link robots is strongly influenced by the human arm, there are almost no limitations of design the shape of continuous robots [5]. This might be the main reason, why the applications and opportunities for continuous robots or continuous parts of robots seem to be endless. Once again, the nature gave a strong inspiration.

1.2 Applications and Opportunities

Continuous Gripping

Figure 1.1: Gripping: opposums hanging from a tree branch by using cabel friction

The concept of conventional robot grippers is based on a finite number of contact points located all over the object. Instead by assuming a continuous robot, this approach shifts to the concept of continuous gripping [6]. The continuous gripper conforms to the shape of the object and builds up a line consisting of an infinite number of gripping points, instead of distinguishing discrete points of force supply [6, 7, 8]. The three opossums in Fig.1.1 wrapping their tails around a tree

branch and using cable friction to balance their own weight. By the use of this principle a wide range of objects and shapes can be manipulated [6, 7, 5, 2]. McMahan *et al.* achieved their continuous manipulater, *OctArm*, to stack and unstack traffic cones within a grasping experiment [7]. As well, concepts for high dynamic grasping, based on the principle of a bull whip have been proposed [5, 6].

Exploration and Sensing

Figure 1.2: Exploration and sensing: giraffe entering and exploring it's nose with it's tongue

Continuous robots enable dexterous movement for the operator in environments, which are unreachable for humans or rigid robots [7, 9, 5, **?**]. In a snake-like manner, they are able to explore e.g. collapsed buildings as a search and rescue robot or enter the human body within a minimally invasive robotic surgery (MIRS) through small orifices [7, 10, 11]. Within these restricted areas, continuous robots are able to feel the shape of object by wrapping around them. As they do this in a minimal energy fashion, they posses an intrinsic force sensing capability and, therefore, can eliminate the need of cost-intensive and complex force torque sensors [11, 12]. Especially for the MIRS these force sensing capabilities have the potential to improve the tactile sensing of the surgeon [13].

Balance

Figure 1.3: Balancing: kangaroo using it's tail to hold balance while fast locomotion.

In nature, many animals use their tails to hold balance while they undergo fast or accurate locomotion [5]. E.g. monkeys and cats use their tails while balancing on tree branches or other

thin paths, while the Kangaroo uses it's tail to compensate the large sweeping motions of it's legs [14, 15]. The company FESTO has built a robotic kangaroo which uses a rigid tail to stabilise itself within the flying period [16].

Transportation

Figure 1.4: Transportation: elephant blows sand out of his trunk to give himself a shower.

Bulk transportation plays a huge role in production and waste disposal [17]. The absence of joints or actuators within a under-actuated continuous structure provides the possibility to integrate a working channel [6]. Various researchers have designed suction or transportation units to use for waste disposal or bulk transportation [18, 19]. In laparoscopic surgery, consumables such as needles or clips are introduced manually through another incision into the body and tissue is removed by the use of a specimen pouch [20]. The presence of a working channel could make this procedure more efficient and reduce trauma of tissue.

Movement in Difficult Terrain

Figure 1.5: Movement in difficult terrain: snake making its way through a tree.

Nature offers a wide range of movements of which animals can make use in difficult terrain. The snake e.g. is capable of moving in four different ways depending on the terrain, namely serpentine, sinus-lifting, pedal wave and side-winding [5]. In dessert areas e.g. the snake uses the economic side-winding technique to propel itself through the sand [9]. With these innovative movement forms one can imagine as well a amphibious robot, capable of passing small winding

path, harsh terrain, water or even trees as shown in fig:.1.5 [9, 5, 2]. One example in the field of medicine is the Colobot, by CHEN *et al.* which can semi-autonomous steer through the human colon within a colonoscopy [21, 22].

1.3 Classification of Serial Link Robots

In the past, various researchers have classified the serial link robotics in different ways. Most of them used the number of joints, the actuation and the material as a criteria of classification [2, 23, 24]. The following section gives a simplified classification including the number of joints and the actuation based on the work of TRIVEDI *et al.*[2]. It has to be mentioned, that this approach does not aim to classify the research field of robotics in general - we tried to give an overview and aimed to clarify the difference between discrete hyper-redundant and continuous robots.

1.3.1 Rigid Robots

The design of rigid robots is strongly inspired by the shape of the human arm and consist usually of a few number of joints serially connected with rigid links [5]. Such robots reach a high precision and and allow for fast motion in prescribed tasks, primary used in manufacturing [2]. Usually, every joint gives rise to one degree of freedom and is actuated independently [2]. While rigid robots are easy to control and are capable of carrying high loads, their rigidity lead to a serious risk of harming people [25, 26, 27].

1.3.2 Discrete Hyper-redundant Robots

The Field of discrete hyper-redundant robots intersects somehow with the field of continuous robots and is not clearly defined. Most researchers classify them as robots, consisting of a finite, but large number of independently actuated joints [2, 9]. Here, this classification will be limited to one more constraint: We will classify every robot consisting of a large number of under-actuated joints connected by rigid links as to be discrete hyper-redundant. As examples one can mention the mechanisms, see [28, 29], which are hyper-redundant and under-actuated, but not continuous. Pioneers in the field of discrete hyper-redundant robots have been ANDERSON and HORN, who developed the Tensor-Arm in the late 1960s for the use within undersea applications [30, 24, 31].

1.3.3 Continuous Robots

We will classify continuous robots as under-actuated robots, divided into a finite number of sections of which every section consists of a flexible mechanism that provides both structure and motion by bending, elongation, compression or torsion. Therefore, a continuous robot consists of a infinite number of joints which makes it theoretically possible to reach every point in the workspace with a infinite range of robot shapes [2]. Some of the main disadvantages

	Rigid	Discrete hyper-redundant	Continuous
Design			
Number of joints	Few	Large	Infinite
Actuation	Completely actuated	Completely actuated / under-actuated	Under-actuated
Inspiration	Human arm	Snakes, fish	Muscular hydrostats
Capabilities			
Accuracy	Very high	High	Low
Load Capacity	High	Low	Lower
Safety	Dangerous	Dangerous	Safe
Dexterity	Low	High	Very high
Working environment	Only structured	Unstructured	Unstructured
Versatility	Dedicated tasks only	Extended	Various applications
Manipulating Objects	Fixed size and class	Fixed object class	Variable

Table 1.1: Classification and capability of Robots, see [2]. Rigid Robots show their high potential in dedicated manufacturing tasks, where high precision is required. Continuous robots provide high dexterity, versatility and a space-saving mechanical design.

of continuous robots are the a relatively low load capacity and greater difficulties in control compared to rigid robots [2]. Opposed to that, continuous robots create a lot of new opportunities as mention in (1.2, p.1) and are said to allow a save interaction with humans [2, 5]. One more advantage becomes clear, if one considers to replace a conventional robot joint by a continuous structure. Bending, elongation and torsion could be realised with only one joint unit occupying a minimum space. This may be very useful in applications where there are minimum space is required such as in MIRS [12].

2 State of the Art in Continuous Robots in Research and Medicine

2.1 Overview

Many research groups have been focusing on the promising field of continuous robots. Tab.2.1 (p.9) gives an overview of research works in this field, based on the work of WEBSTER *et al.* [24]. Note that this tabular just contains continuous robots in the sense as classified in (1.3, p.4). Discrete hyper-redundant robots have been neglected. In general, continuous robots consist of a continuum for support and actuators, placed in a certain geometric pattern around it [23]. This continuum can consist of pneumatic bladders, soft cylinders, elastic rods, meshes or elastomers. As actuators, a wide range of technologies are used. Conventional tendons provide an easy mechanical design [11, 32]. As well, pneumatic artificial muscles, shape memory alloy (SMA) or combinations are used for actuating continuous robots [2, 33, 34]. Another way of actuating a continuous robot might be the use of electro active polymers (EAP) [2]. In this young research field, a dielectric polymer is forced to produce stress and strain by the use of electric voltage [2]. An intresting finding is, that the behaviour and the properties of EAP are close to mammalian muscles regarding strain, actuation pressure, density, efficiency and speed [2]. The actuators are usually placed in a angel of 120° around the continuum and work together to provide bending and elongation [23, 35, 2]. While writing this work, the Harvard Biodesign Lab developed a fluidic actuator which even allows for torsion [36]. The continuous structures are usually divided into a finite number of sections to allow for conforming to a complex shape [24]. Therefore, every section has to be actuated by its own set of actuators.

In the late 1960s the field of discrete hyper-redundant robots experienced a setback because the kinematic models describing the robot's behaviour were poorly understood [24]. In addition to that, researchers have been very limited because of the lack of computation power. Within the 90s the research revived and much effort went into new modelling approaches including the work of CHIRIKJIAN *et al.*, which might has been the first research group in time proposing a modal approach [**?**]. Based on this, many researcher focused on generating new sophisticated models, for example GRAVNGE *et al.*, DUPONT *et al.* and WEBSTER *et al.*, who proposed the use of beam theories [24, 11, **?**, 37]. However, they focused on the Euler-Bernoulli case for thin beams, which might be an oversimplification for some applications. The group of WEBSTER has been the first in time proposing the fast constant curvature approximation on which many researches have based their modelling approaches and implemented controllable continuous structures [38, 39, **?**, 40, 41, 42, 43]. Although the beam theory has been taken into consideration and proven to be a suitable modelling approach, there was no research group found, which focused on the investigation of shear within a kinematic model for continuous robots by now.

Literature	First citation	Sections	DOF/sec.	bending angle	Continuum	Actuation	Application	Image
Micro-active catheter [34]	1994	3	2	80°, overall	Soft cylinder	SMA	minimally invasive surgery	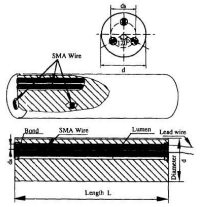
KSI-Tentacle [44]	1995	2	3	90°, each	Pneumatic bladder	Tendon, pneumatic	Nuclear decontamination, material handling	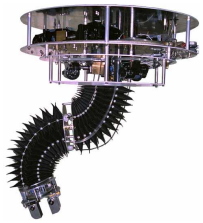
Elephant trunk [17]	1999	3	2	120°, 90°, 30°	Springs	Tendon	Liquid transportation	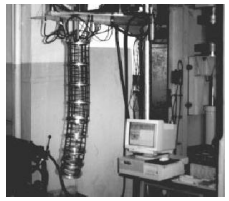
Backbone [11]	2003	2	1	90°, each	Elastic rod	Tendon	Research	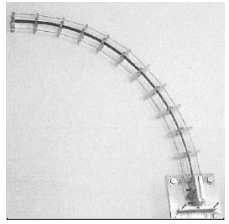
Colobot [22, 21]	2004	1	2	120°	Silicone-rubber tube	Pneumatic	Colonoscopy	

continued on next page

Literature	First citation	Sections	DOF/sec.	bending angle	Continuum	Actuation	Application	Image
DDU [45, 46]	2004	2	2	90°, 60°	NiTi-Tubes	Via backbone	Laryngeal surgery	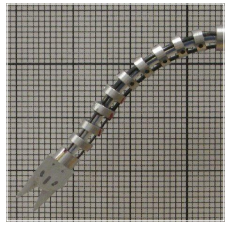
SPORT® [46]	2009, available probably 2015	Based on Simaan's DDU					Single port MIS surgery	
Air-Octor [47]	2005	2	3	N/A	Pressure chamber and springs	Tendon, pneumatic	General purpose	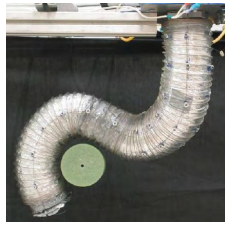
OctArm [?, 48, 40]	2006	3	3	90°, 180°, 360°	Plastic mesh tube	Pneumatic muscle (McKibben actuator)	General purpose	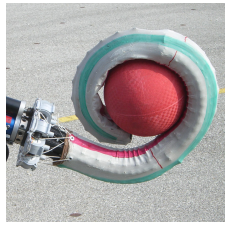
Catheter [32, 49]	2008	2	2	270°, overall	Hollow NiTi-Spine	Tendon	Cardiac surgery	

continued on next page

Literature	First citation	Sections	DOF/sec.	bending angle	Continuum	Actuation	Application	Image
STRAS, actuated Anubis-System (STORZ) [50, 51]	2013	1	2	120°	Continuum shaft (not specified)	Tendon	Endoluminal and transluminal surgery	
Hansen Medical Sensei® [4]	2010	Based on Camarillo's Catheter					Surgery	
FESTO BHA [38]	2012	3	4	N/A	Polyamid tube	Pneumatic bellows	Research and development	
Harvard Soft Robot [?]	2015	1	4	Almost 360°	elastomer	Fluidic actuator	Research rehabilitation	

Table 2.1: Continuous robots in research, industry and medicine

2.2 Application in Medicine

The application of continuous or discrete hyper-redundant robots in medicine include a wide range of surgical procedures, in which they can be, or already are extremely useful [45, 46, 10, 2]. Especially when it comes to MIRS or natural orifice translumeal endoscopic surgery (NOTES), the advantages are outstanding. In these techniques, the operating situs is entered through small incisions or natural orifices, which reduces the degrees of freedom (DOF), that the surgeon can use while operating [13]. In such cases the dexterity of a continuous robot would enable the surgeon to accomplish complex working tasks in the operating situs [46, 13, 12]. A further major advantage is the absence of complex joints within the continuum. This gives rise to many possibility, which are very difficult to achieve with rigid or hyper-redundant robots. Namely the reduced building space or an easy to sterilise mechanical design, to mention a few. However, one of the most important advantage is the possibility of integrating a working channel to provide the surgeon with consumables, suction or materials. By now, this task is executed by an assistant surgeon through an additional incision, which increases tissue trauma [20].
There are two fields, on which continuous robots have been extremely successful by now, namely catheterization procedures and the young field of robotic laryngeal surgery [46, 52]. As well, there have been approaches on using discrete hyper-redundant robots for cardiac surgery and other laparoscopic procedures [53, 54, 55]. Because in this field, there have been almost no continuous structures established by now, we will just give a brief summary.

2.2.1 Catheterization Using Continuous Robots

Catheterization describes a surgical technique, where a thin and very long tube is steered through a lumen and made visible through ionizing radiation or fluoroscopy [56]. Especially for stent-grafting, this is a very useful procedure to threat e.g. aortic aneurysm [57, 10]. This technique is very complicated and time consumptive and requires a highly trained surgeon to achieve good results within the procedure [58, 52, 57]. Therefore, those interventions are cost intensive and expose the patient to harmful radiation. Because of that, many research groups focused on micro-active steerable catheter systems with the endeavour to make catheterization more feasible and save for the clinical use. To the authors knowledge, in 1994, FUKUDA *et al.* have been the first group that developed a micro-active catheter system [34]. This system was capable of two bending DOF and actuated via SMA [34]. Many researcher followed this example and developed very similar systems, which were actuated eighter by SMA or tendons [32, 49, 33, 59, 56]. By now, robotic steerable catheters have been used in various clinical interventions. RIGA *et al.* showed, that the use of the robotic catheter system Sensei® (HANSEN MEDICAL) reduced overall procedure time and improved accuracy, regardless of the training level of the surgeon in a pulsatile silicone phantom model [52]. Afterwards they have successfully stend-crafted a 78-years old man suffering from aortic aneurysm with the use of this continuous robot system

[57]. One year later, LUMSDEN *et al.* reported the successful treatment of a pulmonary artery stenosis, where conventional interventions failed [60].

2.2.2 Laryngenal Surgery

The Larynx, also known as the voice box, is an organ of immense complexity. At least a dozen muscles work together to provide breathing functions, voice generation, and airways protection during swallowing [61, 45]. Abnormalities of the vocal fold or laryngeal cancer often go hand in hand with the need of a surgical procedure [45, 46]. If performed as a conventional open surgery, those procedures inevitably lead to the damage of healthy tissue which might result in scar production, loss of speech or dysphagia [46, 45, 61, 62]. SIMAAN *et al.* focused on the development of a continuous backbone robot to enhance dexterity of the surgeon. Their goal is to use the throat as a pre-determined access port and, therefore, reduce trauma of the healthy tissue framework [45]. The prototype consist of a dual-slave robotic system operated telepresently through a DaVinci® surgeon console (INTUITIVE SURGICAL) [46, 63]. Last reported achievements were the sucessfully complementaion of intracorporal sutering tasks in a animal model [46]. There is clear evidence, that this technique has been translated to the SPORT® system (TITAN MEDICAL), which might be available in 2015.

2.2.3 Hyper-redundant Robotics in Cardiac Surgery and other Laparoscopic Procedures

Many research groups have focused on the design and application of hyper-redundant structures for MIRS or NOTES. The company MEDROBOTICS e.g. developed the CardioArm® , a snakelike robot consisting of discrete elements for the purpose of single port operations on the beating heart [54]. A clinical trial showed good results for minimally invasive epicardial mapping, which gives evidence, that this technology might be a promising approach [54]. Similar to that, AMIR *et al.* introduced HARP, an under actuated snake-like device for cardiac surgery. With this device, they achieved to reach the epicardium through a lumen within an animal model [53]. In addition to that, many new fields of application have been investigated, e.g. athroscopy or fetal surgery [55, 46]. As mentioned above, discrete hyper-redundant robots consist of a rigid and very complex structure. Therefore, they are potentially unsafe and difficult to sterilize, which might be problematic within cardiac or laparoskopic MIRS [2, **?**]. To overcome these difficulties, DEDONNO *et al.* focused on a master-slave device for telepresent MIRS, based on the continuous structure Anubis® (KARL ZEISS) [51, 64]. Although this approach is promising, because of the soft structure and the easily sterilised design, there were no later citations reported.

3 Motivation and Structure

The purpose of this work was to investigate the bending characteristics of a compliant mechanism, which allows for an angular deflections of $\pm 35^\circ$ without any plastic deformation or buckling. Therefore, an elastomer was chosen as the structure's material, whereas the geometry was designed to meet the requirements of a planar motion only and eliminate buckling.
The material properties of silicones said to be highly non-linear with respect to stress, strain, and also, they depend on the manufacturing process. Furthermore silicone show some degree of non-linearities due to the load's amplitude and velocity. For a model-based controller however, the material properties need to be known.
Therefore, we decided on building up a testbed for one special geometry, which has to fulfil following requirements:

1. the bending stiffness of one direction has to be a lot higher than the other, so one can assume a 2D-bending mechanism.

2. the geometry's slenderness ratio has to be in a range, that one can measure a significant difference between the Euler-Bernoulli and the Timoshenko theory.

3. under a reasonable load, the geometry has to allow a deflection angle of $\pm 30^\circ$.

4. the geometry has to be suitable for position tracking.

The material properties of this geometry were determined with simulation results and verified in tensile and 3-point-bending tests. With this Data the position controller was designed and tested in the same experimental setup.

4 Modelling of Flexible Beams

We assumed that planar motion of the compliant mechanism can be modelled as the transverse motion of an elastic beam. This transverse motion is induced by a general load applied a the beams structure. A general load includes concentrated normal forces, concentrated shear forces as well as concentrated moments along the centre fibre of the beam. Furthermore, a general load incorporates also transverse forces or moments along the surface of the beam. Approaches to model the motion of a beam under this general loading condition are termed geometrically exact beam theory or Cosserat beam theory, see [65].
In contrast, classical beam theories entitled Euler-Bernoulli beam theory or Timoshenko beam theory refer to a series of assumptions including a small deformation and only special load cases. These load cases include no normal forces but shear forces and moments which are defined in the global reference frame. The Euler-Bernoulli beam theory was the first theory in time to be postulated. In this theory, the effect of bending moment only is taken into account. While these assumptions work fine for thin beams under statical loadings, for thicker beams and higher frequencies they are an oversimplification [66]. To overcome these restrictions, the more complex Timoshenko Beam theory was formulated in 1921 and extends the Euler-Bernoulli theory by taking shear deformation and the rotary inertia into account [67]. To give an overview, Tab.4.1 (p.14) compares the Euler-Bernoulli Theory and the Timoshenko theory.
For the special case of a concentrated moment at the tip of the compliant mechanism, both modelling approaches converge. This case is called constant curvature (CC) and many mechanisms in literature are build up and modelled with this assumption [38, 39, **?**, 40, 41, 42, 43].
As stated in the requirements, see (3, p.12), the compliant mechanism in focus should be build up with no additional tip masses and should bend about $\pm 30^\circ$ at its tip. Therefore, the aforementioned classical beam theories seemed an appropriate approach to model statics and dynamics of the compliant mechanism, described in (5, p.43). Within the testbed, the compliant mechanism is actuated by a tip moment only. Thus, the CC approach is used to describe the kinematics, derive in (4.7, p.32).

4.1 Fundamentals of Ordinary Bending

We assume an infinitesimal beam element in the planar case for deriving the fundamental equations of ordinary bending. To obtain explicit formulations of the internal Forces, the following assumptions are made:

1. A right hand coordinate system is used, where the y- and z-directions are main the axes of the cross section and the positive z-direction points downwards [68].

2. The principle of small-angle approximation for a infinitesimal beam element is valid [68].

Assumption	Euler-Bernouli	Timoshenko
Lateral displacement	✓	✓
Bending moment	✓	✓
Shear deformation	×	✓
Rotary inertia	×	✓
Linear elastic material	✓	✓
High frequencies	×	✓

Table 4.1: Comparision of the Euler-Bernoulli and Timoshenko's beam theory: The Euler-Bernouilli theory neglect the shear deformation and the rotary inertia. Both theories do not incorporate large displacements and non-linear material behaviour.

3. The deflection v is independent of the z-coordinate such that:

$$v = v(x), \qquad \theta = \theta(x), \qquad \varepsilon_z = \frac{\partial v(x)}{\partial z} = 0. \tag{4.1}$$

This states, that each point $\boldsymbol{p}$ on the beam's cross section will experience the same deflection $v(x)$ in z-direction and therefore, there will be no changes in the beam's height [68].

4. There will be no changes in the surface of a cross section due to bending. Therefore, each cross section will experience a displacement $v(x)$ and a small angle rotation $\theta(x)$, such that the axial displacement of a point $\boldsymbol{p}$ on a cross section of the beam is given by [69]:

$$u(x,z) = -\theta(x)z. \tag{4.2}$$

Assuming equilibrium of forces in the beam element shown in Fig.4.1 (p.15) yields

$$\frac{\mathrm{d}Q}{\mathrm{d}x} = -q(x), \qquad \frac{\mathrm{d}M}{\mathrm{d}x} = Q, \tag{4.3}$$

where $q(x)$ is a distributed load while the moment M, the transverse force Q and the normal force N are resultants of the axial stress σ_x and transverse shear τ_{xz} [68, 69]:

$$M = \int z\sigma \mathrm{d}A, \qquad Q = \int \tau \mathrm{d}A, \qquad N = \int \sigma \mathrm{d}A. \tag{4.4}$$

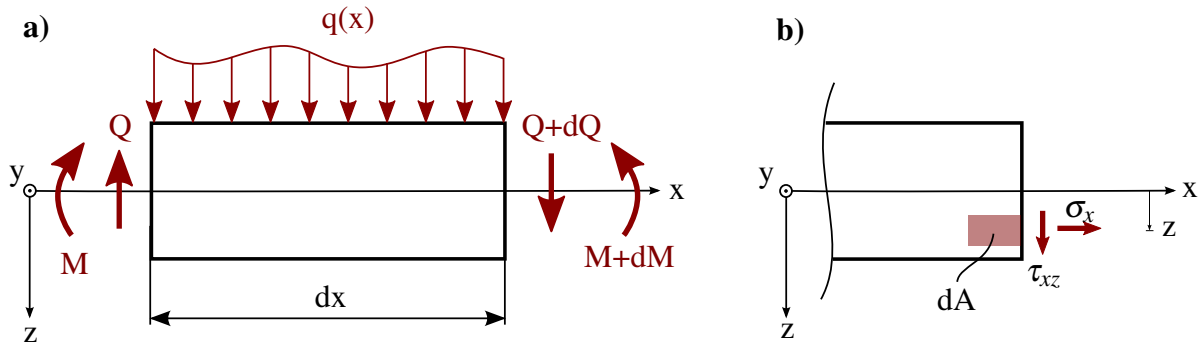

Figure 4.1: a) Schematic drawing of an infinitesimal beam element with external loading $q(x)$. Note that the classical beam theories do not incorporate normal forces. b) An infinitesimal surface element undergoes axial stress σ_x and transverse shear τ_{xz} as resultants of the external forces

The axial stress σ_x is assumed to be considerably larger than σ_z and σ_y and we will refer to $\sigma = \sigma_x$ in the following and treat the shear uniformly, such that $\tau = \tau_{xz}$.
The displacements due to stress and shear of a rectangular planar beam element with side lengths dx and dz is given by [68, 69, 70]

$$\varepsilon = \frac{\partial u}{\partial x}, \qquad \gamma = \frac{\partial v(x)}{\partial x} + \frac{\partial u}{\partial z}, \tag{4.5}$$

where ε is the strain in axial direction and γ is the angular change due to shear (Fig:4.2a, p.16). Combining (4.5), (4.2) and applying Hook's Law yields

$$\sigma = E\frac{\partial u}{\partial x} = -E\frac{\mathrm{d}\theta(x)}{\mathrm{d}x}z, \tag{4.6}$$

$$\tau = G\left(\frac{\partial v(x)}{\partial x} + \frac{\partial u}{\partial z}\right) = G\left(\frac{\mathrm{d}v(x)}{\mathrm{d}x} - \theta(x)\right). \tag{4.7}$$

From those equations we can derive the internal forces by applying (4.4)

$$M = -E\frac{\mathrm{d}\theta(x)}{\mathrm{d}x}\int z^2\mathrm{d}A, \qquad Q = G\left(\frac{\mathrm{d}v(x)}{\mathrm{d}x} - \theta(x)\right)\int \mathrm{d}A, \qquad N = -E\frac{\mathrm{d}\theta(x)}{\mathrm{d}x}\int z\mathrm{d}A, \tag{4.8}$$

where $\int z\mathrm{d}A$ is the first, and $\int z^2\mathrm{d}A$ is the second moment of area [68]. Since the main axes of the cross section are identical with the y- and z-axis of the coordinate system, the first moment of area is zero.
Integrating (4.8) yields

$$M = -EI\frac{\mathrm{d}\theta(x)}{\mathrm{d}x}, \qquad Q = GA\left(\frac{\mathrm{d}v(x)}{\mathrm{d}x} - \theta(x)\right), \qquad N = 0. \tag{4.9}$$

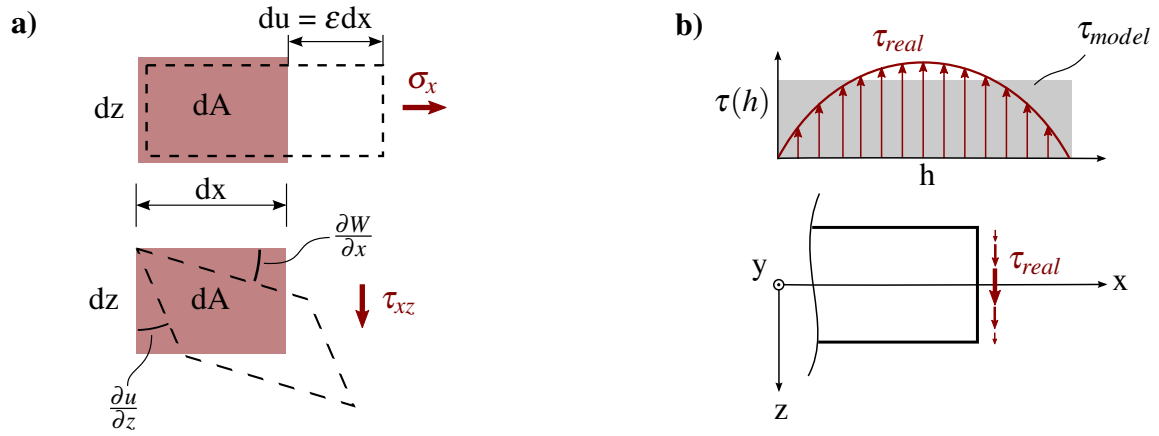

Figure 4.2: a) Displacements in an infinitesimal beam element due to stress and shear. b) Progressions of the real shear τ_{real} and the model shear τ_{model} over the beam's height h. To compensate this error, the shear correction factor κ is introduced

The first equation of (4.9) states, that the angular change of the cross section $\mathrm{d}\theta(x)/\mathrm{d}x$ is proportional to the bending moment M.

The second equation of (4.9) states, that the transverse force Q is constant over the cross section. In fact, Q differs at each point of the cross section (Fig.4.2b, p.16). Especially at the borders of a cross section, there is no shear allowed, $Q = 0$ [68]. To compensate this error, the shear correction factor κ is introduced. κ is defined as the ratio of average shear on the cross section to the product of shear modulus G and the angular change due to shear at the neutral axis γ [71]. Therefore, this factor depends on the considered cross section's geometry [68, 71, 66]. Another finding is, that this factor also depends on the frequency of motion, since the shear stress profile changes to functions of higher orders with higher modes [71, 66, 72]. Introducing the shear correction factor κ changes the second equation of (4.9) to

$$Q = \kappa GA\left(\frac{\mathrm{d}v(x)}{\mathrm{d}x} - \theta(x)\right). \tag{4.10}$$

4.2 Statical Differential Equations of Bending

Equations (4.3), (4.9) and (4.10) are called the differential equations of bending and from those, the transverse displacement v and the angular change of the cross section θ can be computed.

4.2.1 Euler-Bernoulli Theory

The Euler-Bernoulli beam theory does not incorporate shear deformations. Therefore, the shear stiffness is set to $\kappa GA \to \infty$ and (4.10) yields

$$\frac{\mathrm{d}v(x)}{\mathrm{d}x} - \theta(x) = 0. \tag{4.11}$$

This states, that a cross section perpendicular to the neutral axis remains perpendicular to the neutral axis after deformation.
Equations (4.3), (4.9) and (4.11) then can be combined to

$$EI\frac{\mathrm{d}^4 v(x)}{\mathrm{d}x^4} = q(x), \tag{4.12}$$

which is an ordinary differential equation (ODE) and can be solved by integration and applying appropriate geometrical boundary conditions as shown in (4.4, p.20).

4.2.2 Timoshenko Theory

For the Timoshenko case, shear deformation is taken in account which results in two ODE because of the two independent variables $v(x)$ and $\theta(x)$ [67]:

$$\begin{aligned} EI\frac{\mathrm{d}^3\theta(x)}{\mathrm{d}x^3} &= q(x), \\ \frac{\mathrm{d}v(x)}{\mathrm{d}x} &= \theta(x) - \frac{EI}{\kappa GA}\frac{\mathrm{d}^2\theta(x)}{\mathrm{d}x^2}. \end{aligned} \tag{4.13}$$

Again, this set of equations can be solved by integration and applying appropriate geometrical boundary conditions. Figure 4.3 (p.17) shows the effect of shear displacement. While the cross

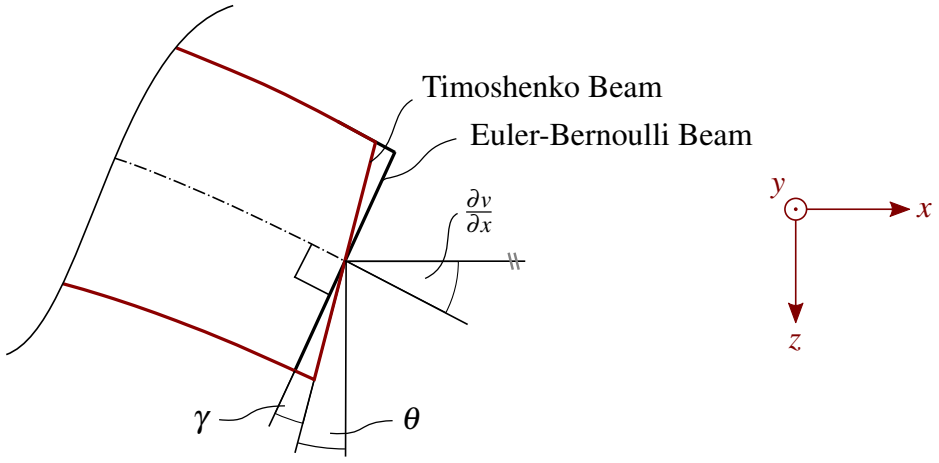

Figure 4.3: Schematic drawing of the cross section's angular change because of shear deformation. While in the Euler-Bernoulli Theory, the planes remain perpendicular to the neutral axis after deformation, in the Timoshenko theory, they experience a small back-shift γ because of the influence of shear.

section of the Euler-Bernoulli beam remains perpendicular after deformation, the Timoshenko

beam undergoes an additional shear deformation γ. With a finite shear stiffness, (4.11) then turns to

$$\frac{\mathrm{d}v(x)}{\mathrm{d}x} - \theta(x) = \gamma \tag{4.14}$$

and, therefore, the shear deformation γ can be expressed with (4.10) as

$$\gamma = \frac{Q(x)}{\kappa GA}. \tag{4.15}$$

Note that γ depends on the transverse force distribution and, for a constant tip force, is a constant over the beam length.

4.3 Equations of Motion for Beam Structures

In the following paragraph, the equations of motion are obtained and solved strongly related to the work of HAN *et.al* [66]. At first, the terms of the kinetic and the potential energy have to be established in order to derive the equations of motion with the use of the Lagrangian formalism. The Lagrangian L is defined as the difference between the total kinetic KE and the total potential energy PE and describes a trajectory along the generalised coordinates r_i, which occur in the same amount as the DOF of the system [73, 70]. The Hamilton's variational principle now states, that the action S of the most probable trajectory between to states $s(t_1)$, $s(t_2)$ has to be minimal [74, 75]. The Lagrangian formalism meets this requirement and is given by

$$\frac{\mathrm{d}}{\mathrm{d}t}\frac{\partial L}{\partial \dot{r}_i} - \frac{\partial L}{\partial r_i} = F_r(x,t). \tag{4.16}$$

The term on the right-hand side is the sum of the non-conservative forces, which are a projection of the acting forces in the space of generalised coordinates [76]. Solving (4.16) results in the equations of motion, where for the Euler-Bernoulli theory $\boldsymbol{r} = v$ and for the Timoshenko theory $\boldsymbol{r} = [v(x,t), \theta(x,t)]^T$. All assumptions made in (4.1, p.13) are valid for this modeling approaches as well.

4.3.1 Euler-Bernoulli Theory

An uniform Beam's potential energy due to bending is given by

$$PE_{bend} = \int_0^L EI \left(\frac{\partial^2 v(x,t)}{\partial x^2}\right)^2 \mathrm{d}x \tag{4.17}$$

and its kinetic energy due to lateral displacement is given by

$$KE_{trans} = \int_0^L \rho A \left(\frac{\partial v(x,t)}{\partial t}\right)^2 \mathrm{d}x, \tag{4.18}$$

where ρ is the materials density. Building up the Lagrangian L results in

$$L = \int_0^L \left[\rho A \left(\frac{\partial v(x,t)}{\partial t} \right)^2 - EI \left(\frac{\partial^2 v(x,t)}{\partial x^2} \right)^2 \right] \mathrm{d}x. \tag{4.19}$$

Since the Euler-Bernoulli theory has one DOF, the Lagrangian formalism results in one equation of motion for the generalised coordinate $r = v(x,t)$:

$$\rho A \frac{\partial^2 v(x,t)}{\partial t^2} + EI \frac{\partial^4 v(x,t)}{\partial x^4} = F_r(x,t). \tag{4.20}$$

Neglecting all the time derivatives leads to the statical differential equation of bending (4.12) postulated in (4.2, p.16).

4.3.2 Timoshenko Theory

The equations of motion for the Timoshenko beam are obtained in the same fashion as for the Euler-Bernoulli theory. As mentioned previously, the Timoshenko theory includes the effect of bending moment, lateral displacment and additional to that, the effect of shear distortion and rotary inertia [67].
The potential energy due to shear is given by

$$PE_{shear} = \frac{1}{2} \int_0^L \kappa GA \left(\frac{\partial v(x,t)}{\partial x} - \theta(x,t) \right)^2 \mathrm{d}x, \tag{4.21}$$

where $\partial v(x,t)/\partial x$ is the slope of the bending curve and $\theta(x,t)$ represents the angel of the surface. In this case, we assume, that only the angular change of the real slope is taken into account for the rotary energy, which results in

$$KE_{rot} = \frac{1}{2} \int_0^L \rho I \left(\frac{\partial \theta(x,t)}{\partial t} \right)^2 \mathrm{d}x. \tag{4.22}$$

According to that (4.17) is modified to:

$$PE_{bend} = \frac{1}{2} \int_0^L EI \left(\frac{\partial \theta(x,t)}{\partial x} \right)^2 \mathrm{d}x. \tag{4.23}$$

Building the Lagrangian yields

$$\begin{aligned} L = \frac{1}{2} \int_0^L \Bigg[& \rho A \left(\frac{\partial v(x,t)}{\partial t} \right)^2 + \rho I \left(\frac{\partial \theta(x,t)}{\partial t} \right)^2 \\ & - EI \left(\frac{\partial \theta(x,t)}{\partial x} \right)^2 - \kappa GA \left(\frac{\partial v(x,t)}{\partial x} - \theta(x,t) \right)^2 \Bigg] \mathrm{d}x. \end{aligned} \tag{4.24}$$

Note that because of the influence of shear, the slope of the bending curve is not the first derivative of the displacement as in the Euler-Bernoulli theory. In this theory, the presence of a transverse force opposes a small back-shift to the plane angle and, therefore, a second generalised coordinate $\theta(x,t)$ is required to describe the system entirely. The Lagrangian equations of motion then yield

$$\begin{aligned} \rho A \frac{\partial^2 v(x,t)}{\partial t^2} - \kappa GA \left(\frac{\partial^2 v(x,t)}{\partial x^2} - \frac{\partial \theta(x,t)}{\partial x} \right) &= F_r(x,t), \\ \rho I \frac{\partial \theta(x,t)}{\partial t^2} - EI \frac{\partial^2 \theta(x,t)}{\partial x^2} - \kappa GA \left(\frac{\partial v(x,t)}{\partial x} - \theta(x,t) \right) &= 0. \end{aligned} \tag{4.25}$$

Again, neglecting the time dependent terms of (4.25) lead to the statical differential equations of bending for the Timoshenko case as shown in (4.13)

4.4 Boundary Conditions and Spatial Solution

The equations of motions derived in (4.3, p.18) for both theories are solved using the method of *eigenfunction expansion* [75]. The process in principle is the same for the Euler-Bernoulli and the Timoshenko theory:

1. Separating the homogeneous equations of motion ($F_r(x,t) = 0$) into to two ODE such that, $v(x,t) = \boldsymbol{w}(x)T(t)$, where $T(t)$ are the time solutions and $\boldsymbol{w}(x)$ the solutions in modal space with $\boldsymbol{w}(x) = W(x)$ for the Euler-Bernoulli theory and $\boldsymbol{w}(x) = [W(x), \Psi(x)]^T$ for the Timoshenko theory. $w(x)$ are called eigenfunctions.

2. Solving the spatial ODE for $\boldsymbol{w}(x)$. One will derive functions of sinusoidal and hyperbolic terms for both theories.

3. Determining the frequency equation using geometrical boundary conditions. The roots of this frequency equation will be related to the eigenfrequencies of the flexible structure. With those, one can identify the coefficients of the spacial solutions. Those spacial solutions are the mode shapes or eigenvectors of the eigenvalue problem.

4. Solving the inhomogeneous equations of motion using the method of *eigenfunction expansion*. Therefore, the eigenfrequencies and mode shapes need to be known.

Four different cases of geometrical boundary conditions are shown in fig:.4.4 (p.21) with the following practical relevance: While the clamped end is used for the base of a continuous robot, the free end represents its tip. The hinged end can be taken into account, when a junction of two continuous segments has to be described. Since in this case the continuous structure has only

one segment, the boundary conditions of the hinged and clamped end are taken into account. At the clamped end, the displacement $v(x) = 0$ and the slope $\theta(x) = 0$. The free end does not allow any internal forces or moments such that $Q(x) = 0$ and $M(x) = 0$. Note that these boundary conditions are independent from the used beam theory, but the equations to describe $v(x)$, $\theta(x)$, $Q(x)$ and $M(x)$ differ depending on the theory.

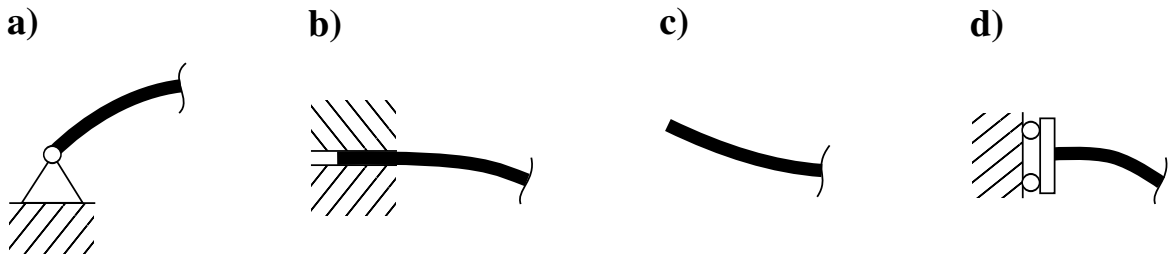

Figure 4.4: Four types of the geometrical boundary conditions. a) Hinged end, $M = 0$, $v = 0$. b) Clamped end, $v = 0$, $\theta = 0$. c) Free end, $M = 0$, $Q = 0$. d) Sliding end, $\theta = 0$, $Q = 0$.

4.4.1 Spatial Solution for the Euler-Bernoulli theory

Following the instructions from (4.4, p.20), one derives two decoupled ODE using the method of *separation of variables*:

$$\ddot{T}(t) + \omega^2 T(t) = 0, \tag{4.26}$$

$$W^{IV}(x) - \frac{\rho A}{EI}\omega^2 W(x) = 0. \tag{4.27}$$

With the introduction of the dispersion relationship

$$a^4 = \frac{\rho A}{EI}\omega^2, \tag{4.28}$$

the solutions for (4.26) and (4.27) are found to be

$$T(t) = d_1 \sin(\omega t) + d_2 \cos(\omega t), \tag{4.29}$$

$$W(x) = C_1 \sin(ax) + C_2 \cos(ax) + C_3 \sinh(ax) + C_4 \cosh(ax). \tag{4.30}$$

The geometrical boundary conditions result in

$$\begin{aligned} \frac{\mathrm{d}W(0)}{\mathrm{d}x} &= 0, & W(0) &= 0, \\ EI\frac{\mathrm{d}W(L)}{\mathrm{d}x^2} &= 0, & EI\frac{\mathrm{d}W(L)}{\mathrm{d}x^3} &= 0. \end{aligned} \tag{4.31}$$

Applying those boundary conditions to (4.30) and rearranging them yields

$$\boldsymbol{F}\boldsymbol{c} = \mathbf{0}, \tag{4.32}$$

with $\boldsymbol{F} \in \mathbb{R}^{4x4}$ and $\boldsymbol{c} \in \mathbb{R}^4$. To avoid the trivial solution $\boldsymbol{c} = 0$ the determinant of $\boldsymbol{F}$ has to be zero:

$$\det(\boldsymbol{F}) = \cos(a_n \cdot L)\cosh(a_n \cdot L) + 1 = 0. \tag{4.33}$$

This determinant is called the frequency equation of the structure and has an infinite number of roots, $n = 1...\infty$. Those roots are the wave numbers for the chosen set of boundary conditions and can be written as well as dimensionless wave numbers by the use of $a_n^* = a_n \cdot L$. Now, $\boldsymbol{c}_n$ can be reduced from four unknowns to one choosing one coefficient to be a constant. Therefore, one obtains the eigenfunction or mode shape for every eingenfrequency. Those mode shapes are orthogonal but not orthonormal to each other. To determine the last unknown coefficient the mode shapes need to be normalized with respect to each other as shown in (4.5, p.25).

4.4.2 Spatial Solution for the Timoshenko Theory

Since the Timoshenko theory consists of two independent variables $v(x,t)$ and $\theta(x,t)$, (4.25) needs to be decoupled into

$$\begin{aligned} EI\frac{\partial^4 v}{\partial x^4} - \left(\rho I + \frac{\rho EI}{\kappa G}\right)\frac{\partial v}{\partial x^2 \partial t^2} + \rho A\frac{\partial^2 v}{\partial t^2} + \frac{\rho^2 I}{\kappa G}\frac{\partial^4 v}{\partial t^4} &= 0, \\ EI\frac{\partial^4 \theta}{\partial x^4} - \left(\rho I + \frac{\rho EI}{\kappa G}\right)\frac{\partial \theta}{\partial x^2 \partial t^2} + \rho A\frac{\partial^2 \theta}{\partial t^2} + \frac{\rho^2 I}{\kappa G}\frac{\partial^4 \theta}{\partial t^4} &= 0, \end{aligned} \tag{4.34}$$

to proof, that the differential equations obeyed by $v(x,t)$ and $\theta(x,t)$ are of the same form. Therefore, one can postulate the relationship

$$\begin{bmatrix} v(x,t) \\ \theta(x,t) \end{bmatrix} = \begin{bmatrix} W(x) \\ \Psi(x) \end{bmatrix} T(t) \tag{4.35}$$

and use the method of *separation of variables* to decouple (4.25) into

$$\ddot{T}(t) + \omega^2 T(t) = 0, \tag{4.36}$$

$$\begin{aligned} \vec{0} = \quad & \begin{bmatrix} \kappa GA & 0 \\ 0 & EI \end{bmatrix}\begin{bmatrix} W''(x) \\ \Psi''(x) \end{bmatrix} + \begin{bmatrix} 0 & -\kappa GA \\ \kappa GA & 0 \end{bmatrix}\begin{bmatrix} W'(x) \\ \Psi'(x) \end{bmatrix} + \\ & + \begin{bmatrix} \rho A\omega^2 & 0 \\ 0 & \rho I\omega^2 - \kappa GA \end{bmatrix}\begin{bmatrix} W(x) \\ \Psi(x) \end{bmatrix}. \end{aligned} \tag{4.37}$$

Again (4.37) can be decoupled into two similar differential equations, to proof that $W(x)$ and $\Psi(x)$ are of the same form:

$$\begin{aligned}\Psi^{IV}(x)+\left(\frac{\rho I}{EI}\omega^2+\frac{\rho}{\kappa G}\omega^2\right)\Psi''(x)+\left(\frac{\rho^2 I}{\kappa GEI}\omega^4-\frac{\rho A}{EI}\omega^2\right)\Psi(x)=0,\\ W^{IV}(x)+\left(\frac{\rho I}{EI}\omega^2+\frac{\rho}{\kappa G}\omega^2\right)W''(x)+\left(\frac{\rho^2 I}{\kappa GEI}\omega^4-\frac{\rho A}{EI}\omega^2\right)W(x)=0.\end{aligned} \tag{4.38}$$

We consider the approach

$$\begin{bmatrix}W(x)\\ \Psi(x)\end{bmatrix}=\sum_{i=1}^{n} d_i \boldsymbol{u}_i \mathrm{e}^{\lambda_i x} \tag{4.39}$$

for the solution of the eigenvalue problem (4.37), where d_i is a constant coefficient, $\boldsymbol{u}_i$ is the eigenvector and λ_i is the eigenvalue. Substituting (4.39) into (4.37) yields

$$\begin{bmatrix}\kappa GA\lambda^2+\rho A\omega^2 & -\kappa GA\lambda\\ \kappa GA\lambda & EI\lambda^2+(\rho I\omega^2-\kappa GA)\end{bmatrix}\boldsymbol{u}=\vec{0} \tag{4.40}$$

with four eigenvalues and eigenvectors:

$$\lambda_i=\pm\sqrt{-\left(\frac{1}{E}+\frac{1}{\kappa G}\right)\frac{\rho}{2}\omega^2\pm\sqrt{\left(\frac{1}{E}-\frac{1}{\kappa G}\right)^2\frac{\rho^2}{4}\omega^4+\frac{\rho A}{EI}\omega^2}}, \tag{4.41}$$

$$\boldsymbol{u}_i=\begin{bmatrix}\kappa GA\lambda_i\\ \kappa GA\lambda_i^2+\rho A\omega^2\end{bmatrix}. \tag{4.42}$$

Now the spatial solution is given by

$$\begin{bmatrix}W(x)\\ \Psi(x)\end{bmatrix}=d_1\vec{u}_1\mathrm{e}^{bx}+d_2\vec{u}_2\mathrm{e}^{-bx}+d_3\vec{u}_3\mathrm{e}^{\mathrm{i}ax}+d_4\vec{u}_4\mathrm{e}^{\mathrm{i}ax}, \tag{4.43}$$

with

$$\begin{aligned}a&=\sqrt{\left(\frac{1}{E}+\frac{1}{\kappa G}\right)\frac{\rho}{2}\omega^2+\sqrt{\left(\frac{1}{E}-\frac{1}{\kappa G}\right)^2\frac{\rho^2}{4}\omega^4+\frac{\rho A}{EI}\omega^2}},\\ b&=\sqrt{-\left(\frac{1}{E}+\frac{1}{\kappa G}\right)\frac{\rho}{2}\omega^2+\sqrt{\left(\frac{1}{E}-\frac{1}{\kappa G}\right)^2\frac{\rho^2}{4}\omega^4+\frac{\rho A}{EI}\omega^2}}.\end{aligned} \tag{4.44}$$

Note that a is always real while b is either real or imaginary depending on the frequency ω. The frequency, where the transition occurs is called the cut-off frequency and is given by

$$\omega_c = \sqrt{\kappa GA/\rho I}. \tag{4.45}$$

Now with the trigonometrical relationships and $\omega < \omega_c$, (4.43) can be rewritten to a function of sinusoidal and hyperbolic terms analogue to (4.30):

$$\begin{bmatrix} W(x) \\ \Psi(x) \end{bmatrix} = \begin{bmatrix} C_1 \\ D_1 \end{bmatrix} \sin(ax) + \begin{bmatrix} C_2 \\ D_2 \end{bmatrix} \cos(ax) + \begin{bmatrix} C_3 \\ D_3 \end{bmatrix} \sinh(bx) + \begin{bmatrix} C_4 \\ D_4 \end{bmatrix} \cosh(bx). \tag{4.46}$$

The relationship between C_i and D_i is given in terms of the eigenvectors $\boldsymbol{u}_i$:

$$\begin{aligned} \begin{bmatrix} C_1 \\ D_1 \end{bmatrix} &= \mathrm{i}(d_3\boldsymbol{u}_3 - d_4\boldsymbol{u}_4), & \begin{bmatrix} C_2 \\ D_2 \end{bmatrix} &= d_3\boldsymbol{u}_3 + d_4\boldsymbol{u}_4, \\ \begin{bmatrix} C_3 \\ D_3 \end{bmatrix} &= d_1\boldsymbol{u}_1 - d_2\boldsymbol{u}_2, & \begin{bmatrix} C_2 \\ D_2 \end{bmatrix} &= d_1\boldsymbol{u}_1 + d_1\boldsymbol{u}_2. \end{aligned} \tag{4.47}$$

Since d_3 and d_4 are complex conjugates of each other, one can build up the following relationship based on (4.47):

$$\begin{aligned} D_1 &= -\frac{\kappa GAa^2 - \rho A\omega^2}{\kappa GAa} C_2, & D_2 &= \frac{\kappa GAa^2 - \rho A\omega^2}{\kappa GAa} C_1, \\ D_3 &= -\frac{\kappa GAb^2 + \rho A\omega^2}{\kappa GAb} C_4, & D_4 &= \frac{\kappa GAb^2 + \rho A\omega^2}{\kappa GAb} C_3. \end{aligned} \tag{4.48}$$

For $\omega > \omega_c$ the spatial solution consists only of sinusoidal terms and yields

$$\begin{bmatrix} W(x) \\ \Psi(x) \end{bmatrix} = \begin{bmatrix} \widetilde{C}_1 \\ \widetilde{D}_2 \end{bmatrix} \sin(ax) + \begin{bmatrix} \widetilde{C}_2 \\ \widetilde{D}_2 \end{bmatrix} \cos(ax) + \begin{bmatrix} \widetilde{C}_3 \\ \widetilde{D}_3 \end{bmatrix} \sin(\widetilde{b}x) + \begin{bmatrix} \widetilde{C}_4 \\ \widetilde{D}_4 \end{bmatrix} \cos(\widetilde{b}x), \tag{4.49}$$

where $\widetilde{b} = \mathrm{i}b$ and the relationsship between $\widetilde{C}_i$ and $\widetilde{D}_i$ is, analoque to (4.48)

$$\begin{aligned} \widetilde{D}_1 &= -\frac{\kappa GAa^2 - \rho A\omega^2}{\kappa GAa} \widetilde{C}_2, & \widetilde{D}_2 &= \frac{\kappa GAa^2 - \rho A\omega^2}{\kappa GAa} \widetilde{C}_1, \\ \widetilde{D}_3 &= -\frac{\kappa GA\widetilde{b}^2 - \rho A\omega^2}{\kappa GA\widetilde{b}} \widetilde{C}_4, & \widetilde{D}_4 &= \frac{\kappa GA\widetilde{b}^2 - \rho A\omega^2}{\kappa GA\widetilde{b}} \widetilde{C}_3. \end{aligned} \tag{4.50}$$

Now, with (4.48) and (4.50) the amount of unknown coefficients is reduced from eight to four and, therefore, we are able to solve the eigenvalue Problem as shown in (4.4.1, p.21).
Since the boundary conditions are the same for both cases, but the equations to describe them differ from each other, (4.31) needs to be transformed to match the Timoshenko theory:

$$\begin{aligned} \Psi(0) &= 0, & W(0) &= 0, \\ \frac{\mathrm{d}\Psi(L)}{\mathrm{d}x} &= 0, & \kappa GA\left(\frac{\mathrm{d}W(L)}{\mathrm{d}x} - \Psi(L)\right) &= 0. \end{aligned} \tag{4.51}$$

With those boundary conditions, the frequency equation can be found, which depends both on $b_n^* = b_n \cdot L$ and $a_n^* = a_n \cdot L$.

4.5 Forced Response via Method of Eigenfunktion Expansion

To solve the non-homogeneous linear partial differential equations, the method of *eigenfunction expansion* can be used. Therefore, one has to show, that the corresponding eigenfunctions $\chi_i(x)$ are orthonormal to each other. This is the case, if the eigenfunctions $\chi_n(x)$ of the related homogeneous problem satisfy a regular Strum-Liouville eigenvalue problem in the form of [77]

$$\frac{\mathrm{d}}{\mathrm{d}x}\left(p(x)\frac{\mathrm{d}y}{\mathrm{d}x}\right) + q(x)y = -\lambda r(x)y. \tag{4.52}$$

Then the non-homogeneous solution can be written as a series of eigenfunctions, weighted with a time dependent coefficient

$$y(x,t) = \sum_{n=1}^{\infty} \eta_n(t)\chi_n(x), \tag{4.53}$$

where χ_n denotes the n^{th} eigenfunktion [77, 66]. Using the method of *seperation of variables*, for the Euler-Bernoulli beam (4.20) can be written to match (4.52):

$$\frac{\mathrm{d}}{\mathrm{d}x}\left(-EI\frac{\mathrm{d}^2}{\mathrm{d}x^2}\frac{\mathrm{d}W(x)}{\mathrm{d}x}\right) = -\omega^2\rho A W(x). \tag{4.54}$$

Applying the same procedure to (4.25) for the Timoshenko theory yields

$$\frac{\mathrm{d}}{\mathrm{d}x}\begin{bmatrix}\kappa GA & 0\\ 0 & EI\end{bmatrix}\frac{\mathrm{d}}{dx}\begin{bmatrix}W(x)\\ \Psi(x)\end{bmatrix} + \begin{bmatrix}0 & -\kappa GA\frac{\mathrm{d}}{\mathrm{d}x}\\ \kappa GA\frac{\mathrm{d}}{\mathrm{d}x} & -\kappa GA\end{bmatrix}\frac{\mathrm{d}}{dx}\begin{bmatrix}W(x)\\ \Psi(x)\end{bmatrix} = -\omega^2\begin{bmatrix}\rho A & 0\\ 0 & \rho I\end{bmatrix}\begin{bmatrix}W(x)\\ \Psi(x)\end{bmatrix}. \tag{4.55}$$

Now introducing the Sturm-Liouville operator and the weight function as [77]

$$L(y) = \frac{\mathrm{d}}{\mathrm{d}x}\left(-p(x)\frac{\mathrm{d}y}{\mathrm{d}x}\right) + q(x)y, \qquad M(y) = r(x)y. \tag{4.56}$$

Therefore, one can write (4.54) and (4.55) as

$$L(\boldsymbol{w}_n) = \omega^2 M(\boldsymbol{w}_n), \tag{4.57}$$

with $\boldsymbol{w}_n = W_n(x)$ for the Euler-Bernoulli Theory and $\boldsymbol{w}_n = \begin{bmatrix} W(x) & \Psi(x) \end{bmatrix}^{\mathrm{T}}$ for the Timoshenko theory.

The two operators $L(\boldsymbol{w}_n)$ and $M(\boldsymbol{w}_n)$ are self-adjoint. Therefore, two different eigenfunctions have to satisfy the boundary conditions of a regular Strum-Liouville problem, which is the case when [77, 66]

$$\int_0^L \left(\boldsymbol{w}_n^{\mathrm{T}} L(\boldsymbol{w}_m) - \boldsymbol{w}_m^{\mathrm{T}} L(\boldsymbol{w}_n) \right) \mathrm{d}x = 0. \tag{4.58}$$

For both theories, the integral vanishes due to symmetry after integrating twice by parts and, therefore, the eigenfunctions satisfy a regular Sturm-Liouville problem. One of the facts that are incorporated with this case is, that the eigenfrequencies are complete and are orthogonal to each other with respect to the weight function M [77]

$$\int_0^L \boldsymbol{w}_n^{\mathrm{T}} M(\boldsymbol{w}_n) \mathrm{d}x = \delta_{nm}. \tag{4.59}$$

As the coefficients C_n (4.4, p.20) of the corresponding eigenfunctions $\chi_n(x)$ are unique only to a constant, we can set this constant appropriately that (4.59) is satisfied. From this point on, the forced response can be obtain, which is

$$\boldsymbol{v}(x,t) = \sum_{n=1}^{\infty} \eta_n(t) \boldsymbol{w}_n(x). \tag{4.60}$$

Again, $\boldsymbol{v}(x,t) = v(x,t)$ for the Euler-Bernoulli Theory and $\boldsymbol{v}(x,t) = \begin{bmatrix} v(x,t) & \theta(x,t) \end{bmatrix}^{\mathrm{T}}$ for the Timoshenko theory. Substituting (4.60) into the equations of motion (4.20) and (4.25) and using (4.57) yields

$$\sum_{n=1}^{\infty} \left(\frac{\mathrm{d}^2 \eta_n(t)}{\mathrm{d}t^2} + \omega_n^2 \eta_n(t) \right) M(\boldsymbol{w}_n) = f(x,t). \tag{4.61}$$

Integrating over the beam length and multiplying $\boldsymbol{w}_n^{\mathrm{T}}$ from the left hand side results in

$$\frac{\mathrm{d}^2 \eta_n(t)}{\mathrm{d}t^2} + \omega_n^2 \eta_n(t) = \int_0^L \boldsymbol{w}_n^{\mathrm{T}} f(x,t) \mathrm{d}x, \tag{4.62}$$

which represents a modal state space model of dymension 2n. The initial conditions to use for the simulation are obtained by applying the weight function M to (4.60), multiplying $\boldsymbol{w}_m^{\mathrm{T}}$ from

the left hand side and integrating over the beam length [66]:

$$\int_0^L \boldsymbol{w}_m^{\mathrm{T}} M(\boldsymbol{v}(x,t)\mathrm{d}x = \sum_{n=1}^{\infty} \eta_n(t) \int_0^L \boldsymbol{w}_m^{\mathrm{T}} M(\boldsymbol{w}_n)\mathrm{d}x. \tag{4.63}$$

With $m = n$, (4.63) simplifies due to the orthogonality of eigenfunctions to

$$\eta(t) = \int_0^L \boldsymbol{w}_n^{\mathrm{T}} M(\boldsymbol{v}(x,t)\mathrm{d}x, \tag{4.64}$$

from where $\eta(0)$ can be obtained using $\boldsymbol{v}(x,t=0)$. The solution for the for the forced response finally yields

$$\boldsymbol{v}(x,t) = \sum_{n=1}^{a} \eta_n(t)\boldsymbol{w}_n(x), \tag{4.65}$$

where a denotes the number of considered natural frequencies and modes.

4.6 Model Validity for different geometries

To establish a statement about the validity of the Euler-Bernoulli theory, one has to consider the beam's thickness which corresponds with the influence of shear and the rotary inertia [66]. Therefore, the slenderness ratio sr is introduced, which is defined as

$$sr = L\sqrt{\frac{A}{I}}. \tag{4.66}$$

Roughly said, the slenderness ratio increases if the beam structure's thickness decreases. Various researchers have made predictions about the correctness of the beam theories depending on the slenderness ratio. While HAN *et al.* propose the use of the Timoshenko theory for $sr < 100$, VANRENSBURG *et al.* and LABUSCHAGNE *et al.* suggest this theory for $sr < 34$ [66, 78, 79]. In the static case, GROSS *et al.* claim validity for the Euler-Bernoulli theory, when $sr > 17$ [68]. To express a clear statement on this issue, the error made by the Euler-Bernoulli theory has been investigated for both the dynamic and the static case.

4.6.1 Dynamic Case - Prediction of Eigenfrequencies

As shown in (4.4.1, p.21) the frequency equation of the Euler-Bernoulli theory depends only on one sort of dimensionless wave numbers a_n^*. With the dispersion relationship given by (4.28) the natural frequencies for a beam of specified length and material can be found using

$$\omega_n L\sqrt{\frac{\rho}{E}} = \frac{a_n^{*2}}{sr}. \tag{4.67}$$

Note that for the Euler-Bernoulli case a_n^* depends only on the boundary conditions and is independent of the structure's geometry or material.

Cross section	Shear correction factor κ	numerical value for $\nu = 0.5$
Circle	$\frac{6(1+\nu)}{7+6\nu}$	0.9
Rectangle	$\frac{10(1+\nu)}{12+11\nu}$	0.857
Hollow circle	$\frac{6(1+\nu)(1+m^2)^2}{(7+6\nu)(1+m^2)^2+(20+12\nu)m^2}$ $m = \frac{R_i}{R_o}$	-
Thin walled square	$\frac{20(1+\nu)}{48+39\nu}$	0.444

Table 4.2: Shear correction factor κ for different cross sections [81]. Note that κ depends on the Poisson's ratio ν. For $\nu = 0.5$ the numerical values for the shear correction factors are between 0.55 - 0.9.

As opposed to this, the frequency equation of the Timoshenko theory depends on both a_n^* and b_n^* and, therefore, the dispersion relationship has to be established. Here, we will outline the procedure for $\omega < \omega_c$. Analogue to that, one can derive the dispersion relationship for $\omega > \omega_c$: a_n and b_n from (4.44) can be written in in terms of

$$B_1 = \frac{\rho\omega_n^2}{2E}, \qquad B_2 = \frac{\rho\omega_n}{2\kappa G} = B_1 \cdot \Gamma^2, \qquad B_3 = \frac{\rho A\omega_n^2}{EI}, \tag{4.68}$$

which yields

$$\begin{aligned} \frac{a_n^*}{L} &= \sqrt{B_1(1+\Gamma^2) + \sqrt{B_1^2(1-\Gamma^2)^2 + B_3}}, \\ \frac{b_n^*}{L} &= \sqrt{-B_1(1+\Gamma^2) + \sqrt{B_1^2(1-\Gamma^2)^2 + B_3}}. \end{aligned} \tag{4.69}$$

Γ^2 is the relationship of Young's and shear modulus in ratio to the shear correction factor κ and is defined as:

$$\Gamma^2 = \frac{2(1+\nu)}{\kappa}. \tag{4.70}$$

Since κ also depends on the Poisson's ratio as shown in tab:.4.2 (p.28), Γ^2 combines the information about the beam structures material. Here, ν is called the Poisson's ratio an varies from 0.1 -0.55 [80].

Now solving for B_1 and B_3 results in

$$B_1 = \frac{a_n^{*2} - b_n^{*2}}{2(1+\Gamma^2)L^2}, \qquad B_3 = \frac{1}{4L^4}\left[(a_n^{*2} + b_n^{*2})^2 - \frac{(1-\Gamma^2)^2}{(1+\Gamma^2)^2}(a_n^{*2} - b_n^{*2})^2\right], \tag{4.71}$$

from which the ratio of B_1 and B_3 can be obtained:

$$\frac{(\Gamma^2 b_n^{*2} + a^{*2})(\Gamma^2 a_n^{*2} + b_n^{*2})}{(a_n^{*2} - b_n^{*2})(1+\Gamma^2)} = sr^2. \tag{4.72}$$

This states, that the relationship between a_n^* and b_n^* depends on the slenderness ratio sr of the beam, the shape factor κ of the cross section and the Poisson's ratio ν of the used material.
With (4.68) and (4.72), (4.48) can be expressed in terms of dimensionless wave numbers only:

$$\begin{aligned} D_1 &= -\frac{a_n^{*2} + \Gamma^2 b_n^{*2}}{(1+\Gamma^2) a_n^* L} C_2, \qquad & D_2 &= \frac{a_n^{*2} + \Gamma^2 b_n^{*2}}{(1+\Gamma^2) a_n^* L} C_1, \\ D_3 &= -\frac{b_n^{*2} + \Gamma^2 a_n^{*2}}{(1+\Gamma^2) b_n^* L} C_4, \qquad & D_4 &= \frac{b_n^{*2} + \Gamma^2 a_n^{*2}}{(1+\Gamma^2) b_n^* L} C_3. \end{aligned} \tag{4.73}$$

Therefore, we can now derive the frequency equation also in terms of dimensionless wave numbers only:

$$\begin{aligned} 0 = (a_n^{*2} - b_n^{*2}) \sin(a_n^*) \sinh(b_n^*) - \\ -a_n^* b_n^* \frac{a_n^{*4} + a_n^{*4}\Gamma^4 + 4a_n^{*2} b_n^{*2}\Gamma^2 + b_n^{*4}\Gamma^4 + b_n^{*4}}{(a_n^{*2}\Gamma^2 + b_n^{*2})(a_n^{*2} + b_n^{*2}\Gamma^2)} \cos(a_n^*) \cosh(b_n^*) - 2a_n^* b_n^*. \end{aligned} \tag{4.74}$$

With B_3 from (4.68) and (4.71) we can now compute the natural frequencies of a specified beam:

$$\omega_n L \sqrt{\frac{\rho}{E}} = \frac{1}{2sr} \sqrt{(a_n^{*2} + b_n^{*2})^2 - \frac{(1-\Gamma^2)^2}{(1+\Gamma^2)^2} (a_n^{*2} - b_n^{*2})^2}. \tag{4.75}$$

Note that for $a_n^* = b_n^*$, the frequency equation and, therefore, the natural frequencies of a specified beam described by the theory match the ones of the Euler-Bernoulli theory. This is the case for higher sr as we will see following.
Fig:.4.5 (p.4.5) shows the over prediction of the first four natural frequencies for clamped-free beams of unspecified material and length, made by the Euler-Bernoulli theory. Γ^2 varies in a range of 2.5 - 5.5 depending on the beams material and cross section as seen in (4.70). For a thin walled elastomer tube $\Gamma^2 = 5.5$ which can be considered as a relatively high value. For suche structures the Euler-Bernoulli theory tends to over predict the natural frequency with lower values of $1/sr$ compared to e.g. a cylindrical steel beam, $\Gamma^2 = 2.5$. As well, for higher wave numbers, the over prediction of the natural frequencies occurs with lower values of sr, see fig:.4.5 (p.4.5). In (**??**), we pointed out, that the step response of our critically damped system shows satisfying accuracy for v and θ when we consider the first 25 wave numbers. Because of this findings, we recommend to use the Timoshenko theory for dynamical analysis.

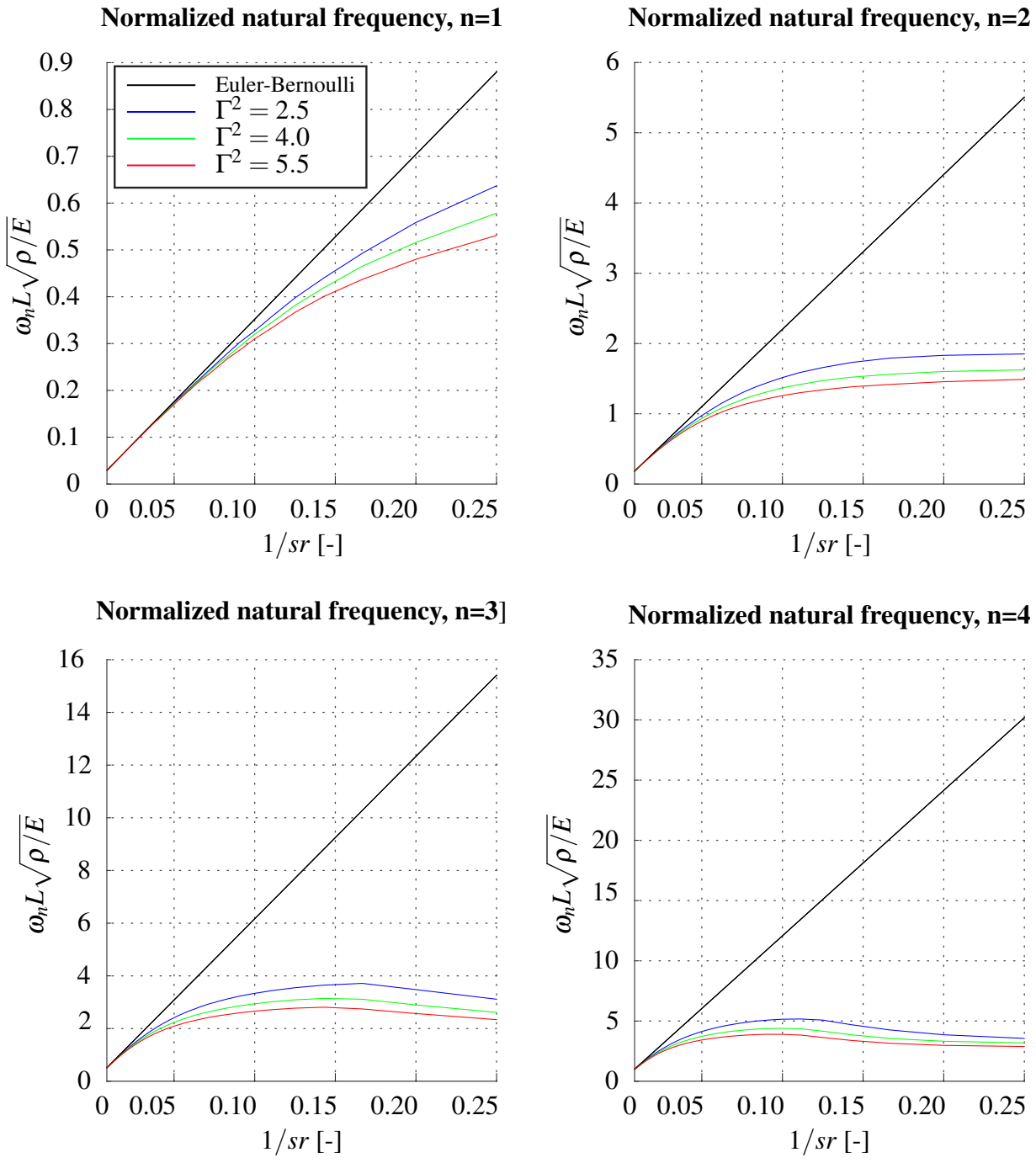

Figure 4.5: First four natural frequencies for clamped-free beams of unspecified material and length predicted by the Euler-Bernoulli and the Timoshenko theory for differnt Γ^2. Note as the higher the wave number increases, the error between the two theories increase.

4.6.2 Static Response - Shear Deformation Error

Within the static case one has to take closer look at the effect of shear deformation to predict the error made by the Euler-Bernoulli theory.
For a lateral force F at $x = l$, no distributed load $q(x) = 0$ and no moments M along the beam, we can apply following boundary conditions at the free end:

$$Q(l) = F, \qquad M(l) = 0. \tag{4.76}$$

Solving the statical differential equations of bending (4.12) and (4.13) then yields for the plane angle and deflection:

$$v'_{eb}(x) = \frac{Fl}{EI}x - \frac{F}{2EI}x^2, \qquad \theta_{ts}(x) = \frac{Fl}{EI}x - \frac{F}{2EI}x^2, \tag{4.77}$$

$$v_{eb}(x) = \frac{Fl}{2EI}x^2 - \frac{F}{6EI}x^3, \qquad v_{ts}(x) = \frac{Fl}{2EI}x^2 - \frac{F}{6EI}x^3 + \frac{F}{\kappa GA}x. \tag{4.78}$$

One can see, that the $v'_{eb}(x) = \theta_{ts}(x)$, but $v_{ts}(x)$ experiences an additional deflection $Fx/\kappa GA$, which we call the shear deformation.
Now we assume two beams undergoing the same concentrated tip load $F_{eb} = F_{ts} = F$, but following different theories. With (4.77), (4.78) turns into:

$$v_{ts}(L) = v_{eb}(L)\left(1 + \frac{3EI}{l^2\kappa GA}\right). \tag{4.79}$$

With the slenderness ratio sr from (4.66) and Γ^2 from (4.70), (4.79) then is simplified to

$$v_{ts}(L) = v_{eb}(L)\underbrace{\left(1 + \frac{3\Gamma^2}{sr^2}\right)}_{SDE}, \tag{4.80}$$

where the constant factor on the right hand side is called the shear deformation error (SDE) and depends on the shear correction factor κ, the Poisson's ratio ν and the slenderness ratio sr.
Now, this proceeder is repeated for two beams underlying the same tip deflection $v(L) = v_{eb}(L) = v_{ts}(L)$ but different forces. See, that in this case the plane angels differ from each other by,

$$\theta_{ts}(L) = \frac{v'_{eb}(L)}{SDE}, \tag{4.81}$$

Fig:4.6 (p.32) shows a schematic sketch of the SDE in both cases. For equal tip forces the Timoshenko beam bends more, with the help of the shear deformation, while the tip plane angles remain equal for both models. The SDE for equal tip deflections induces a back-shift of the tip plane angel in the Timoshenko theory. In opposite to that, the tip deflection for both models

remains equal. For the static case, we considered a SDE of 3% as acceptable. Fig.4.7 (p.33)

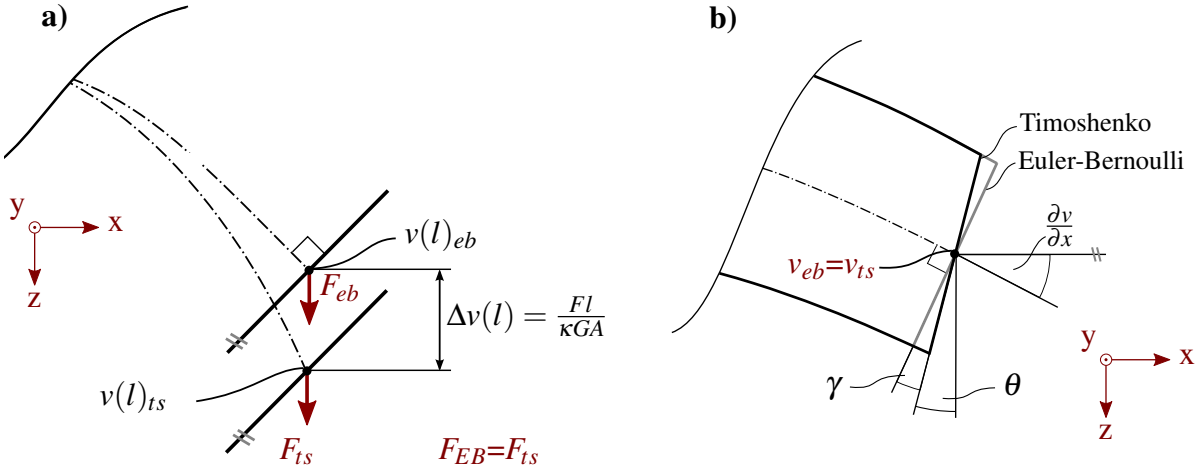

Figure 4.6: Schematic explanation of the shear deformation error. a) For equal tip forces, the Timoshenko beam bends more, with the help of the shear deformation. Note that the tip plane angle in the Timoshenko beam is equal to the tip plane angle in the Euler-Bernoulli theory. b) For an equal tip deflection, the Timoshenko theory induces a back-shift of the plane anqle, γ. Here, the tip forces used to reach the displacement differ from each other

shows the progress of the SDE for degreasing sr. The point of 3% error occures for $sr = 40$, which is why we recommend to consider the Thimoshenko theory for geometries with $sr < 40$. Note that for $sr = 40$, the SDE is little depending on Γ^2.

4.6.2.1 Concentrated tip Moment

Another finding is, that for the absence of shear, the SDE vanishes, which can be seen easily by applying appropriate boundary conditions and solving (4.12) and (4.13). Those Boundary conditions are a concentrated tip moment $M_{eb}(l)$, no distributed load $q(x) = 0$ and no lateral Force $Q(x) = 0$ along the beam:

$$v'_{eb}(x) = \frac{M}{EI}x, \qquad \theta_{ts}(x) = \frac{M}{EI}x, \tag{4.82}$$

$$v_{eb}(x) = \frac{M}{2EI}x^2, \qquad v_{ts}(x) = \frac{M}{2EI}x^2.$$

4.7 Kinematic Modelling

The kinematics of a bending beam can be described using the Frenet-Serret formulas. In differential geometry, these formulas describe the kinematic properties of a particle which moves along a continuous, differentiable curve in Euclidean space. The curve of the particles along the centre line of the beam width length L thus can be described by the curve vector $r(s)$ where s is

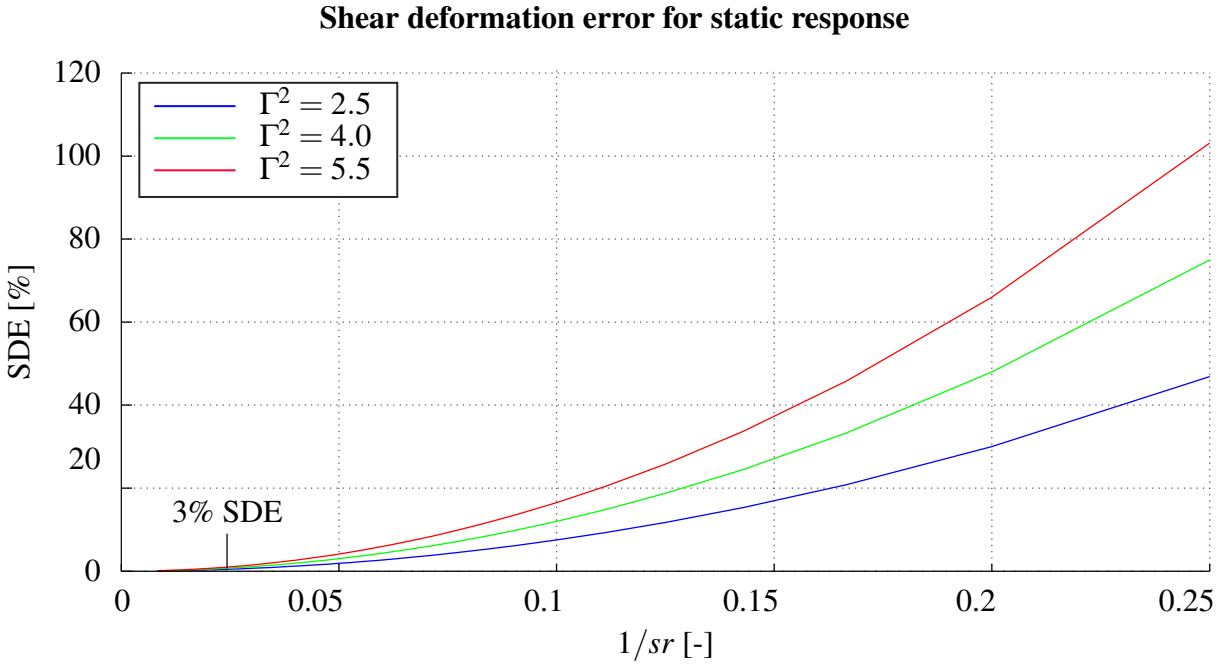

Figure 4.7: Progress of the SDE for different Γ^2. For $sr < 40$, the Timoshenko theory shoud be taken into account, because the tollerable error of 3% is exceeded.

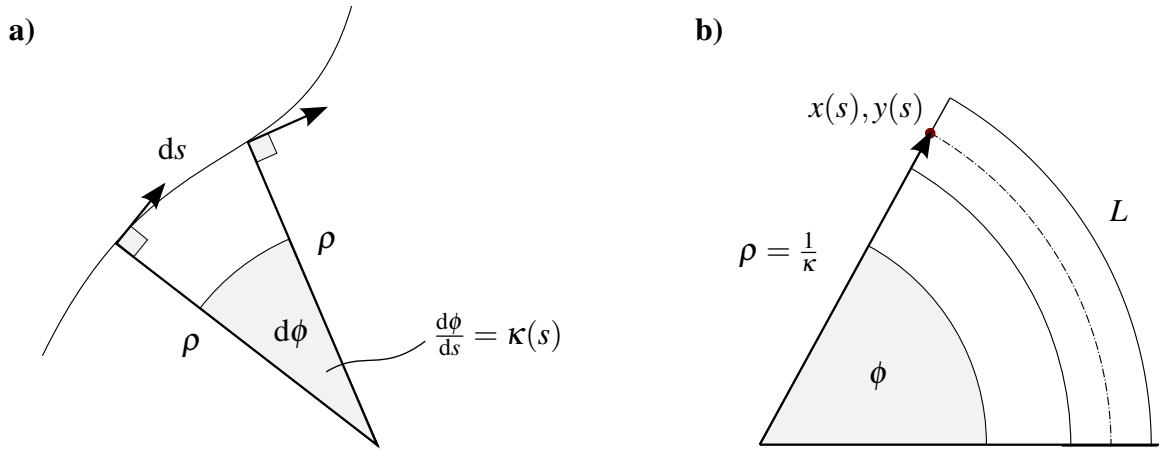

Figure 4.8: a) Formulas of Frenet-Serret from which the CC approximation can be derived. b) For a constant k, the beam describes a circle segment of length L with radius ρ. For the general loading case of a concentrated tip moment, the CC approximation posses validity.

the arc length parameter, see Fig. 4.8a (p.33), and

$$L = \int_0^L \sqrt{(r'(s)^2)}\mathrm{d}s, \qquad r'(s) = \frac{\mathrm{d}r(s)}{\mathrm{d}s}. \tag{4.83}$$

For an infinitesimal small segment ds of a bended beam due to a general loading, see Fig.4.8 (p.33, the particles of the centre line lie on a circle with radius ρ and the inclined angle d$\phi(s)$ is

$$\mathrm{d}\phi(s) = \frac{\mathrm{d}s}{\rho(s)}, \qquad \frac{\mathrm{d}\phi(s)}{\mathrm{d}s} = \frac{1}{\rho(s)} = k(s), \tag{4.84}$$

where $k(s)$ is called the curvature of the centre line. To find $k(s) = \mathrm{d}\phi(s)/\mathrm{d}s$, we use

$$\frac{\mathrm{d}\phi(s)}{\mathrm{d}s} = \frac{\mathrm{d}\phi(s)}{\mathrm{d}x(s)} \cdot \frac{\mathrm{d}x(s)}{\mathrm{d}s} \tag{4.85}$$

where $x(s)$ is the x-coordinate of a particle at s, see Fig.4.8a (p.33). With

$$\phi(s) = \arctan\left(\frac{\mathrm{d}y(s)}{\mathrm{d}x(s)}\right) \tag{4.86}$$

and

$$\mathrm{d}s = \sqrt{\mathrm{d}x(s) + \mathrm{d}y(s)}, \tag{4.87}$$

(4.85) gets:

$$k(s) = \frac{\mathrm{d}\phi(s)}{\mathrm{d}s} = \frac{\mathrm{d}}{\mathrm{d}x}\arctan\left(\frac{\mathrm{d}y(s)}{\mathrm{d}x(s)}\right) \cdot \frac{1}{\frac{\mathrm{d}s}{\mathrm{d}x}} \tag{4.88}$$

$$= \frac{\frac{\mathrm{d}^2y(s)}{\mathrm{d}x(s)^2}}{1 + \left(\frac{\mathrm{d}y(s)}{\mathrm{d}x(s)}\right)^2} \cdot \frac{1}{\sqrt{1 + \left(\frac{\mathrm{d}y(s)}{\mathrm{d}x(s)}\right)^2}} \tag{4.89}$$

For the present approach of CC, $k(s) = k$, equation (4.85) becomes

$$\frac{\mathrm{d}\phi(s)}{\mathrm{d}s} = k = \underbrace{\frac{\mathrm{d}\phi(s)}{\mathrm{d}x(s)}}_{=1} \cdot \frac{\mathrm{d}x(s)}{\mathrm{d}s} \tag{4.90}$$

$$\frac{1}{k} = \rho = \sqrt{1 + \left(\frac{\mathrm{d}y(s)}{\mathrm{d}x(s)}\right)^2} \tag{4.91}$$

and, therefore, the curvature k of the centre line of the beam describes a circle segment of length L with radius ρ, whereas the coordinates of a particle on the centre line are

$$x(s) = \rho sin(\phi(s)) \tag{4.92}$$
$$y(s) = \rho(1 - cos(\phi(s))) \tag{4.93}$$

see Fig.4.8b (p.33).

Relation to classical Beam Theory

The Euler-Bernoullie Beam Theory and the Timoshenko Beam Theory have both in common, that they assume small displacements of the centre line of the beam while loaded. To be more specific, they assume that the angle between the tangent and the x-axis of the global reference frame is small. Therefore, (4.86) becomes

$$\underbrace{tan(\phi(s))}_{=\phi(s)} = \frac{\mathrm{d}y(s)}{\mathrm{d}x(s)} \tag{4.94}$$

Here, the tangent $\mathrm{d}y(s)/\mathrm{d}x(s)$ at s is considered to be small ($(\mathrm{d}y(s)/\mathrm{d}x(s))^2 << 1$) and, therefore, the curvature $k(s)$ (4.89) gets

$$k(s) = \frac{\mathrm{d}^2 y(s)}{\mathrm{d}x(s)^2} \tag{4.95}$$

which converges with the classical beam theories, see (4.82).

4.8 Extended Modelling

4.8.1 Damping

Damping is included in the equation of motions to reproduce the dynamical behaviour of the compliant mechanism. In general, the presence of damping affect the equations of motion by a additional linear term. With this additional term, the modal representation of the equations of motions are not generally decoupled [66]. Therefore, the identification of an appropriate damping model and its respective parameter is a challenging task since all relevant modes and their damping need to be exited thoroughly. The present testbed does not incorporate the necessary properties as it was not the focus of this thesis. However, a coarse damping analysis will be presented in (6.3, p.75), to give an idea about the dynamic characterisitc of the compliant mechanism. To do so, we assume a constant modal damping coefficient ζ that decouples the modal representation of the equation of motion for the ith eigenfrequency:

$$\ddot{\eta}_i + 2\zeta\omega_i \cdot \dot{\eta}_i + \omega_i^2 \cdot \dot{\eta}_i = W_i(x) \cdot f(x,t). \tag{4.96}$$

4.8.2 Material Non-Linearities

As described in (3, p.12) the compliant mechanism's material was chosen to be an elastomer to allow higher lateral displacement achieved with moderate forces. While this fact may avoid plastic deformation, it is highly probable, that it will result in an elastic non-linearity. As seen in Tab.4.1 (p.14), both the Euler-Bernoulli and the Timoshenko theory do not provide non-linear material behaviour. The aim of the following consideration is to establish a method of including non-linear material behaviour into the solution of the forced response, without the need of executing the modal analysis anew for each change in the material parameters. As we saw in (4.6, p.27), the n^{th} natural frequency ω_n depends on the Young's Modulus E, the mass density ρ, the beam length L and the corresponding dimensionless wave numbers a^* and b^*, as seen in (4.67) and (4.75). Therefore, it is clear, that we can determine the dimensionless wave numbers once for a beam with specified boundary conditions, and obtain the natural frequencies by scaling a^* and b^* with the aforementioned parameters. If a change in the Young's modulus occurs, the resulting natural frequency can be computed without the need of executing the modal analysis anew.

As we determine the wave numbers from the frequency equations, the mode shapes are independent from the materials parameters. Therefore, the set of linear equations (4.32) is solved in terms of a^* and b^* for the Euler-Bernoulli theory and additionally in therms of Γ^2 and with the help of (4.73) for the Thimoshenko theory. For the Euler-Bernoulli theory, this is

$$C_1 = \frac{\cosh(a^*) + \cos(a^*)}{\sinh(a^*) + \sin(a^*)}, \tag{4.97}$$

$$C_2 = -1, \tag{4.98}$$

$$C_3 = -\frac{\cosh(a^*) + \cos(a^*)}{\sinh(a^*) + \sin(a^*)}, \tag{4.99}$$

$$C_4 = 1. \tag{4.100}$$

For the Thimoshenko theory, we derive

$$C_1 = \frac{a^* \left(a^{*2}\Gamma^2 \cosh(b^*) + b^{*2}\Gamma^2 \cos(a^*) + b^{*2} \cosh(b^*) + a^{*2} \cos(a^*)\right)}{\left(b^{*2}\Gamma^2 + a^{*2}\right)\left(b^* \sinh(b^*) + a^* \sin(a^*)\right)}, \tag{4.101}$$

$$C_2 = -1, \tag{4.102}$$

$$C_3 = -\frac{b^* \left(a^{*2}\Gamma^2 \cosh(b^*) + b^{*2}\Gamma^2 \cos(a^*) + b^{*2} \cosh(b^*) + a^{*2} \cos(a^*)\right)}{\left(a^{*2}\Gamma^2 + b^{*2}\right)\left(b^* \sinh(b^*) + a^* \sin(a^*)\right)}, \tag{4.103}$$

$$C_4 = 1. \tag{4.104}$$

The obtained coefficients C_i have to be normalized with respect to each other using (4.59). See, that only the Poisson's ratio ν , contained by Γ^2 contributes a dependency of the material within the mode shapes. Therefore, we need to assume a constant Poisson's ratio ν, for the aforementioned relationships to hold. We will see for the used elastomer,in (5.4, p.52), this is the case. Therefore, no effect on the mode shapes is considered by the influence of a non-linear material behaviour. Note that (4.101) is valid for $\omega_n < \omega_c$. For $\omega_n > \omega_c$, one can repeat the steps analogously.

4.9 Finite Element Modelling of the Classical Beam Theories

To provide a cross-validation of the analytical solution of the classical beam theories postulated in (4.3, p.18), the finite element method (FEM) was used. This numerical method solves the problem by finding an approximation function for the weak formulation of the governing equations of motion [82]. Following, the basic process of applying the FEM to a beam structure is outlined, based on the work of KWON *et al.*, see [83]:

1. The beam is separated into a finite number of elastic elements *nde*, which are interconnected by $n = nde + 1$ nodes. Those nodes are considered as having mass, while the interconnections are modelled as massless springs. The state of every node is described by a set of variables $\boldsymbol{d}_i$, called the element nodal variables, see Fig.4.9 (p.38). In our case, we use the deflection v and the plane angle θ as nodal variables. Therefore, we derive four variables per element, namely v_i, θ_i at the beginning node and v_{i+1}, θ_{i+1} at the ending node, for $i = 1...m$.

2. Accordingly to KWON *et al.*, a set of continuous function *bmh* have to be defined, to interpolate between two nodal states:

$$\boldsymbol{d}_i = \begin{pmatrix} v_i \\ \theta_i \end{pmatrix}. \tag{4.105}$$

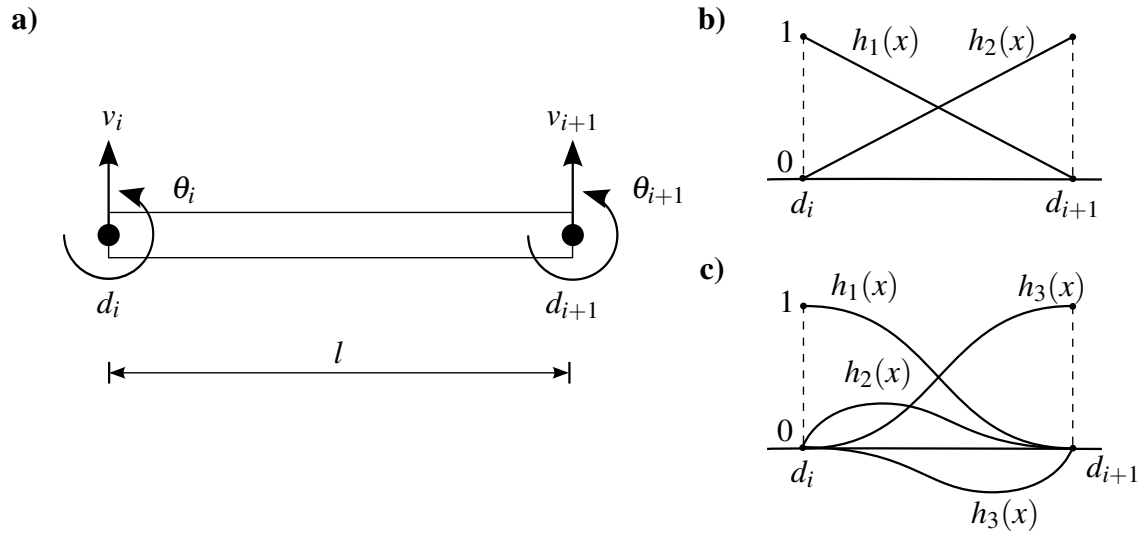

Figure 4.9: FEM Modelling of a beam structure: a) Discrete beam element consisting of two nodes and a massless interconnection of length l. Every nodal state $\boldsymbol{d}_i$ is described by the use of two variables v_i and θ_i. b) Linear shape functions used for the Timoshenko theory. c) *Hermitian* shape function used for the Euler-Bernoulli theory.

For the Euler-Bernoulli theory, we use *Hermitian* shape functions, while for the Timoshenko theory, we use linear shape function, see Fig.4.9 (p.38). This is because with the use of *Hermitian* shape functions, we can propose a certain cubic approximation function for v and θ, where $\theta = \mathrm{d}v/\mathrm{d}x$ and, therefore, fulfil the Euler-Bernoullian assumption.

3. The element stiffness matrix $\boldsymbol{K}_i \in \mathbb{R}^{4x4}$ and element mass matrix $\boldsymbol{M}_i \in \mathbb{R}^{4x4}$ are computed using *Galerkins'* method for the Euler-Bernoulli and the energy method for the Timoshenko theory, see [83]. Those matrices having the dimension correlated to the number of nodal variables per element. Every single element matrix is combined to derive the system matrices $\boldsymbol{K} \in \mathbb{R}^{2nx2n}$, $\boldsymbol{M} \in \mathbb{R}^{2nx2n}$. Accordingly, the systems nodal variable vector $\boldsymbol{d}$, $\in \mathbb{R}^{2n}$ is derived. Note that per definition, $\boldsymbol{M}$ is always positive definite, while $\boldsymbol{K}$ is positive semi-definite and furthermore, both matrices are symmetrical. This is because a system's mass is always > 0, while a system's stiffness can be ≥ 0. Now, the geometrical boundary conditions are applied to the $\boldsymbol{K_s}$ by setting the corresponding row and column entries to zero and the entry on the main diagonal to 1, see [83].

4. An advantage of the FEM analysis of beam structures is the possibility of composing complex force and moment progressions along the beam. Those progressions are described within the system's excitation vector $\boldsymbol{f_t}$, $\in \mathbb{R}^{2n}$. To oppose a concentrated load at a specified node i, one has to change the corresponding $\boldsymbol{f}_{t,i}$. Analogue, for opposing a concentrate moment at this node, one has to change the entry corresponding to $f_{t,i+1}$.

5. Now, the system's equations of motion can be described by:

$$\boldsymbol{M} \cdot \ddot{\boldsymbol{d}} + \boldsymbol{K} \cdot \boldsymbol{d} = \boldsymbol{f_t}. \tag{4.106}$$

A modal analysis can be conducted, analogue to (4.5, p.25), where the natural frequencies and mode shapes can be derived by solving the generalized eigenvalue problem:

$$(\boldsymbol{K} - \omega^2 \boldsymbol{M}) = 0 \tag{4.107}$$

Because $\boldsymbol{K}$ and $\boldsymbol{M}$ are positive definite and positive semi-definite, the mode shapes corresponding to (4.107) are orthogonal with respect to the system matrices, see [84].

4.10 Control Model

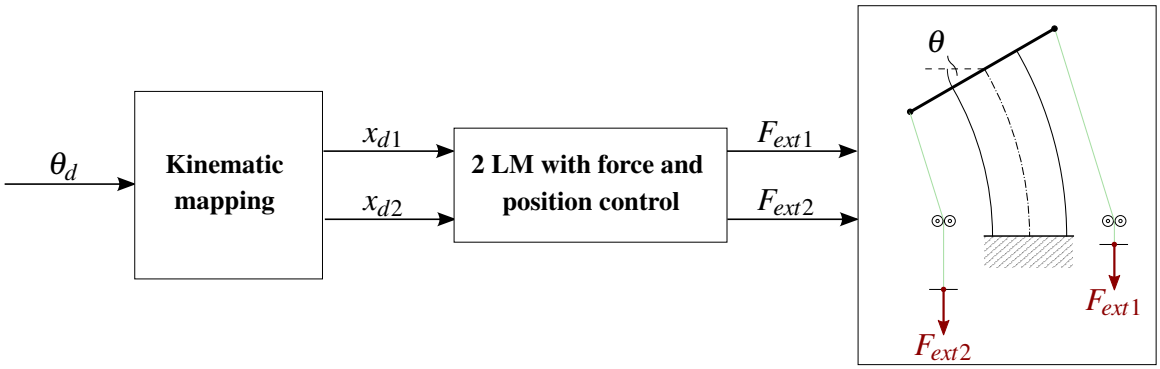

Figure 4.10: Block diagram of the controller model. The distance covered by the linear motor units is derived using the CC approximation and a kinematic mapping described below. With this distances an impedance controller is feeded, see JACOBSEN *et al.*[85].

The aim of the controller that needs to be developed is to control the tip angle $\theta(L)$ of the compliant mechanism. As stated before, no additional sensor at the compliant mechanism shall be used for the controller due to the practical relevance. Thus, the measured quantities that can be used in the feedback of the control algorithm are the tendon forces F_{ext1}, F_{ext2} and the positions of the linear motors x_{LM1}, x_{LM2}. To control the tip angle $\theta(L)$ with an actuation via tendons, it has to be considered that tendons can go slack due to friction or other unwanted effects in the drive train. Therefore, a pretension force $F_{Pre} > 0$ needs to be ensured. A control law, that incorporates the position control of each linear motor as well as a guaranteed pretension of the tendons is proposed in [85]. The essential equation of the control loop are

$$m_{LMi} \cdot \ddot{x}_{LMi} = F_c - F_{ext,i}, \tag{4.108}$$

where $m_{LM,i}$ and $x_{LM,i}$ is the mass and the position of the ith linear motor, $F_{ext,i}$ is the external

force e.g. the tendon force and F_c is the control force with

$$F_c = K_f \cdot \underbrace{(F_{pre} - F_{ext,i}}_{Pretension\ \ Control} \underbrace{+ K_p \cdot (x_{d,LMi} - x_{LMi}) - K_d \cdot (\dot{x}_{LMi}))}_{Position\ \ Control}. \tag{4.109}$$

Now, to control the tip angle θ of the compliant mechanism, a kinematic mapping needs to be established that transforms desired tip angles $\theta_d(L)$ into a desired motor position $x_{d,LM1,2}$ which serves as an input set point for the position control law (4.109). The block diagram of this overall control concept is illustrated in Fig.4.10 (p.39). This kinematic mapping is described in the following by the use of Fig.4.11 (p.41). To command a desired tip angle *theta* we use the (4.92) to compute the complaint mechanism's tip position $\boldsymbol{p}$. With θ_d and $_p$, we derive $\boldsymbol{p_2}$ and $\boldsymbol{p_1}$ by the use of

$$\boldsymbol{p_2} = \begin{bmatrix} \boldsymbol{p_x} - l\sin(\theta_d) \\ \boldsymbol{p_x} + l\cos(\theta_d) \end{bmatrix}, \quad \boldsymbol{p_1} = \begin{bmatrix} \boldsymbol{p_x} + l\sin(\theta_d) \\ \boldsymbol{p_x} - l\cos(\theta_d) \end{bmatrix}, \tag{4.110}$$

where l is the length of the lever arm. Now, the distance to be covered by the actuating and linear motor computes as

$$\Delta x_i = L_0 - L_i - L_c, \tag{4.111}$$

where L_c is the length of the circle segment described by γ_i and r and L_i computes as

$$L_i = \sqrt{p_{i,y} - l - r(1-\cos[\gamma_i))^2 + (L_0 + p_{i,x} - hr_i - r\sin(\gamma_i))^2)}, \tag{4.112}$$

with γ_i implicitly given by

$$\begin{aligned} \tan(\gamma_2) &= -\frac{p_{2,y} - l - r(1-\cos(\gamma_2))}{L_0 + p_{2,x} - hr_2 - r\sin(\gamma_2)} \\ \tan(\gamma_1) &= -\frac{p_{1,y} - l - r(1-\cos(\gamma_1))}{L_0 + p_{1,x} - hr_1 - r\sin(\gamma_1)}. \end{aligned} \tag{4.113}$$

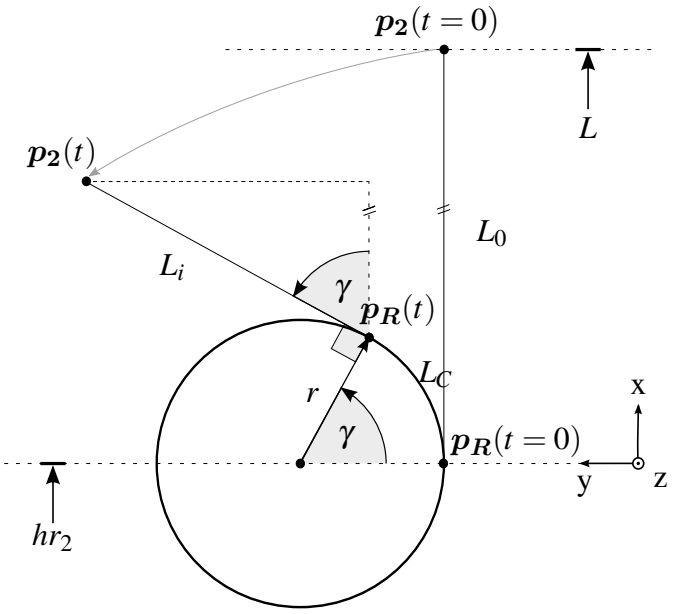

Figure 4.11: Kinematic mapping between tip angle and actuator position

5 Testbed Design

5.1 Overall Design and Measured Quantities

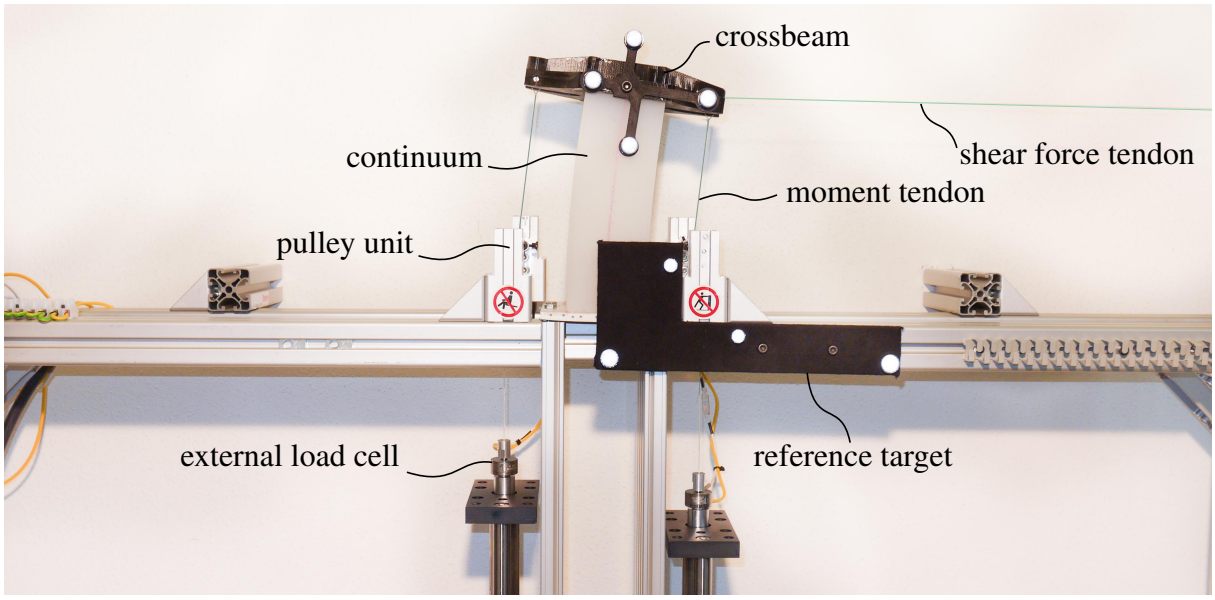

Figure 5.1: The testbed with the compliant mechanism: The frame was built up using ITEM profiles. The actuation was realised by tendons using four linear motors. To measure tendon forces, four external load cells were mounted onto the linear motors. The tip position and angle was tracked using the ARTtrack2® System.

In this section, the design of the testbed is described. First of all, an overview will be given followed by design specifications of the compliant mechanism. Afterwards, the special routing of the tendon will be explained. This section closes with the parameter estimation for the material properties.

For the first experiments we focused on investigating the planar case, in which we aimed to reproduce bending by an external tip moment or tip shear force.

To apply those forces, an actuation via Dyneema® tendons was chosen, because they are easy to configure and allow high tendon force [86]. Furthermore it is possible to redirect tendons by the use of pulleys, which is necessary to achieve a force transmission as it is explained in (5.3.1, p.48). The use of tendons suggest an antagonistic placement of the motors for realizing the actuation. This is, because such a mechanism shows better active and passive performance and ensures that tendons would not go slack [85]. As well, with an antagonist actuation, one is able to oppose a pretension to the structure.

Four linear motors were used to actuate the tendons. Two of them were placed in vertical orientation for the moment actuation. In this case, the tendons were routed with pulleys and mounted to the crossbeam on the structures tip, which acts as a lever arm. For the introduction

of concentrated shear force, the other two linear motors were placed on the left and right hand side at the same level as the mechanism's tip. The test stand itself was constructed using ITEM® profiles and provides flanges on which the base plates of different structures and the motors can be mounted.

Quantities of interest have been the motor's positions and forces, the tendon forces and the structures tip position and angle. Tab.5.1 (p.**??**) shows an overview of them. The linear motors are capable of sensing their desired motor forces and positions. For the measurement of tendon forces, four external load cells were mounted onto each liner motor's tip. The ARTtrack2® system, consiting of two infra-red (IR) cameras, was used to track the structures tip position and angle. Therefore, two marker targets, which reflect the IR emissions, were used. The target for the tool center point (TCP) was mounted to the structures tip, while the reference target was mounted to the testbed's frame.

Motor positions	Intrinsic position sensing	x_{LM1}, x_{LM2}, x_{LM5}, x_{LM4}
Motor forces	Intrinsic force sensing	F_{LM1}, F_{LM2}, F_{LM5}, F_{LM4}
Tendon forces	External load cells	F_{ext1}, F_{ext2}, F_{ext5}, F_{ext4}
Tip pose	ARTtrack2® system	v_{tip}, x_{tip}, θ_{tip}

Table 5.1: Quantities of interest measured by the test stand's components.

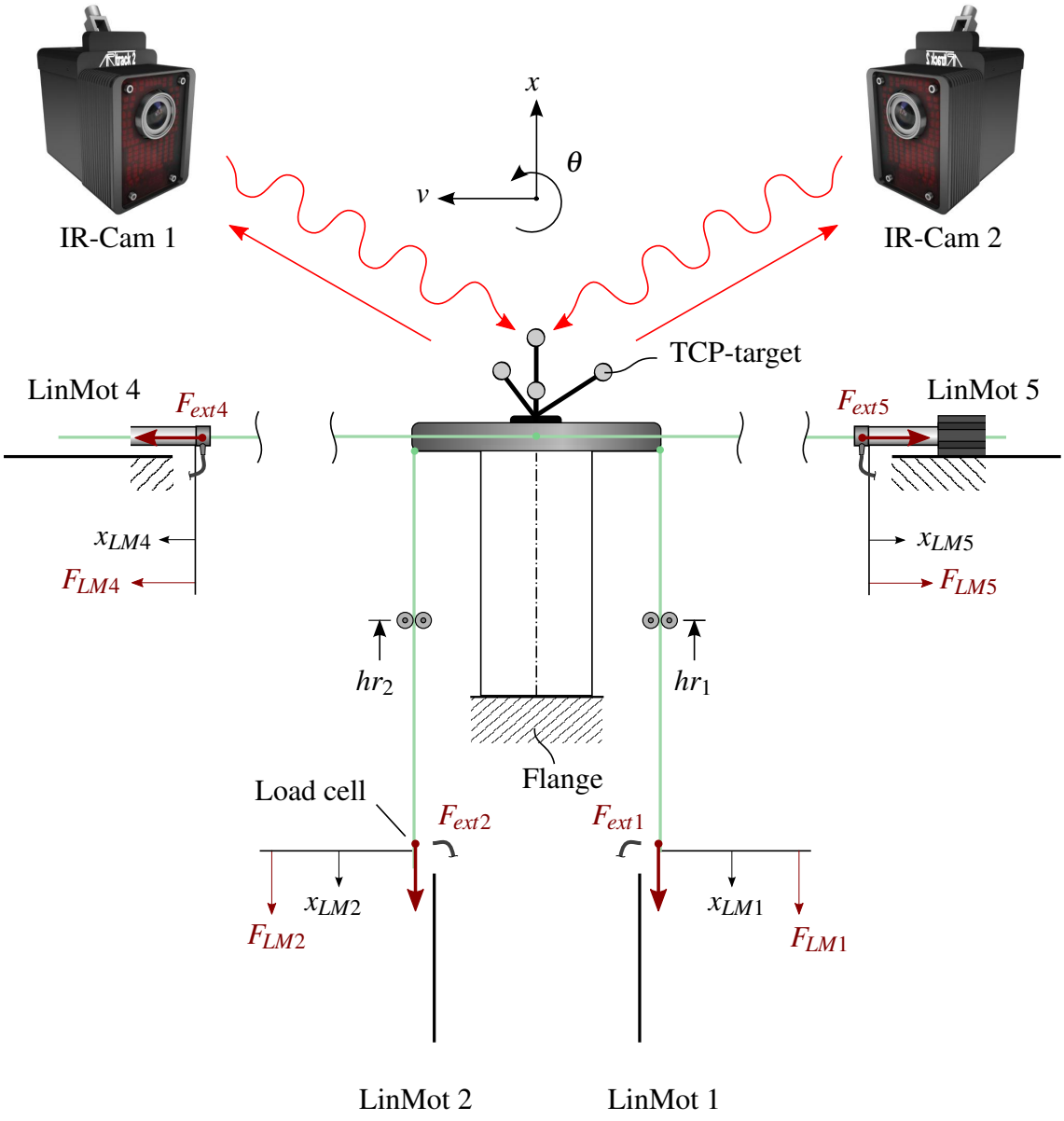

Figure 5.2: Schematic drawing of the test stand design and it's components

5.2 Compliant Mechanism

5.2.1 Mechanical Design

The flexible structure of the compliant mechanism was designed to meet following four requirements:

1. the bending stiffness of one direction has to be a lot higher than the other, so one can assume a 2D-bending mechanism
2. the geometry's slenderness ratio has to be in a range that one can measure a significant difference between the Euler-Bernoulli and the Timoshenko theory and furthermore, buckling is avoided.
3. under a reasonable load, the geometry has to allow at least $\pm 30^\circ$ deflection angle
4. the geometry has to be suitable for position tracking

The first requirement is met by the use of a rectangular surface, since for those geometries, the flexural rigidity in z-direction is a lot stiffer as in y-direction when $h < b$ [80]:

$$I_y = \frac{hb^3}{12} \quad << \quad I_z = \frac{bh^3}{12}. \tag{5.1}$$

The second requirement was met by the choice of an appropriate slenderness ratio sr, which, for a structure with a rectangular cross section, depends only on the length L and height h of the structure:

$$sr = L\sqrt{\frac{A}{I_z}} = \frac{L}{h}\sqrt{12} \tag{5.2}$$

The third requirement was met by the use of an elastomer, which we will describe in detail in (5.2.2, p.47). Since the tracking target has a determined size, the length was chosen to be 190 mm to allow for good position tracking. With this length, we searched for a suitable height with the help of Fig.4.7 (p.33) and than, adjusted the width, such that a 2D-Bending mechanism was obtained. Therefore, it was decided to use a structure with the dimensions as shown in Tab.5.2 (p.46). Another challenging task was to connect the baseplate and the crossbeam, shown in

Length	190 mm
Height	70 mm
Width	123 mm

Table 5.2: Dimensions of the rectangular bending mechanism as shown in Fig.**??**b (p.**??**b)

.

Fig.5.3b,c (p.47) with the continuous structure. Since the used silicone is a highly hydrophobic material, adhesive bonding was not possible [87]. Therefore, we decided to make use of form closure and a primer medium to increase the adhesion. Our mechanical design was based on the principle of surface enlargement, which is why we designed anchor points and cavities included in the baseplate and the crossbeam. The elastomer was able to flow in and around those structures and achieve a high adhesion. The ends of the lever arms and the midpoint of the crossbeam contain bearing seats, where the tendons are mounted. As we modelled a clamped-free beam structure in (**??**, p.**??**), we needed to ensure the absence of any additional tip mas, to fulfil the boundary conditions. Therefore, we manufactured the crossbeam with the use of 3D-printing and a material filling ratio of 20%, to reduce weight. However, we needed to ensure stability and therefore, stiffening rips were included, see Fig.5.3b,c (p.47).

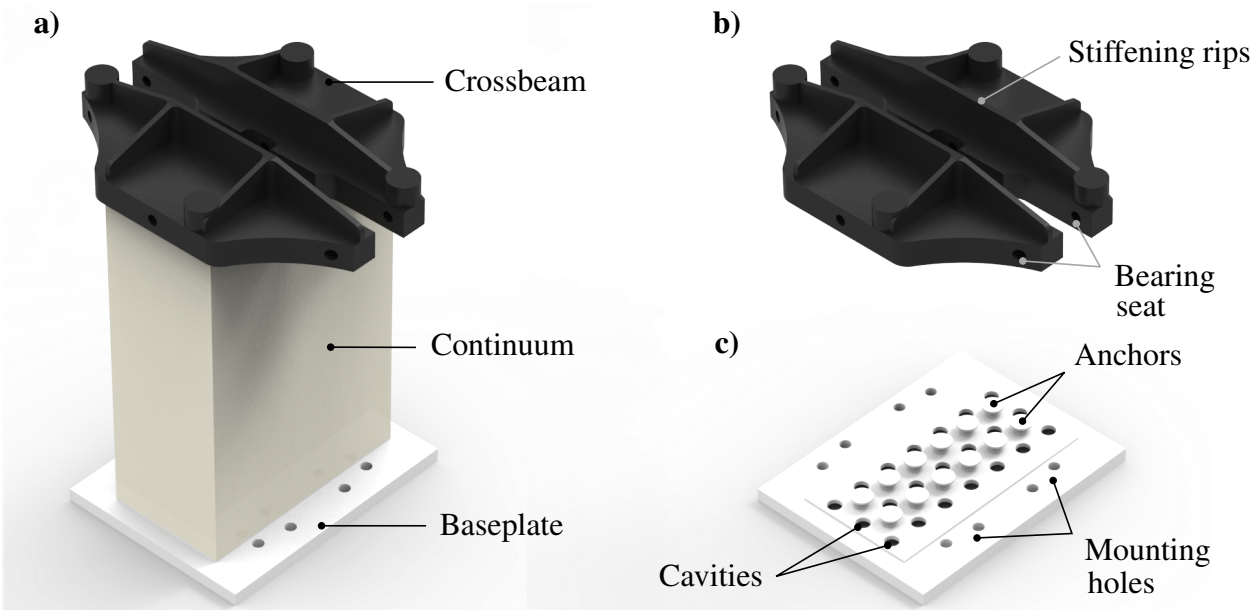

Figure 5.3: a) Design of the compliant mechanism with a baseplate, the continuous structure made of silicone and the crossbeam used for force transmission. b) The crossbeam includes bearing seats, where the tendons are mounted. To reduce weight, the material filling ratio is 20%. Therefore, we designed stiffening rips to ensure stability. c) To increase adhesion, the surface was enlarged by the use of anchors and cavities. This principle was used for both the baseplate and the crossbeam.

5.2.2 Manufacturing Process

Dragon Skin® was chosen as the manufacturing material, which is an addition-curing silicone with a shore hardness A30 and a 100 % Young's modulus of 600 000 MPa.
baseplate and crossbeam were mounted onto a mould, made of MDF plates. This mould was treated with a release agent wax, to ensure an easy removal of the compliant mechanism after the curing process. First, the two components of the silicone had to be mixed at a ratio of 1:1.

From this point on, there were 40 min manufacturing time remaining, before the silicone was cured. Within this time period, the air bubbles, trapped in the mixture, needed to be evacuated completely. After another four hours, the silicone was cured completely. Therefore, two crucial parameters of the manufacturing process have been the correct mixing ratio and the absence of air bubbles, trapped in the cured silicone.

5.3 Tendon Routing

Now, as the compliant mechanism was manufactured and mounted onto the testbed, the actuators had to be connected with the structure by the use of Dyneema® tendons. Following, the choice of tendon routing is described in detail, to give an overview on how it affects the force transmission. While the introduction of shear force was trivial to realize, the transmission of a bending moment was comparatively challenging.

Load type	Practical relevance	Example
Local moment	Actuation	Motor torques introduced at the tip
Local force	Interaction	Interaction with rod like laparoscopic instruments
Distributed force	Interaction	Lifting tissue or organs

Table 5.3: Three different load types, which can affect the structure. While a local moment is a reasonable load type for actuation, local forces and distributed loads may occur, when the structure interacts with it's surrounding.

In principle, there are three load types which can occur at every point over a structures length. For the minimally invasive surgery, those three load types have more or less practical relevance: A moment is most likely introduced at the tip for the purpose of actuation, while it is unprobable that tissue interaction produces a concentrated moment. Introduction of a local force may occur, whenever the structure interacts with it's surrounding. As well, distributed loads may be opposed to the structure whenever it interacts with tissue, for example when lifting organs.

5.3.1 Moment Actuation

To introduce the forces resulting in the actuation moment a crossbeam was mounted onto the structure's tip. This crossbeam provides a lever arm with length $l = 80\,\text{mm}$ at each side of the mechanism. Note that this length was gained from CAD-data and underlies the manufacturing accuracy of the 3D-Printer. To ensure the introduction of a tip moment only, the direction of the forces have to be perpendicular to the cross beam for each tip deflection v. As shown in Fig.5.4a (p.49) this is not always the case. For an increasing v, the points of intersection x_i travel down on

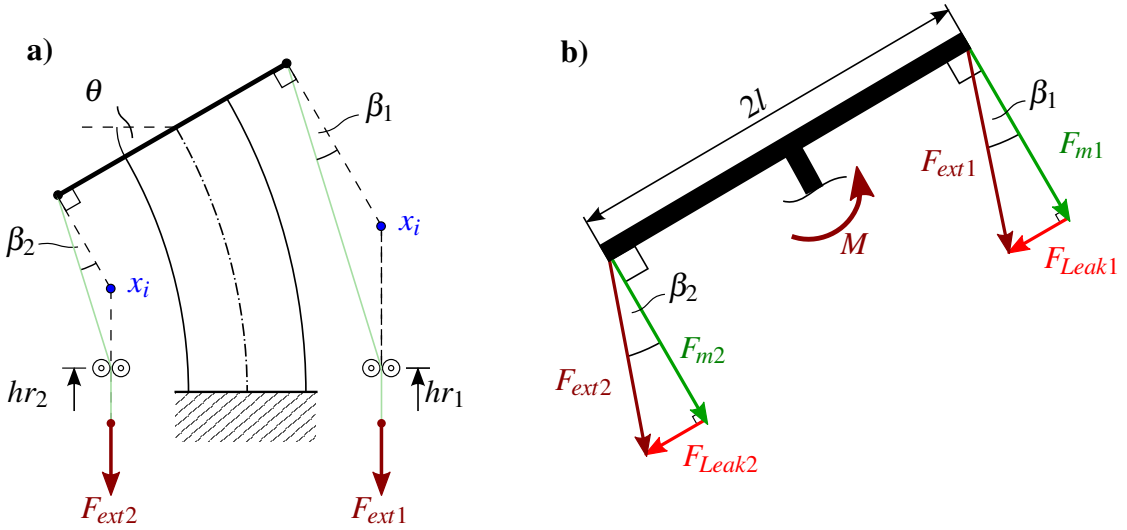

Figure 5.4: a) Because the pulley positions hr_1, hr_2 are fixed, two errors in the force transmission β_1, β_2 occur. b) Resulting force triangles. because $\beta_{1,2} \neq 0$ a leak Forces $F_{leak1,2}$ disturb the introduction of a tip moment only. These forces does not produce any moment, because they miss a lever arm.

the actuating side, while on the antagonistic side, they travel up along a vertical line in distance l to the structures mid fibre. Note that the positions of the pulleys are fixed and, therefore, they can not follow x_i. This results in the angular errors β_1 and β_2, which disturb the presence of a pure actuation moment. Fig.5.4b (p.49) shows the resulting force-triangles. Since $F_{leak1,2}$ miss a lever arm, they does not produce any moment and, therefore, the actuation moment composes as

$$M = l\cos\beta_2 \cdot F_{ext2} - l\cos\beta_1 \cdot F_{ext1}. \tag{5.3}$$

Therefore, the force transmission error (FTE) was introduced to give a quantity for the resulting leak force.

$$FTE_i(\theta) = \frac{F_{leak,i}}{F_{ext,i}} = \frac{F_{ext,i}\sin(\beta_i(\theta))}{F_{ext,i}} \tag{5.4}$$

Now, the next step was to identify the pulley positions $hr_{1,2}$ resulting in the lowest FTE within the workspace. For a fixed pulley position on the actuating side, there are a maximum of two tip positions v_{z0} and v_z within the workspace, where $\beta = 0$. This is the case for $v_{z0} = 0$ and

$$v_z = \tan(\theta_z)(x_z - l\cos(\theta_z) - hr_i) + l(1+\cos(\theta_z)), \tag{5.5}$$

where x_z is the axial position of the structures tip corresponding to v_z, θ_z is the tip plane angle at the second zero crossing and l is the length of the lever arm. Now, the pulley positions hr for the actuating side were computed using (5.5) in a way that the second zero crossing occurs at a tip deflection of $v_z = 10,\ 20,\ 30,\ 40,\ 50\,\text{mm}$. Following, for every $hr(v_z)$ the compliant

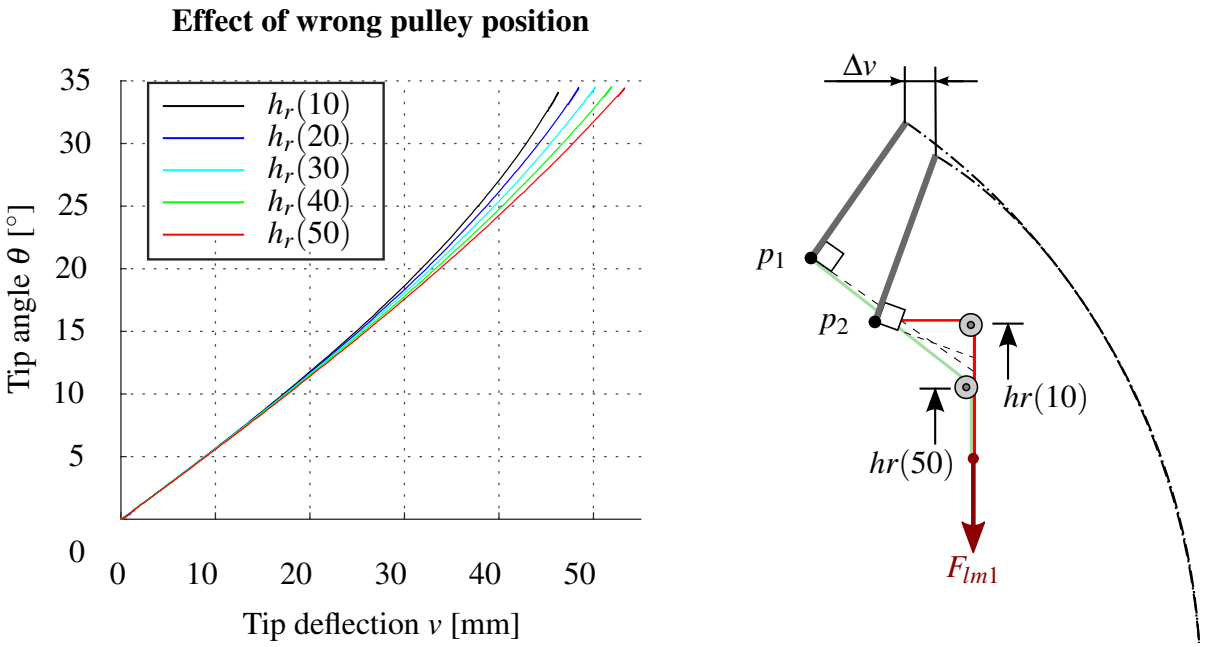

Figure 5.5: Wrong pulley positions result in an undefined load case. p_1 and p_2 are not able to travel to a lower vertical position than their pulleys. At the point, where they are the same, the tip deflection v stops, while θ increases.

mechanism was moved once through the workspace in our test bed. Fig.5.6 (p.51) shows the FTE for the actuating side. Note that for the first to pulley positions $hr(10)$ and $hr(20)$ the FTE stays almost 0 until θ_{z2} is reached and then, it rises rapidly. For $hr(30)$, the second zero crossing occurs at 15.5° and for $hr(40)$ it occurs at 26°. For $hr(50)$ it is never reached within the workspace. This seems plausible because for small deflections, F_{leak} acts in positive transverse direction and reduces β a little bit, which shifts the structure closer to the introduction of a tip moment only. Opposed to that for larger deflections, F_{leak} acts in normal direction and, therefore, increases β. At a certain point, this increase is that big that the point of a perfect moment will never be reached within the workspace. Another interesting finding is that for smaller hr, the tip defelction v decreases while the tip angle θ increases. Fig.5.5 (p.50) explains this phenomena: p_1 and p_2 will never be able to travel to a lower axial position than their corresponding pulley positions, because the tendon would then go slack. At this point, the bending is suppressed. For $hr(10)$, the point where $p_2 = hr(10)$ is reached earlier, because of the higher FTE. Then, F_{leak} pulls p_2 towards the midpoint of the beam and, therefore, increases θ, while the tip deflection v stays the same.

For $hr(50)$ the FTE never gets bigger than 3.5 %, which is why this pulley position was chosen to be suitable (Fig.5.6, p.51). As we aimed to move the compliant mechanism in a range of $\pm 35°$, it is clear that the pulley positions hr_1, hr_2 have to be equal, because within one cycle, every linear motor will once be the actuator and once the antagonist. Note that the FTE of the antagonist side was found to be considerably higher than the FTE for the actuating side.

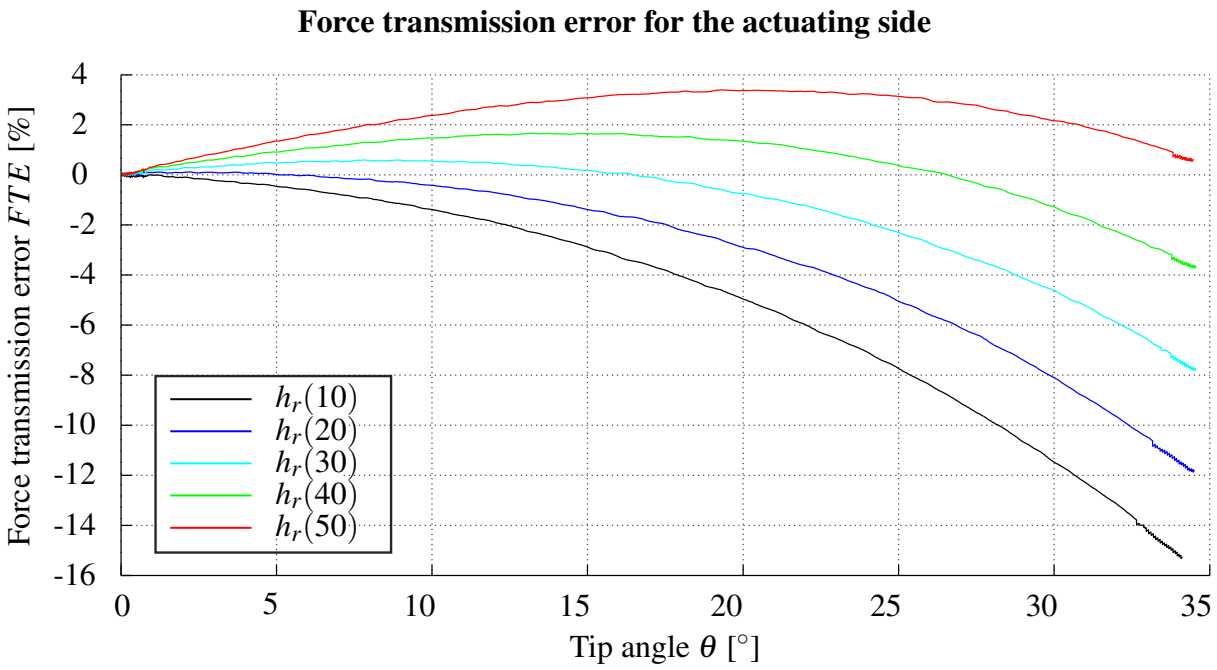

Figure 5.6: Force transmission error (FTE) for the actuating side. For the pulley position $h_r(50)$, the FTE never exceeds a value of 3.5 % within the workspace which is why this position was chosen to be suitable for the experiments.

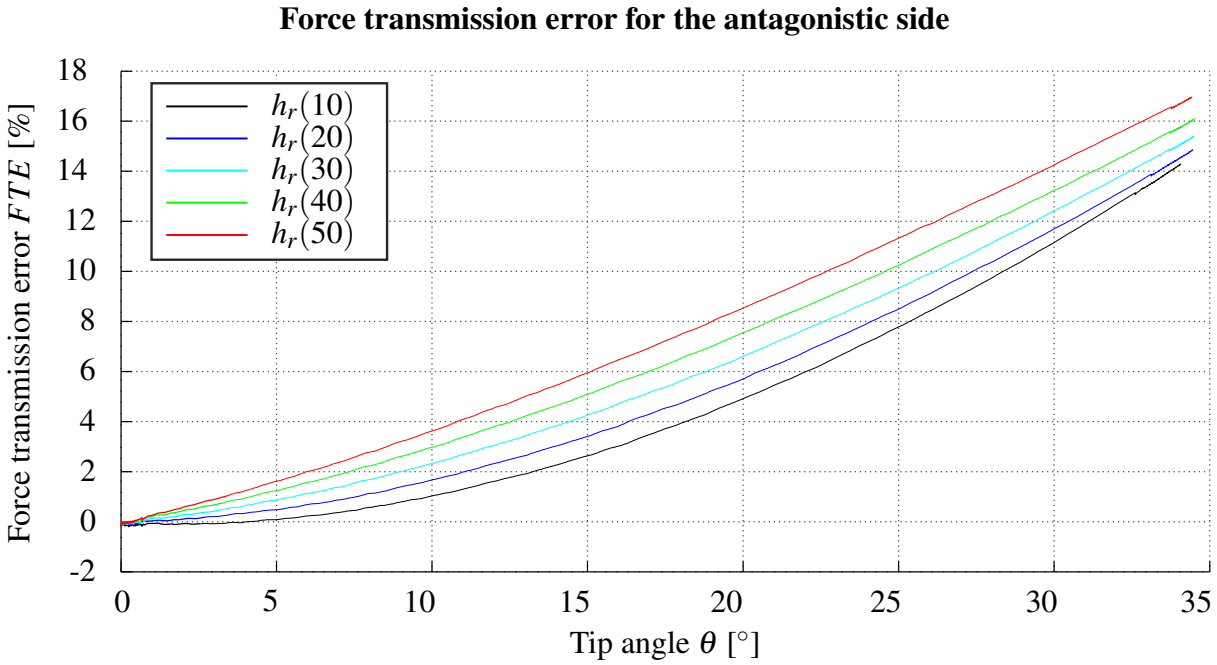

Figure 5.7: Force transmission error (FTE) for the antagonist side. While $h_r(50)$ is the best choice for the actuating side, for the antagonist side, it produces the highest FTE. For small pretensions, this is negligible, but should be considered, when applying higher pretensions to the compliant mechanism.

5.3.2 Shear Force Introduction

As explained in (4.6.2, p.31) for the introduction of a perfect moment, the static response for the Euler-Bernoulli and the Timoshenko theory is the same. Therefore, to measure the error resulting in the use of an inadequate theory, one has to introduce a shear force to the structures tip. Opposed to the actuation via a tip moment only, this is trivial. The actuating linear motor was placed 60 cm away from the structures midpoint. As the compliant mechanism will undergo an axial compression of maximum 13 mm, this placement results in a maximum error angle of $0,6^\circ$ between perfect and real force transmission, which is negligible.

5.4 Material Investigation and Parameter Estimation

Since the material parameters of polymers depend highly on the manufacturing process, the charge and the type of loading, measurements concerning the parameter identification needed to be performed. This includes the determination of elasticity, such as the Young's and shear modulus and investigations concerning the linearity of these parameters. The manufacturer's information about the Young's modulus was 600 000 MPa measured in an interval of $0 - 100\,\%$ strain. Since the compliant mechanism was moved in a range of $\pm 35^\circ$ for the tip angle which corresponds to a maximum of 12° outer fibre strain, it was assumed that this parameter will not be suitable to use for the simulations, because the strain ranges were not equal. Therefore, it was essential to find an adequate experiment based on standardised tests. To determine the Young's modulus and the Poisson's ratio ν, a modified compression test was conducted. Furthermore, standardised tensile- and 3-point bending tests were performed to verify the results of the modified compression test and investigate the dependency of velocity of the material properties.

5.4.1 Modified Compression Test

Fig.5.9a (p.53) shows the testing structure undergoing ordinary bending. Note that the outer fibre at the actuating side undergoes compression, while the outer fibre on the antagonist side experiences an elongation. Within an elastomer, the Young's modulus of compression matches the Young's Modulus of tension in a small interval of deformation [88, 89, 87]. For a larger compression, the elastomer fibres are crumpled up, see Fig.5.9c (p.53). Since the material can not disappear, the compression modulus is assumed to rise until a certain point. Opposed to that for an elongation, the elastomer fibres are pulled apart, see Fig.5.9d (p.53). At a certain point, the elastomer's binding sites will be destroyed and, therefore, the fibres are able to drift apart [89]. This may results in the fall of the Young's modulus for lager tensile strains.
From this view, one could assume a two spring analogy (Fig.5.9b, 53) for a bending mechanism, where the spring representing the compression modulus is likely to become stiffer than the one used for extension when undergoing higher bending. Based on this findings, it was decided

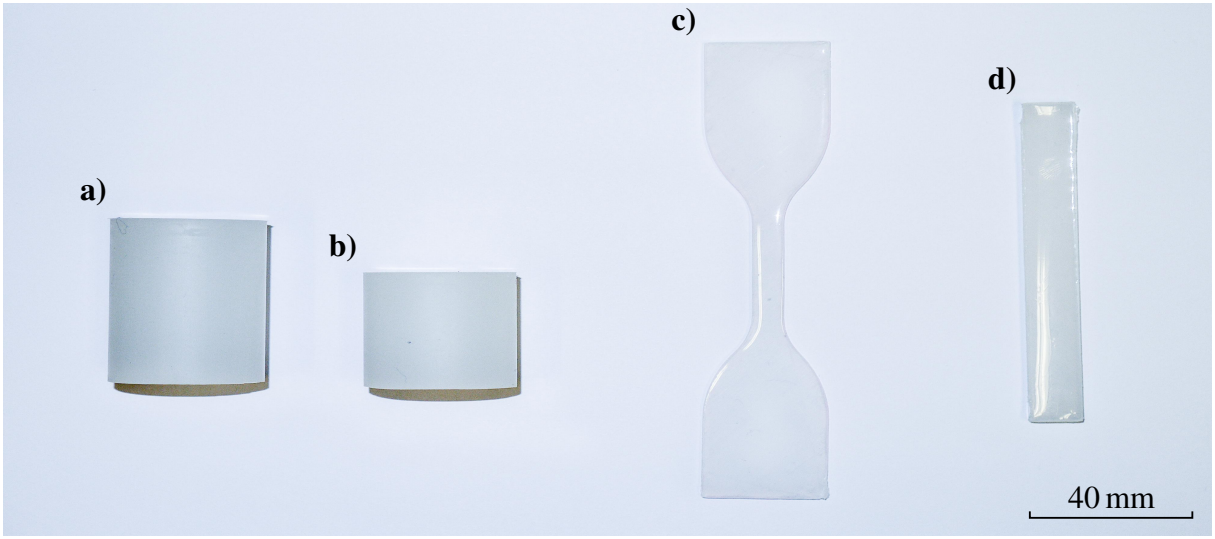

Figure 5.8: Different test objects: a,b) non-standardised test specimens for the compression test. c) Standardised shouldered test bar for tensile testing. d) Standardised test bar for 3-point-bending test.

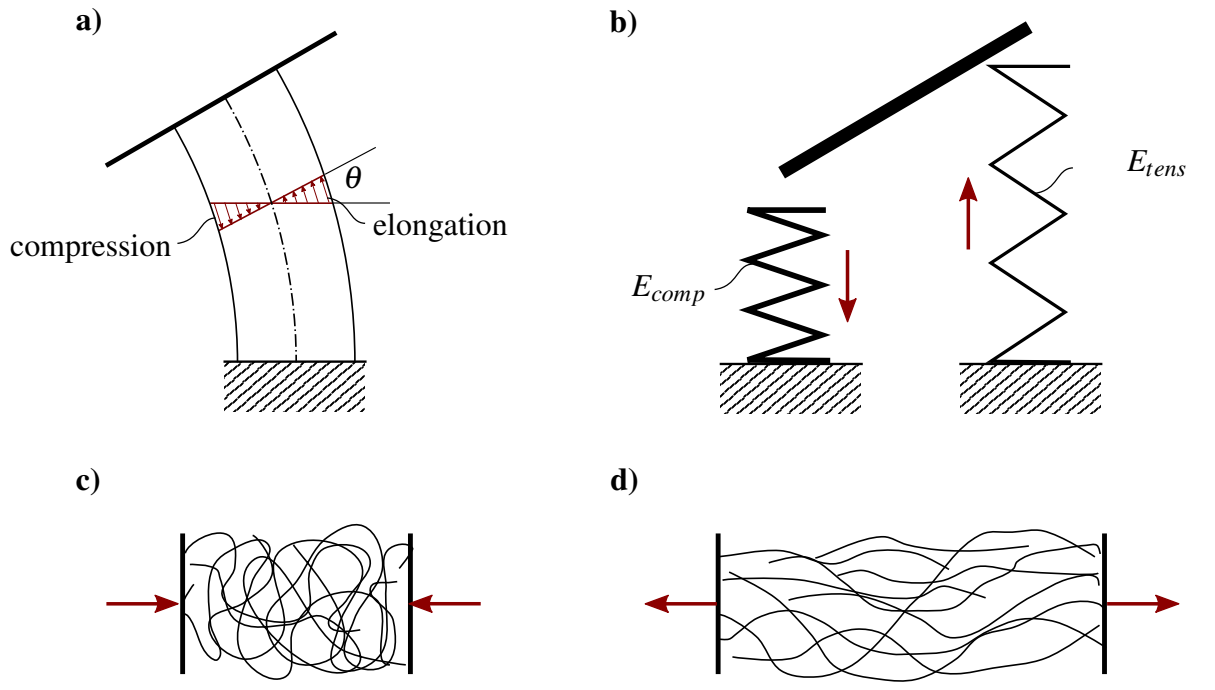

Figure 5.9: a) When bending a beam, one outer fibre undergoes compression, while the other experiences an extension. b) If the Young's modulus of compression differs from the Young's modulus of tension, one has to consider the compression modulus for the actuating side. c) Polymer fibres crumbling up while compression. d) Polymer fibres drifting apart while extension.

to perform a compression test in the interval of $0 - 12\,\%$ compression, which correlates the maximum outer fibre compression.
Within this modified test, two test probes with diameter $d = 29.5\,\text{mm}$ have been investigated. The first probe had a length of 28 mm, the second a length of 40 mm and were manufactured independently from the compliant mechanism. The tests were conducted using a Zwick tensile testing machine. The test specimens were concentrically arranged to the machine's axis and compressed within a range of 0 - 16 % of strain.To compute the Poisson's ratio ν the diameter at the mid point of the probe was measured using a dial gauge in steps of 2% strain. Fig.5.10 (p.54) and Tab.5.4 (p.54) show the testing results. The compression modulus of the two probes rises constantly within a range of 0 - 16 %. Note that the Poisson's ratio ν was measured to be a constant with mean values of 0.74 and 0.72.

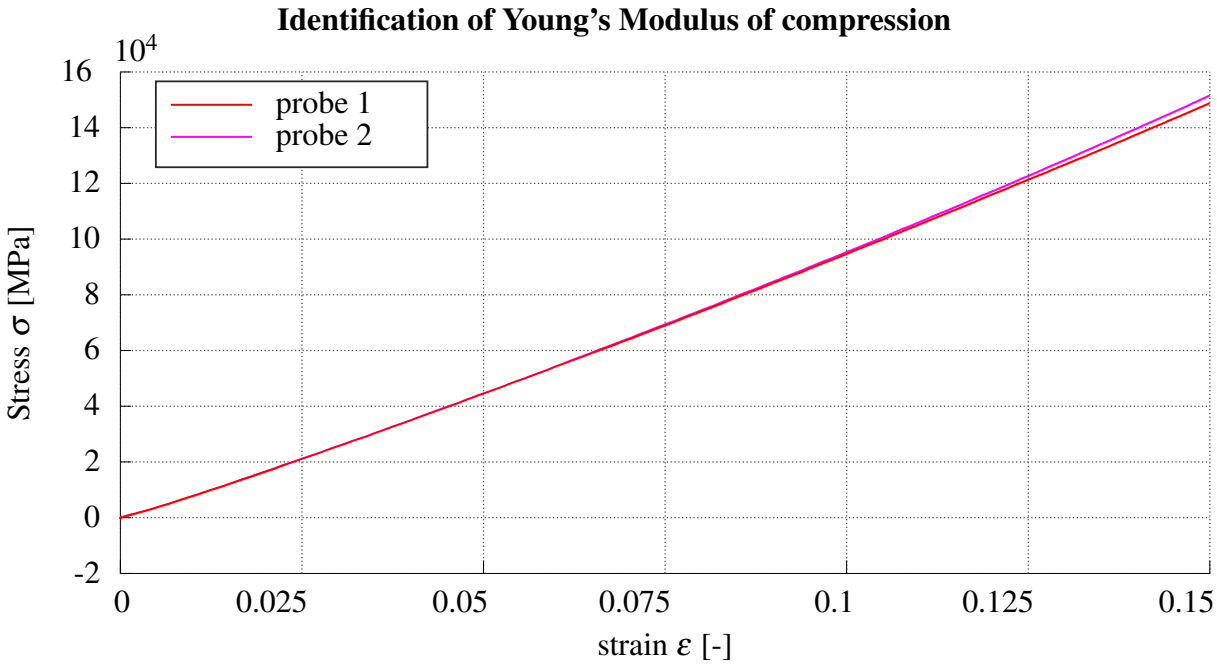

Figure 5.10: A compression test was performed with two cylindrical test probes, $L_1 = 28$, $L_2 = 40$. See tab:.5.4 (p.54) for results.

	Probe 1		**Probe 2**	
	E [Mpa]	ν [-]	E [Mpa]	ν [-]
4%	881 100	0.77	877 400	0.81
6%	911 060	0.71	908 700	0.66
10%	957 500	0.71	952 100	0.69
16%	1011 800	0.75	996 900	0.70
Mean	-	0.74	-	0.72

Table 5.4: Results from the modified compression test corresponding to Fig.5.10 (p.54).

5.4.2 Standardised Material Test

To verify the results gained from the modified compression test, standardised tensile and 3-point-bending tests were performed. The experiments were carried out on the same tensile testing, as the compression test. As test specimens, a shouldered test bar and a thin test rod were used, see Fig.5.8 (p.53). See Fig.5.11 (p.55) and Tab.Tab.5.5 (p.56) for the results of those test bending test. For $E_{4\%}$, $E_{6\%}$ standard deviation from tests performed with varying velocity is 2 % and 6 %. Therefore, it is assumed that within the range of 2 mm/s and 8 mm/s the material parameters do not underlie any dependency of velocity. Note that the 3-point-bending test could be erroneous, because the test bar was pre bent slightly because of gravity.

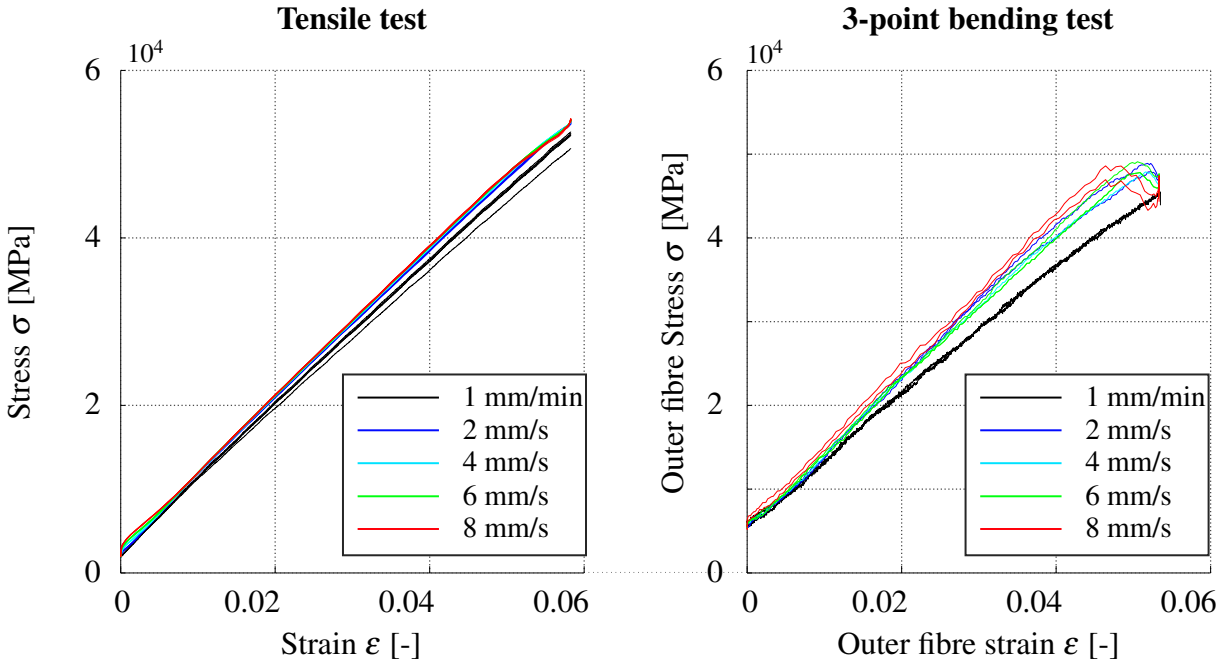

Figure 5.11: A tensile test and a 3-point-bending test were performed to support the results from the compression test and to investigate the dependency of velocity of the elastomer. Within the range of velocity, a dependency could not be confirmed. See Tab.5.5 (p.56) for results. Note that the 3-point-bending test could be erroneous, because the test bar was prebent slightly because of gravity.

	Tensile test		3-point-bending test	
	$E_{0,25\%}$ [MPa]	$E_{6\%}$ [MPa]	$E_{0,25\%}$ [MPa]	$E_{4\%}$ [MPa]
1mm/min	975 400	855 900	629 500	785 800
2mm/s	886 900	885 200	623 700	908 100
4mm/s	839 200	887 700	593 300	879 200
6mm/s	826 000	886 000	602 300	876 100
8mm/s	899 500	881 900	716 000	914 000
MEAN	885 400	879 300	633 000	872 600
STAW	0.07	0.02	0.08	0.06

Table 5.5: Results from tensile test and 3-point-bending test corresponding to Fig.5.11 (p.55).

6 Results

In the following chapter, the experimental results that were measured on the tested described in (5, p.43) during the course of the present work will be illustrated. First, we will give an evaluation of the testbed and the modelling approach after which we will present the results regarding the implementation of the position controller. At last, we will give a brief overview about the dynamical behaviour of the compliant mechanism.

6.1 Evaluation of Testbed and Modelling Approach

In this section, we will evaluate the testbed and the modelling approache, namely the CC approximation and the Timoshenko theory. Within the experiments, we have encountered a range of difficulties which reach from the directionality of the Testbed to material non-linearitys. In detail, these difficulties are:

1.	Force transmission	Influences of testbed
2.	Directionality of the tesbed	
3.	Influence of mean deformation rate	Influences of material properties
4.	Identification of the compliant mechanism's elastic behaviour	
5.	Model errors for moment actuation	Influences of modelling approach
6.	Influence of pretension	
7.	Model errors for shear actuation	

First, we will deal with the influences resulting from the testbed design. Then, the material properties of the compliant mechanism will be investigated. Afterwards we will evaluate the accuracy of the modelling approach for different load cases. The structure of each of following paragraphs will be divided into four sections: intention, experimental design, results and discussion. Note that there is no chronological order. In some cases we will anticipate results, which will be referenced accordingly.

We defined the workspace the workspace of the compliant mechanism to be $\pm 35°$. Following we will only regard the measured quantities at the compliant mechanism's tip, such that e.g. $v(L)$, $\theta(L)$ and $x(L)$ will be called v, θ and x.

6.1.1 Force Transmission

Intention: As explained in (5.3.1, 48), the vertical pulley position has a strong influence on the force transmission. Wrong positioned pulleys increase the error angle β between the vectors of perpendicular and actual force introduction. Remember, that the constant curvature assumption only possess validity for tip moment only introduction without any disturbances. Therefore, we needed to ensure, that the actuation forces act in a purely perpendicular direction on the lever of the crossbeam.

Experimental Design: The pulleys have been placed to the best of our knowledge. For the vertical placement, we measured height from equal references. From these references, the pulleys on the right were placed at a height $hr_1 = 64.5$ mm and the pulleys on the left at $hr_2 = 64.7$ mm. For the horizontal placement, a distance of 45.5 mm to the outer fibre of the compliant mechanism was ensured. The compliant mechanism was moved ones through the workspace at a mean deformation rate of 5 mm/s and a pretension of 10 N. We assumed that there will be no influence of mean deformation rate on the material parameters. Measured quantities were the tip-position and tip angle from which the error angle for the actuating side β and for the antagonistic side β_A were computed.

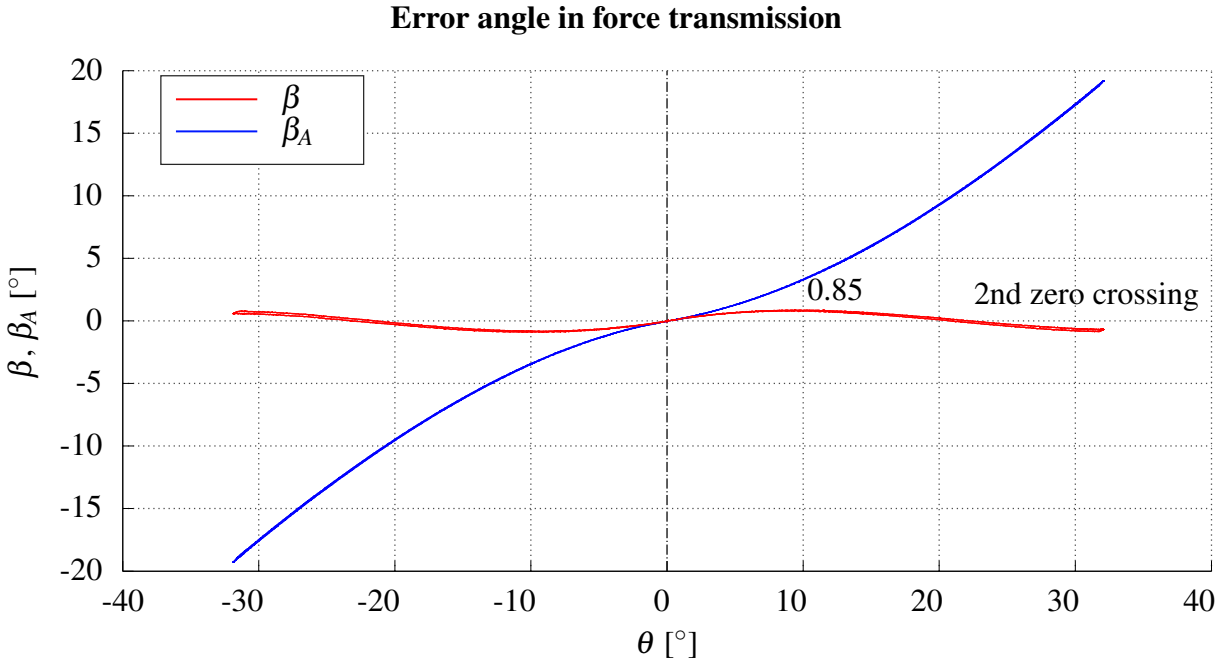

Figure 6.1: Error angels between real and perfect force transmission of the actuating side β and of the antagonistic side β_A for the chosen pulley positions. β never raises over a value of $0.87°$, which is why we were able to assume perfect force introduction at the actuating side. β_A rises constantly to a much higher value of about $19°$. This fact has to be taken into account, when dealing with higher pretensions.

Results: Fig.6.1, (p.58) shows the error angles β and β_A. As predicted in (5.3.1, p48), the course of β starts at 0 and rises to a maximum of 0.87° after which a second zero crossing occurs. At this point, the actual force acts again in a perpendicular way on the lever arm. Confirming all predictions from (5.3.1, β_A rises constantly until the maximum of 19° at the boundaries of the workspace. Note that the curves are point symmetrical.

Discussion: Since $\cos(\beta_{max}) \sim 1$, we were able to assume a perfect force transmission for the actuating side. On the antagonistic side, the influence of the increased error angle $\beta_{antagonist}$ is only negligible, when dealing with low pretensions. The maximum leak force at the antagonistic side was found to be $F_{leak,max} = \sin(19°)F_{pre} = 0.326F_{pre}$. Based on this findings we decided to assume constant curvature only for pretensions until $F_{pre} = 10\,\text{N}$.

6.1.2 Testbed Directionality

Intention: The testbed was designed to allow a reachable workspace of ±30° maximum tip angle and, therefore, we needed to investigate the directionality before performing any measurements. As the movement went from one side to another we assumed, that we will encounter some degree of deviations in the tip pose at the reversing points of each side. As well, the influence of initial displacement on the directionality of the testbed was of interest.

Experimental Design: To measure the directionality of the testbed, the maximum values of v, θ, x, F_{ext1} and F_{ext2} at the reversing points were measured for positive and negative deflection while moving the compliant mechanism once trough the workspace. The motion was conducted at a mean deformation rate of 5 mm/s and a pretension per tendon of 10 N. Again we assumed that there will be no influence of mean deformation rate on the material parameters. This procedure was repeated for different initial angles θ_{init} represented through a difference of initial tendon forces $\Delta F_{init} = F_{ext1} - F_{ext2}$. This is because we assumed, that for equal initial forces, the compliant mechanism needed to be in a upright position, just like the principle of a seesaw. The initial displacement was varied in a range of$\pm 2N$ steps of in 1 N for ΔF_{init} by manually applying an initial deflection to the mechanism until the desired difference in forces was recorded.

Results: First, it may be well to mention, that a relatively small change in the initial deflection resulted in a significant amplification of the directionality. We recorded initial angles in a small range of -0.4 to 0.7°. Fig.6.2 (p.61) shows the directionality for the measured quantity. Two phenomena have to be explained, at first the presence of a intrinsic directionality, see Fig.6.2a,b,c. For the absence of a initial displacement ($\Delta F_{init} = 0$), those quantities experienced an offset, while the maximum forces at the reversing points could be considered equal. These offsets were $\Delta v = 0.5\,\text{mm}$, $\Delta\theta = 0.1°$ and $\Delta x = -0.5\,\text{mm}$, respectively. Secondly, for a initial displacement, the maximum values of every measured quantity drifted apart. The resulting errors increased with a larger displacement. While the error for v and θ have been within 0 % to 2.5 %, the

ΔF_{init}	[N]	-2	-1	0	1	2
$v_{max,+}$	[mm]	47.7	47.7	48.0	48.1	48.3
$v_{max,-}$	[mm]	-47.8	-47.9	-47.5	-47.4	-47.1
Δv	[mm]	-0.1	-0.2	0.5	0.7	1.2
P_{error}	[%]	0.2	0.4	1.0	1.5	2.5
$\theta_{max,+}$	[°]	30.8	30.7	30.8	30.9	31.0
$\theta_{max,-}$	[°]	-30.8	-30.9	-30.7	-30.7	-30.6
$\Delta\theta$	[°]	0.0	-0.2	0.1	0.2	0.4
P_{error}	[%]	0.0	0.6	0.3	0.6	1.3
$x_{max,+}$	[mm]	10.1	10.0	10.3	10.3	10.5
$x_{max,-}$	[mm]	10.9	10.9	10.8	10.6	10.5
Δx	[mm]	-0.8	-0.9	-0.5	-0.3	0.0
P_{error}	[%]	7.3	8.3	4.6	2.8	0.0
$F_{max,ext2}$	[N]	-137.2	-136.5	-135.4	-134.1	-133.2
$F_{max,ext1}$	[N]	-132.4	-133.1	-134.7	-136.0	-137.2
ΔF	[N]	-4.8	-3.4	-0.7	1.9	4.0
P_{error}	[%]	3.5	2.5	0.5	1.4	2.9

Table 6.1: Results of the directionality test corresponding to Fig.6.2 (p.61).

maximum divergence of x was about 8 %.

Discussion: The results showed, that the used testbed underlies an intrinsic directionality, which could be due to inaccuracies in manufacturing process, wrong pulley position, friction or a mixture of those errors. We assumed, that the intrinsic directionality asserts itself as an initial offset between $|v|$, $|\theta|$, and $|x|$ (maximum values of the green lines should be the same, see Fig.6.2d). As well, we encountered a directionality triggered by the initial deflection, which showed itself in a growing divergence of the maximum values. When performing measurements, these facts were kept in mind. For further measurements neutral position was chosen to be at $\Delta F_{init} = 0\,\mathrm{N}$ and was ensured by adjusting the compliant mechanism manually. Because of the directionality, in some of the following experiments and as well for the position controller, we will only evaluate the positive bending direction.

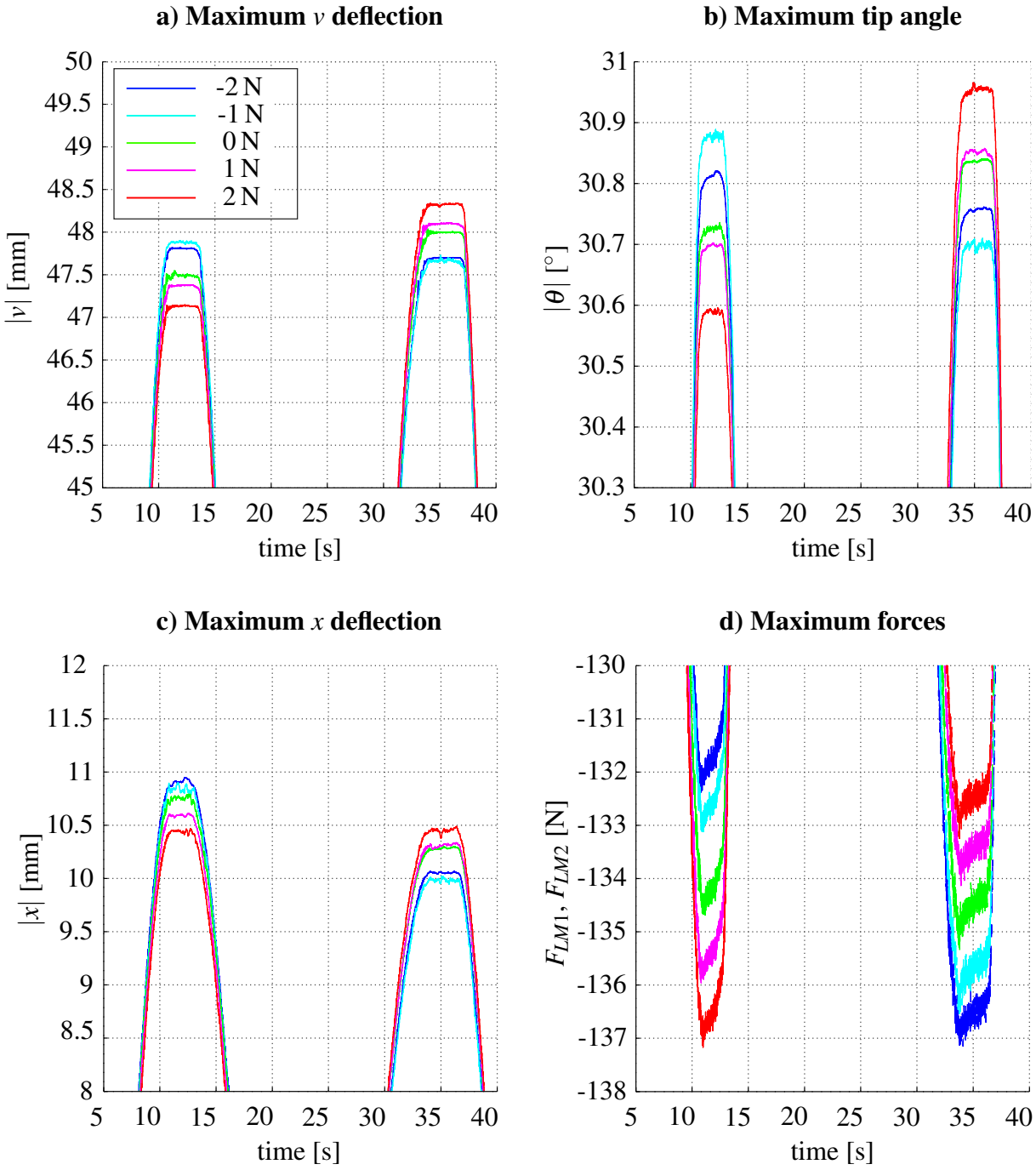

Figure 6.2: Directionality of the measured quantities v, θ, x at the structures tip and F_{ext1}, F_{ext2} in the reversing points of each side. a) Maximum tip deflection $|v|$. b) Maximum tip angle θ. c) Maximum axial deflection x. d) Forces in external load cells F_{ext1}, F_{ext2}. Note that the intrinsic directionality asserts itself as an initial offset between $|v|$, $|\theta|$, and $|x|$ (as seen in d), maximum values of the green lines should be the same). The directionality triggered by the an initial deflection asserts itself in a growing divergence of the maximum values.

6.1.3 Influence of Mean Deformation Rate

Intention: In the experiments described above, we assumed, that the mean deformation rate has no influence on the results. To ensure, that this assumption is valid, we needed to investigate the effect of mean deformation rate.

Experimental Design: We moved the compliant mechanism once through workspace with different mean deformation rates at a pretension of 10 N per tendon and measured the tip position $\boldsymbol{p} = [xv]^T \in \mathbb{R}^2$. The conducted mean deformation rates were 5, 10, 20, 30, 40 mm/s, respectively.

Results and Discussion: Fig.6.3 (p.62) shows the results. Note that the curves match each other. Objectively, we considered a mean deformation rate of 40 mm/s as fast motion. As we could not measure any differences between the curves, we assumed that the mean deformation rate has no influence of the behaviour of the compliant mechanism. Therefore, the assumption made above hold.

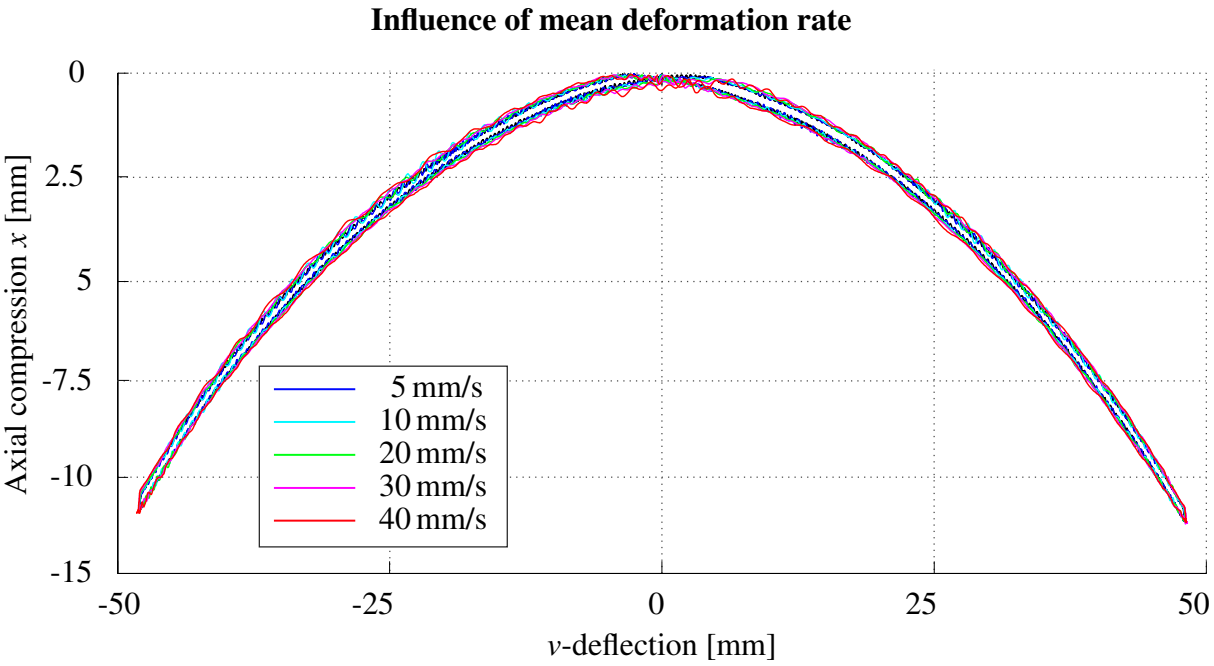

Figure 6.3: Influence of mean deformation rate. Note that there was no significant difference between the mean deformation rates was measured. Therefore, we assumed that the mean deformation rate has no influence of the behaviour of the compliant mechanism.

6.1.4 Young's modulus of the Compliant Mechanism

Intention: It was assumed, that the elastic properties of the material vary with the deformation and the spatially position $\in \mathbb{R}^3$ on the beam and, therefore, can be described as:

$$E = E(\varepsilon, \boldsymbol{r}). \tag{6.1}$$

The dependency of deformation was assumed, because elastomer tend to show a non-linear material behaviour [88, 89, 87]. Since it is not guaranteed that there are no structural anisotropies within the continuum, a spatial dependency of the coordinate $\boldsymbol{r}$ was introduced. Such structural anisotropies e.g. could be trapped air bubbles.
Since the outer fibre on the actuating side will be compressed while bending, the Young's modulus of compression was assumed to be the dominating material parameter, see (**??**, p.**??**). Therefore, we aimed to investigate, if the elastic properties of the compliant mechanism follow the Young's modulus of compression.

Experimental Design: The outer fibre stress and strain of the compliant mechanism within a movement can be obtained using:

$$\sigma_{max} = \frac{M}{I}\frac{h}{2} \quad [68], \qquad \varepsilon_{max} = \frac{h}{2}\frac{\theta}{L}, \tag{6.2}$$

where h is the height of the beam. The second equation of (6.2) was obtained from the CC assumption described in (4.7, p.32). As discussed above, F_{pre} opposed by the antagonistic actuator disturbs actuation moment by causing an additional leak force. Therefore, the antagonist was dismounted from the crossbeam. The compliant mechanism was moved ones from 0° to 35° at a mean deformation rate of 2 mm/s to correspond with the deformation rate used in the compression test.

Results Fig.6.4a (p.64) shows the stress-strain diagram of the used material gained from a compression test, which is covered by the measurement curve of the compliant mechanism. Fig.6.4b (p.64) shows the non-linearity of the Young's modulus as a function of the tip angle θ. Note that a significant non-linearity was observed, which increases the Young's modulus by 10 % by the end of the workspace.

Discussion The results showed, that the Young's modulus of compression can give an indication about the material behaviour of bending mechanisms. In our case two test specimens of different length, manufactured independently, led to similar measurement curves, which is why we assume scalability of the material parameter. The elastic behaviour of the compliant mechanism covers those curves in a range of 0-12 % of outer fibre strain. Therefore, we assumed, that the macroscopic Young's modulus is independent from the place in the continuum, such that

$$E = E(\varepsilon). \tag{6.3}$$

This might only be the case, if the manufacturing process is carried out appropriately and to the best of the manufacturers knowledge. Based on this findings, the fitted dataset for the Young's modulus was used for the following experiments.

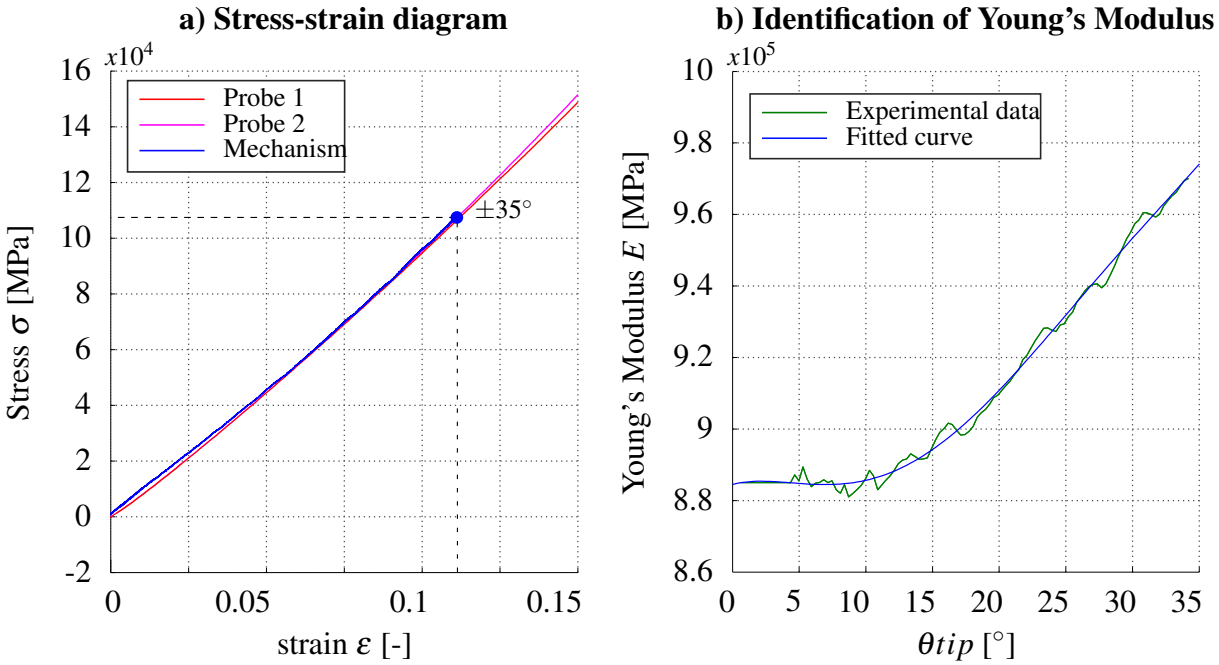

Figure 6.4: a) Stress-strain Diagram of the compression test, see (?? p.52). The elastic behaviour of the compliant mechanism matches the Young's modulus of compression. b) Experimental data and fitted curve for the Young's modulus with respect of the tip angle. This fitted dataset was used for the experiments concerning the accuracy of the modelling approach.

6.1.5 Model Errors for Moment Actuation

Intention: In this experiment, we aimed to evaluate the accuracy of our kinematic model, established in (4.7, p.32) within the present testbed. We assumed that there are two different errors: the error resulting from the force transmission via pulleys and an approximation error made by the use of the CC assumption.

Experimental Design: In this experiment, quantity of interest was the overall actuation moment M computed by the use of F_{ext1} and F_{ext2} with (5.3). Using the beam equations and the assumption of CC, we were able to derive the curvature k and the tip angle θ:

$$k = \frac{M}{EI}, \qquad \theta = \frac{ML}{EI}. \tag{6.4}$$

With this quantities, the tip position $\boldsymbol{p}_{CC} = [v_{CC}, x_{CC}]^T$ was computed and compared to the measured tip position and angle derived from the 3D-tracking system. From now on we were able to compute the errors in tip position and angle with

$$e_v = \frac{v_{CC} - v}{v_{max,cam}}, \quad e_x = \frac{x_{CC} - x}{x_{max,cam}}, \quad e_\theta = \frac{\theta_{CC} - \theta}{\theta_{max,cam}}. \tag{6.5}$$

As we have done before, the compliant mechanism was moved once trough the workspace with a pretension of 10 N and a mean deformation rate of 5 mm/s. Regarding the results of (6.1.2, p.59), we decided to evaluate bending in positive direction only.

Results: Fig.6.5 (p.65) shows the measured trajectory and the one predicted by the CC assumption. In the reversing point, the compliant mechanism bended in v-direction about 4% less than predicted by the CC assumption. Opposed to this, the x compression exceeded the predictions by a maximum of about 18%. The error in θ reached its maximum of about 2% at a tip angle of 16°.

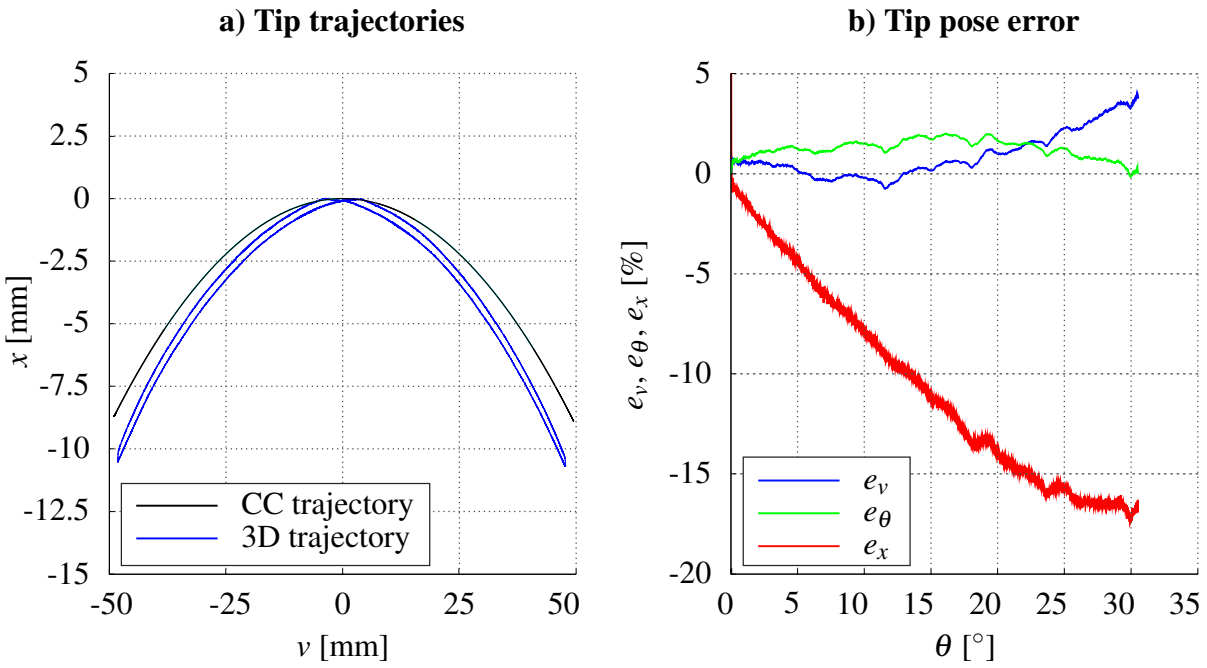

Figure 6.5: Model errors resulting from the use of CC approximation and the influence of a undefined leak force not incorporated in the modelling approach. While the tip angle θ never exceeds an error of 2% the maximum error of v and x were 4 and 18%, respectively.

Discussion: As we have seen in (6.1.1, p.58) the error angle β for the actuating side was comparatively small. It reached its maximum at a tip angle of about 10°. Compatible with this, e_θ showed the same course. θ_{CC} was computed according to the static Timoshenko beam theory by the use of the actuation moment M only. Note that e_θ never exceeded an error of 2%. Therefore, we concluded, that we can make a clear prediction about θ based on our modelling approach. For the tip position $\boldsymbol{p}$ we measured higher errors. Whereas the maximum of e_v was about 4%, e_x reached a maximum of about 12%. We assumed that the reason for these errors may be a mixture between the approximation error resulting from the use of the CC assumption and the error resulting from a leak force not incorporated in the modelling approach.

6.1.6 Influence of Pretension

Intention: When opposing pretension to the compliant mechanism, this may give rise to a number of effects, not covered by the modelling approach taken within this work. Some of this effects were found to be:

1. Initial axial compression of the beam.
2. Increased material non-linearity.
3. Disturbance of the constant curvature assumption

Usually the flexural stiffness EA of a beam structure is a lot higher than it's flexural rigidity EI and particular in our case $EA = 2500EI$. Therefore, we assumed, that for low pretensions, the initial axial compression is negligible. For higher pretension though, an influence on the beam length could be the case. If so, it must be assumed, that this initial strain will also result in an increased material non-linearity. Furthermore, higher pretensions disturb the introduction of the actuation moment. As mentioned above, the force introduction on the antagonistic side experiences a higher error angle β_A and, therefore, gives rise to a leak force. This force obviously increases with a higher pretension.

Experimental Design: The experimental design divides into two parts. At first, the influence of pretension on the initial compression and, therefore, on the initial length of the bending mechanism was investigated. The compliant mechanism was investigated in its neutral position, see above, and than the desired pretension F_D in the tendons was increased until a value of 60 N per tendon. Measured quantities were the forces in the external load cells F_{ext1}, F_{ext2} and the tip position v and x. Therefore, we were able to make a statement about the progress of the force at the tendon's starting points F_{ext1}, F_{ext2}. As we also measured the axial compression x, we were able to estimate the force in each tendon's end point with:

$$F_{out} = \frac{E(\varepsilon_x)A}{L_0}\frac{x}{2} \tag{6.6}$$

Note that this assumption is only valid when we assume the loss of force only happens in the tendon paths which includes tendon and pulley friction as well as tendon elasticity. Therefore, the experiment was conducted twice at different mean deformation rates, namely 0.2 N/s and 5 N/s. We assumed, that if there is any short time viscoelasticity in the compliant mechanism's continuum, we will derive different measurement curves for $F_{ext1,2}$ and x.
In the second part of the experiment, we aimed to investigate the influence of pretension on the overall actuation moment and the tip position and angle. The experimental design basically matches the ones used in previous experiments: the compliant mechanism was moved once

through the workspace while opposed to different pretensions in a range form 10 N to 50 N per tendon. Again, the initial v-displacement was adjusted as explained in (6.1.2, p.59). The experiment was conducted at 5 mm/s deformation rate. Measured quantities were the tip position consisting of v and x as well as the forces in the external load cells. Form these quantities, the overall actuation moment M for every pretension was computed using (5.3). As well with (6.5, the errors between tracked tip pose and CC approximation were computed.

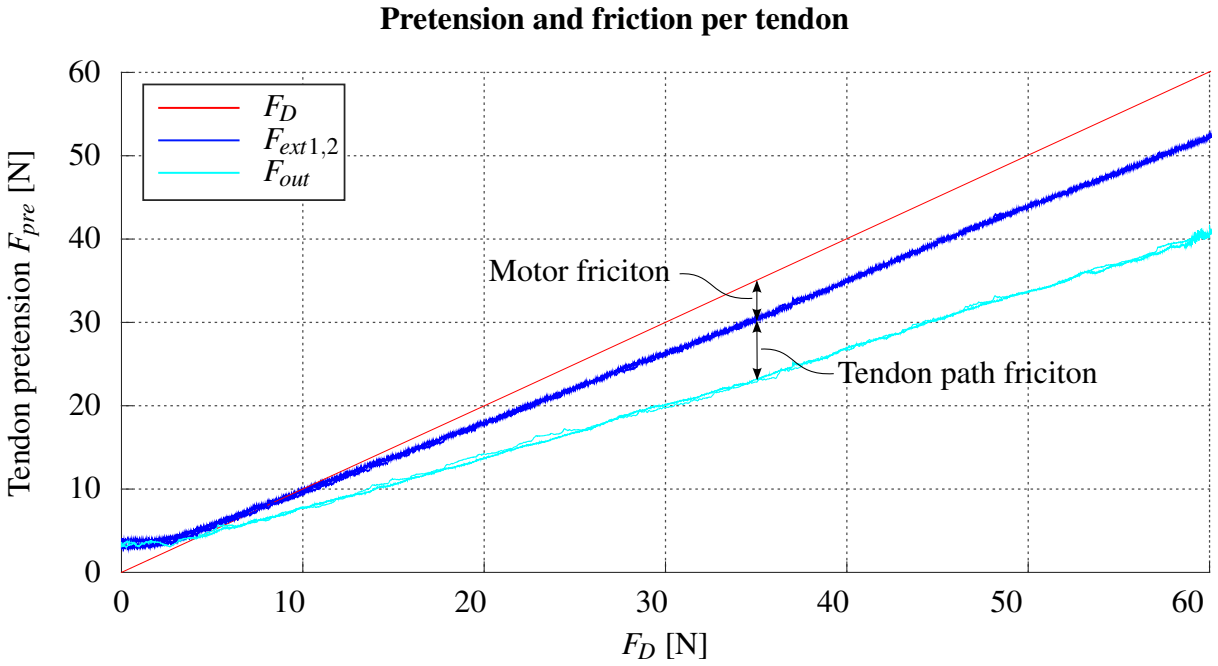

Figure 6.6: Pretension and friction in the tendons: the motor friction turned out as the difference between between F_D and $F_{ext1,2}$. The difference between $F_{ext1,2}$ and F_{out} could be considered as the loss of force in the tendons due to friction and tendon elasticity.

Results: Fig.6.6 (p.67) shows the progress of the forces, where F_D was the manipulated variable, F_{pre} the measured tendon force in the load cells $F_{ext1,2}$ and F_{out} the estimated force acting on the mechanism, computed with (6.6) under the assumption, that all friction and loss of force happens in the tendon path. Note that the curves for $F_{ext1,2}$ cover each other. While we lost about 2.25 N at $F_D = 10$ N in this experiment, at $F_D = 60$ N the loss increased to about 10 N per tendon. Fig.6.7a (p.68) shows the Force-Strain curves for different mean force rates which differ by the factor of 25. Note that they cover each other. A pretension of 60 N per tendon compressed the compliant mechanism about 1% of its initial length. This initial strain resulted in changed start points on the curve for the Young's modulus, see Fig.6.7b (p.68).

In the experiment concerning the model accuracy for higher pretension, the actuation moment was not found to differ with increased pretension, see Fig.6.8b (p.68). Opposed to that, the error in v-deflection e_v increased until a maximum value of 10%, while the error in axial compression e_x decreased until a maximum of 12%.

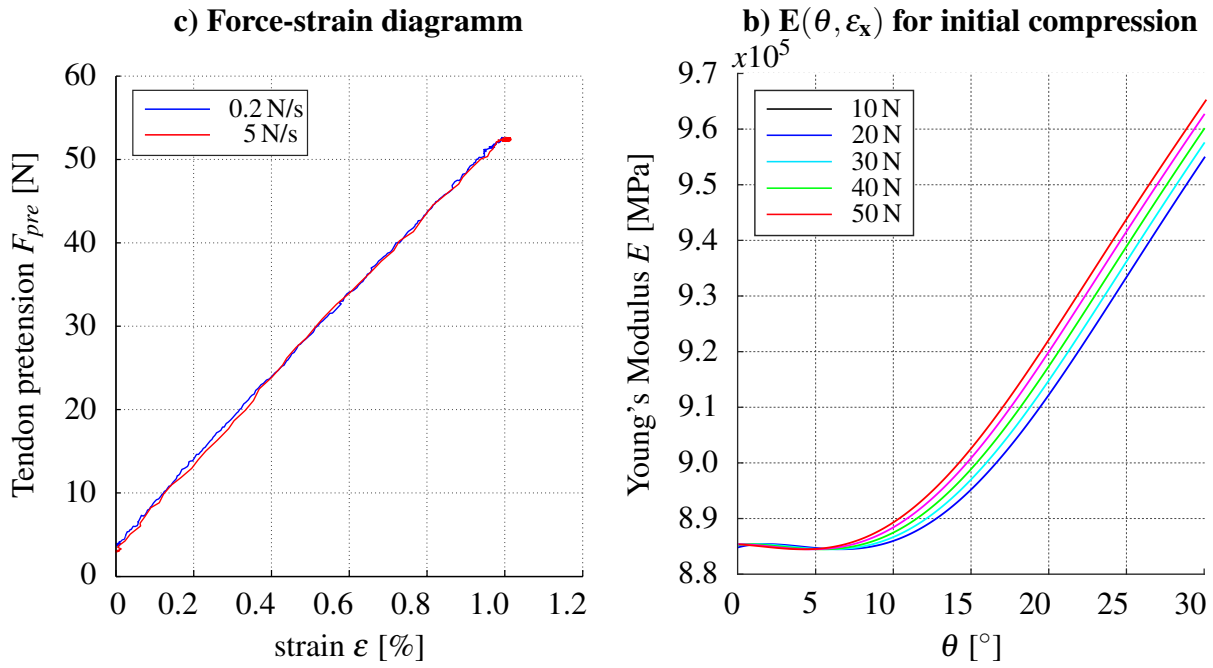

Figure 6.7: a) Force-strain curve for increasing pretension. The mean deformation rates differ by factor 25. b) Because the initial strain is increased with higher pretension, the curve of the Young's modulus shifts. Therefore, the initial compression has to be taken into account.

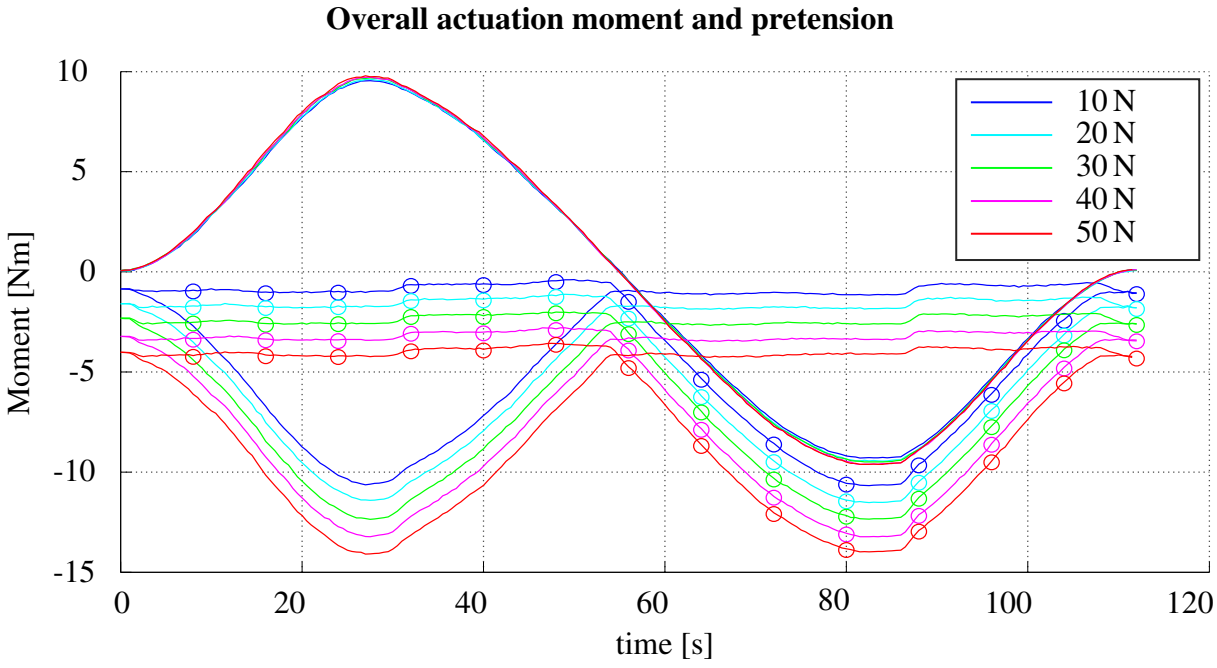

Figure 6.8: Overall actuation moment for higher pretension: since M is computed by a difference between F_{ext1} and F_{ext2}, it does not change with higher pretension.

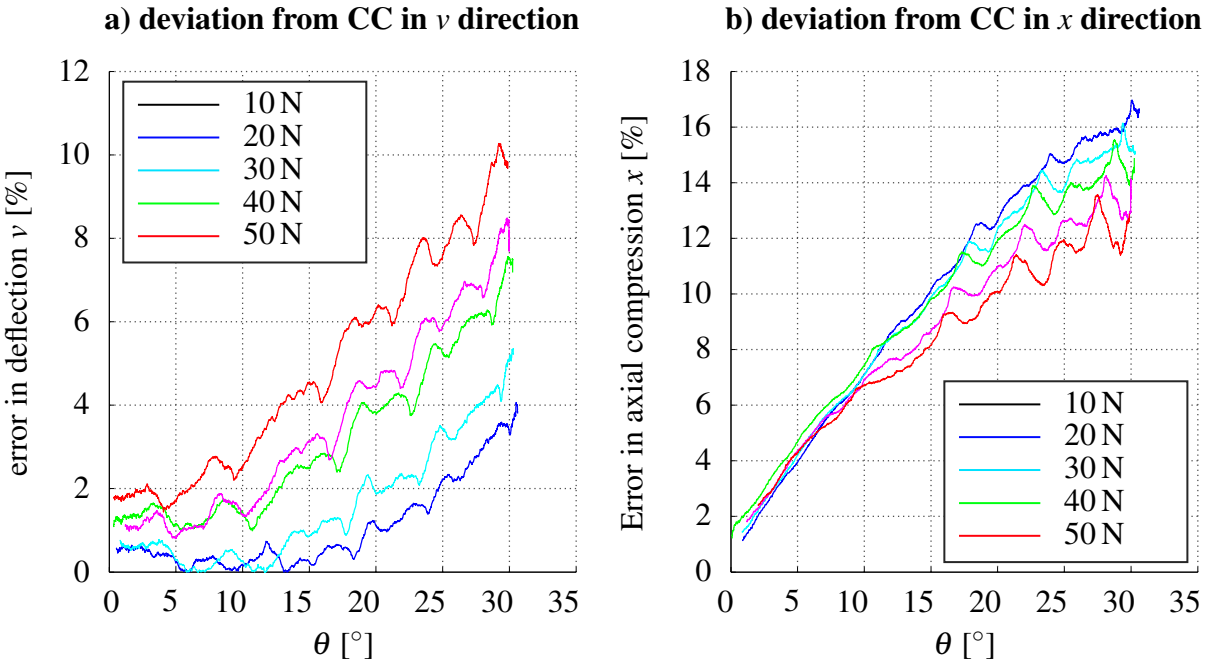

Figure 6.9: Although the actuation moment is the same for every pretension, e_v is increased while e_x is decreased for higher pretension. An explanation could be the presence of different load case due to β_A.

Discussion: The results showed a strong influence of pretension on both friction and Young's modulus. As described above, we assumed that all loss of force happens in the tendon paths. A criteria for this assumption to hold was the absence of any short time viscoelaticity within the continuum of the compliant mechanism. Fig.6.7 (p.68) shows two measurement curves for mean deformation rates which differ by the factor 25. As these curves match each other, we considered this as proof for the absence of short time viscoelasticity within the elastomer. Therefore, we where able to identify the loss of force within the tendon paths which was about 2.25 N at $F_D = 10\,\text{N}$. This finding matches the prediction of REINECKE *et al.*, who analysed the friction in steel and Dyneema® tendons [86].

The use of a higher pretension resulted in a shift of the Young's modulus, because the starting point on the characteristic curve shifts to higher strains. For a pretension of 10 N per tendon we derived a maximum Young's modulus of 955 000 MPa by the end of the workspace, while for a pretension of 50 N per tendon it raised to a value of 965 000 MPa. This is a increase of about 1%. Higher pretension had no effect on the overall actuation moment M. this is plausible, because M is computed using (5.3), which represents a difference between F_{ext1} and F_{ext2}. Regarding this fact, the errors in tip position and angle e_v, e_x and e_θ should be equal for any pretension. This is obviously not the fact. The only explanation for this could be the presence of an load case not incorporated in the Timoshenko beam theory.

6.1.7 Model Error for Shear Actuation

Intension: The aim of the present work had been also to investigate the load case of a tip shear force only. Therefore, we designed an experimental setup which allowed us to evaluate:

1. The feasibility of the Timoshenko theory to describe the compliant mechanism undergoing shear deformation.

2. The error of tip position and angle made by the Euler-Bernoulli theory.

3. A qualitative evaluation differences between beam shapes undergoing shear or moment actuation.

Experimental Design: For the introduction of a tip shear force only, we mounted a transverse linear motor to the bearing seat on the mid of the crossbeam, see Fig.5.2 (p.45). The compliant mechanism was deflected to five different tip deflections, $v = 10, 20, 30, 40$ mm. At each deflection v, a picture was taken. To ensure no optical distortions, the pictures were taken with an aspect ratio of 1:1 of the highest possible focal length, here 42 mm. To compare the beam shapes, this procedure was repeated with moment actuation as well. Besides the tip angle θ and tip deflection v, tendon forces F_{ext5} were recorded. From this quantities, we computed the errors e_v and e_θ analogously to (6.5, p.64). Here, as the Euler-Bernoulli and the Timoshenko theory differ, we computed the model errors for both theories. Form the results, the SDE for equal tip forces and equal tip deflections were computed:

$$SDE = \left(1 + \frac{3\Gamma^2}{sr^2}\right), \quad SDE_F = \frac{v_{ts}(L)}{v_{eb}(L)}, \quad SDE_v = \frac{v'_{eb}(L)}{\theta_{ts}(L)}. \tag{6.7}$$

The error in x-direction was not computed, because in the case of shear deformation, the kinematic model established in (4.7, p.32) is not valid. To give a qualitative evaluation of the x position, we referred to the camera data.

Results Fig.6.10a (p.71) shows the the resulting errors for both theories. The tip deflection v was underestimated by 22% by the use of the Euler-Bernoulli theory. In contrary, for the Timoshenko theory, v was underestimated by 10%. Note that the angular errors $e_{\theta,eb}$ and $e_{\theta,ts}$ matched each other. Their maxiumum error was found to be -13%. Fig.6.10b (p.71) shows the experimentally determined SDEs, gained by (6.7), while the black line represents the theoretical SDE. The mean value of SDE_F was found to be 10% higher than the SDE. In contrast, SDE_v was underestimated by a mean value of 15%.
Fig.6.11 (p.72) helps in getting an feeling for the differences in beam shapes depending on the two load cases, tip moment only and tip shear force only.

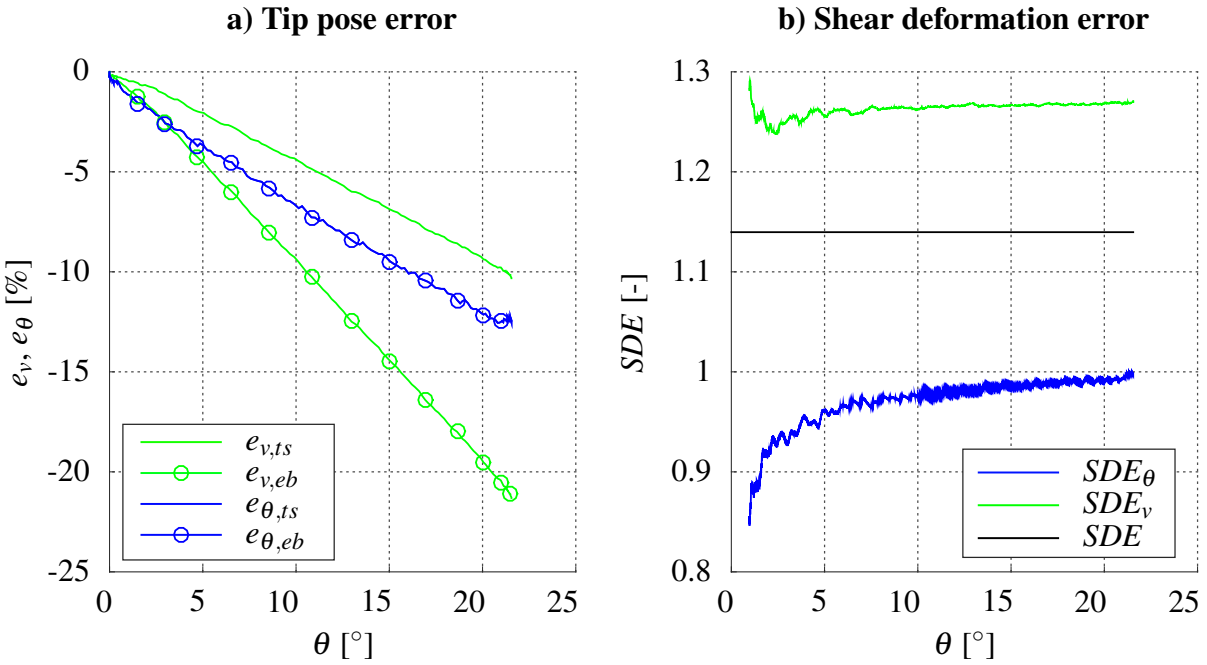

Figure 6.10: Model error for shear actuation. a) The tip angle θ and the lateral displacement v were underestimated by 10-12% with the Thimoshenko, theory. As explained below, we assumed, that this was an effect of tendon elasticity. b) Accordingly, SDE_v and SDE_F differed from the theoretical SDE.

Discussion Both θ and v are underestimated by the Thimoshenko beam theory. We will explain the reasons for this by the use of the equation for the tip angle under static lateral force, see (4.77):

$$\theta(L) = \frac{FL^2}{2EI}$$

Since I and L are geometric parameters, e_θ could only rise from the influence of force or the estimated Young's modulus. Since E was estimated beforehand and produced satisfying results for the experiments using a constant tip moment, we assume, that in this case, the error could only be due to the force F_{ext5}. As explained in (5.3.2, p.52), the shear actuation in the present testbed design does not require any additional pulleys within the tendon routing. Therefore, the effect of tendon and pulley friction is avoided. We concluded, that the error was due to tendon elasticity. Accordingly, SDE_v and SDE_F differed from the theoretical SDE.

Within a qualitative evaluation of Fig.6.11 (p.72) we assumed the curvature k for moment actuation as a constant, $k_m(s) = k_m(s+\Delta s)$. For the shear actuation it was found that $k_s(s) \neq +k(s+\Delta s)$.

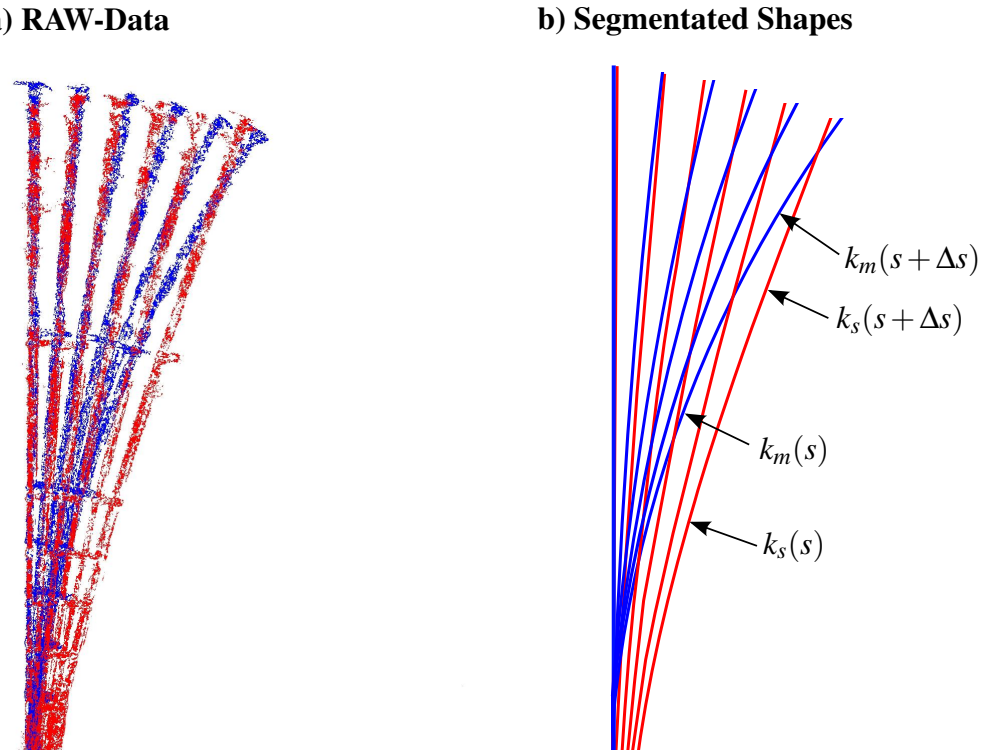

e

Figure 6.11: Difference in beam shapes for moment actuation (blue shape) and shear actuation (red shape). a) raw data gained from photographs with a aspect ratio of 1:1 and a focal length of 42 mm. b) Segmented forms of the beam shapes. While for the moment actuation, one could assume $k_m(s) = k_m(s+\Delta s)$, for the shear actuation it was found that $k_s(s) \neq k(s+\Delta s)$. Note that this is just a qualitative evaluation.

6.2 Accuracy of the Position Controller

Intention and Experimental Design: To evaluate the accuracy of the position controller proposed in (4.10, p.39), we commanded desired tip angles θ_d in steps of 5°and measured the actual positions of the actuating linear motor x_{LM} as well as the resulting tip position $\boldsymbol{p} = [v,x]^T$ and tip angle θ. The measurements were conducted at a mean deformation rate of 25 mm/s.

Results: Fig.6.12 shows the commanded tip angles as constants over time and the actual tip angle. The mean error between the two quantities was found to be 22%, see Tab.6.2 (p.74). Fig.6.13 (p.74) shows an exemplary presentation of the actuating linear motor positions for $\theta_d = 30°$. While x_d is the desired position, x_{LM} represents the actual position. x_{tend} was computed with the use of the measured tip angle and the equations established in (4.10, p.39). The mean error between x_d and x_{LM} was found to be 12%, the mean error between x_{LM} and x_{tend} was found to be 6%, see Tab.6.2 (p.74).

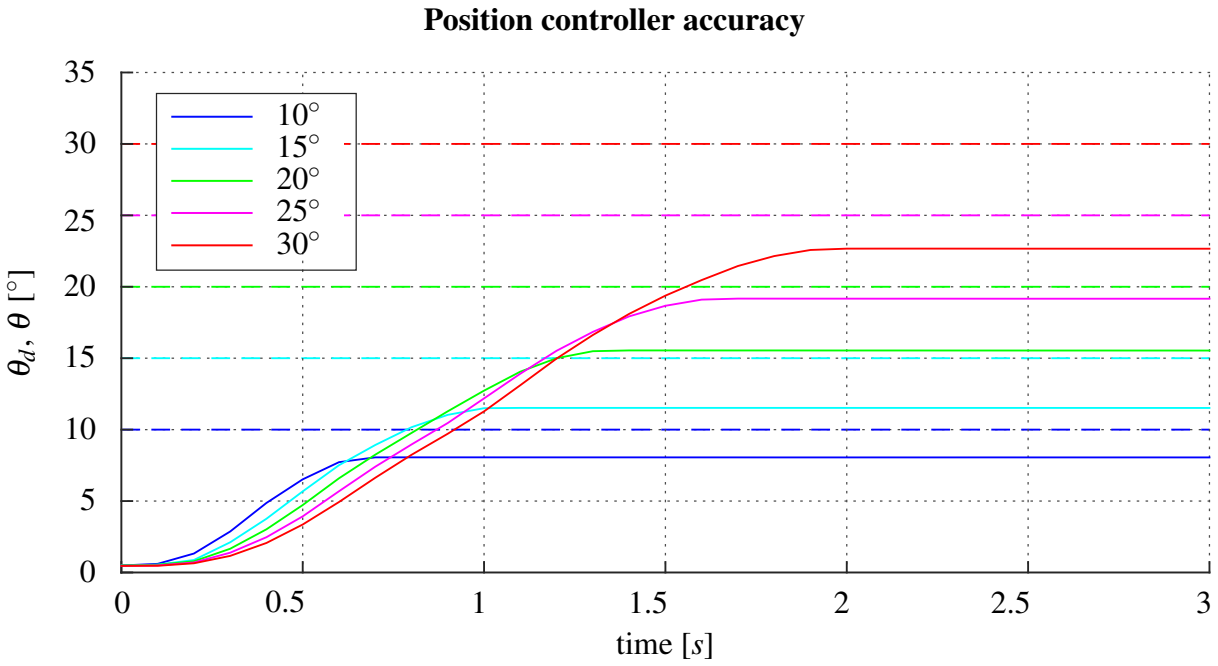

Figure 6.12: Position controller offset. The mean error of commanded angle θ_d and actual angle θ was 22%. See Tab.6.2 (p.74) for numerical results

Discussion: The accuracy of the proposed position controller was found to be 22%. One share of this error results from the CC approximation as we command θ_d and compute x_d by the use of CC, see (4.10, p.39). Further inaccuracies result from the steady state errors summarized in e_{SS} such as motor friction plus tendon elasticity. This error may be decreased by tuning the controller gains.

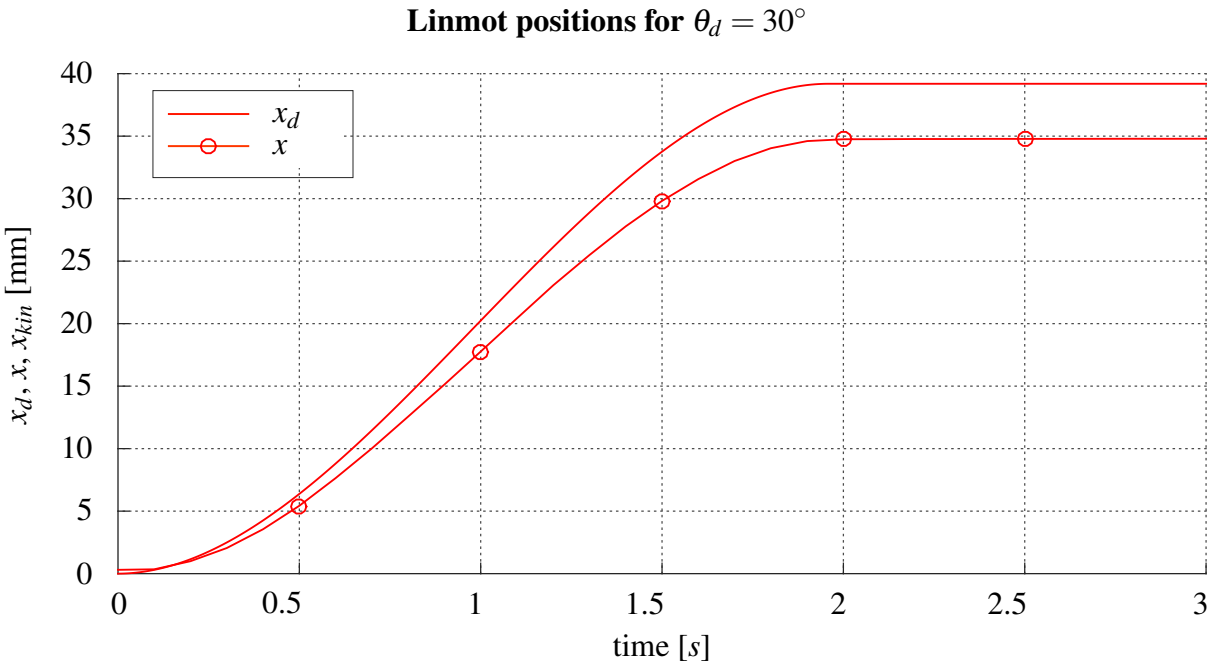

Figure 6.13: Exemplary presentation of the actuating linear motor positions for $\theta_d = 30°$. The offset between x_d and x_LM resulted from the steady state error. Errors between x_{LM} and x_{tend} result partly from CC approximation and tendon elasticity.

θ_d	e_{total}	θ	x_d	e_{SS}	x_{LM}
10°	19%	8.1°	13.6 mm	12%	12.0 mm
15°	23%	11.5°	20.3 mm	11%	18.0 mm
20°	23%	15.5°	26.8 mm	13%	23.4 mm
25°	23%	19.2°	33.1 mm	11%	29.4 mm
30°	24%	22.7°	39.2 mm	12%	34.5 mm

error by CC

static controller error

Table 6.2: Results for the position controller accuracy corresponding to Fig.6.12 and Fig.6.13.

6.3 Dynamic analysis

Intention and Experimental Design: As the evaluation of the compliant mechanism's dynamic behaviour was not covered within this work, in this section, we will just give a brief overview to get a feeling for the dynamic response and the damping coefficient ζ.
We commanded the linear motors to perform four chirp motions of different amplitudes and measured the resulting tip angle θ and the resulting actuation moment M. Using the measured quantities, we computed the dynamic response of the analytical model for different damping coefficients ζ and built the difference between the measured tip angle θ and the tip angle predicted by the model θ_{mod}.

Results: Fig.6.14 (p.76) shows the resulting error by the use of different damping coefficients ζ. For a critically damped system $\zeta = 1$ the resulting error reached a maximum of $\pm 3^\circ$. For $\zeta = 0.5$ as well as for the use of the static response, the maximum error was about $\pm 2^\circ$. For $\zeta = 0.2$ the maximum erro was about $\pm 1^\circ$

Discussion As the results showed, for fast motion, one has to consider the dynamic model for the beam equations. For $\zeta = 0.2$ the error was found to be the lowest and, therefore, we assume, that the exact damping properties of the compliant mechanism could be found around this value. Further work will be to investigate the dynamical behaviour in detail.

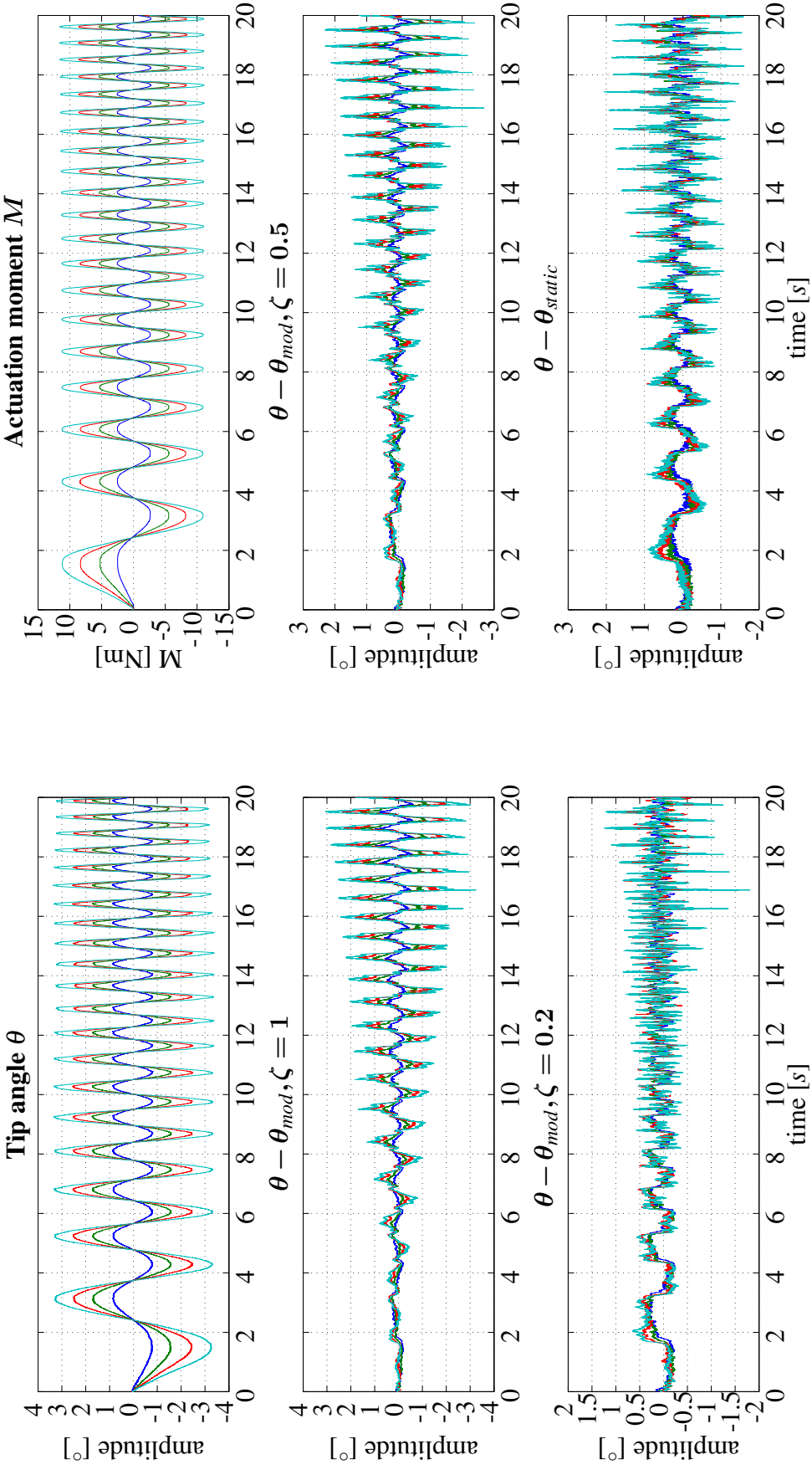

Figure 6.14: Coarse damping analysis of the compliant mechanism. The lowest error was encountered for $\zeta = 0.2$. Further work will be to investigate the dynamical behaviour in detail

7 Discussion

Within the present testbed, we were able to introduce a local moment and concentrated transverse shear force at the structures tip. As explained in (5.3, p.48), for actuating a continuous robot, the load case of a local tip moment is from mater. Therefore, our recommendations for the tesbed design and the discussion concerning the model accuracy refer to this load cases only. Following, we will summarize the Euler-Bernoulli and the Timoshenko beam theory under one definition, namely the classical beam theories. This is because for a tip moment, those two beam theories converge, see (4.7, p.35). Following, we will recapitulate the steps in building up the test bed and manufacturing the compliant mechanism, after which we will discuss the model validity in detail. Then, we will have a closer look on the possible improvements concerning the postion controller.

7.1 Design Recommendations for Testbed Improvements

7.1.1 Adhesion between the parts of the Compliant mechanism

One crucial issue for the compliant mechanism to work was the adhesion between continuum, mounting flange and crossbeam. Within the period of this work, we conducted about 100 cycles through the workspace with varying mean deformation rates and load cases including shear force and pretension. We encountered no problems concerning the adhesion between the parts and, objectively, we can recommend to use the principle of form closure to achieve good adhesion.

7.1.2 Manufacturing of Flange and Crossbeam

The flange and crossbeam mounted onto the compliant mechanism were manufactured using 3D-Printing with PLA as a filament. Rough calculations showed, that these structures were a lot stiffer than the continuum of the mechanism and, therefore, we assumed that crossbeam and flange will not experience any deformation. However, because of the slow cooling down of the PLA within the 3D-printing process, we encountered warping and stress within these parts. Inaccuracies while mounting the flange onto the testbed could result from this fact. Furthermore, unsymmetrical shape of the parts due to this warping could be perceptible. As a result, geometrical parameters such as the length of the lever arm l could differ from the CAD data. For future manufacturing, this wraping needs to be avoided.

7.1.3 Manufacturing of the Compliant Mechanism

As described in (5.2.2, p.47), we used MDF-plates to manufacture the mould on which we mounted the flange and crossbeam by the use of screw clamps. Then we filled the mould with the liquid elastomer, which were evacuated completely beforehand. However, when filling in the elastomer, air bubbles could have been trapped again in the continuum. Because of the

screw clamps occupied to much space, we were not able to put the mould into a vacuum furnace. Therefore, we could not ensure, that no air bubbles were trapped in the continuum, although we conducted the manufacturing process to the best of our knowledge. We recommend to design a space saving mould. Polyoxymethylene could be an interessting material because of its low surface energy [87]. This may result in an easy demoulding because of the reduced adhesion between the mould and the continuum.

7.1.4 Design of the Pulley units

As we saw in (6.1, p.57), we were able to predict the tip angle θ by the classical beam theories with satisfying accuracy. The maximum error for the tip angle $e\theta$ never exceeded 2%. Remember, that the tip angle for a concentrated actuation moment is derived by

$$\theta = \frac{ML}{EI}.$$

Since L and I are geometry parameters and E were identified within several test, see (5.4, p.52), we assumed, that every inaccuracy of θ is a result of a disturbance of the actuation moment. Remember the course of the error angle β and the one of e_θ, see Fig.6.1 (p.58) and Fig.6.5 (p.65). As they are the same in a qualitative sense, we took this as proof for our assumption. Regarding the accuracy of the results, we conclude, that pulley placement was good enough to ensure the introduction of a pure actuation moment for lower pretension. However, the pulley position brings several disadvantages which is why we will recommend a different design for the pulley units. See Fig.7.1a for a schematic drawing of the actual pulley position. Since the linear motors were placed in vertical direction, we needed two pulleys to route the tendons probably. Because every single pulley was adjustable independently, this resulted in different pulley heights hr_L, hr_R and different distances b, b_R. As well, we were not able to assume the same amount of friction of the four pulleys. We assume, that the directionality of the testbed was a result of this facts. Furthermore, the present pulley arrangement brought one more major disadvantage in terms of controlling the tip: when switching between the actuating and antagonistic mode, means one the actuating motor pulls while the antagonistic actuator follows, the neutral position represents an undefined state where the kinematic model fails. For this reasons, we recommend a pulley arrangement similar to the one as shown in Fig.7.1b. A horizontal placed linear motor allows the use of one pulley per tendon only. Therefore, we have defined friction and kinematic mapping. Another advantage of the redesigned pulley arrangement is, that the need of a gravity compensation for the slider's weight is avoided because the linear motors are placed horizontally. this also ensures the same initial angel θ_{init} for every experiment. Furthermore, there is an easy way to change the pulley height within the experiment, e.g. in terms of θ such that $hr = hr(\theta)$. As one can see, the place beneath the pulley, beforehand occupied by the linear motor, is now available. This gives the possibility to integrate a second linear motor or an actuated linear

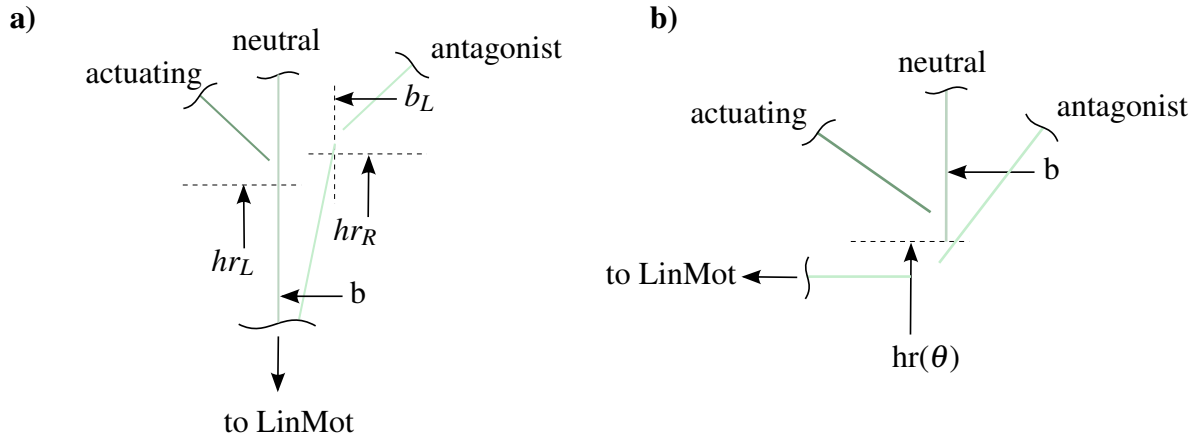

Figure 7.1: a): Pulley arrangement used in this work. The use of two pulleys per tendon results in different pulley positions and frictions for each the actuating and antagonistic mode of the actuator. Furthermore, at the neutral position, the state of the tendon is undefined, because it has no contact with any pulley. This may result in instabilities when controlling the compliant mechanism. b): Redesigned pulley arrangement. By placing the linear motor in a horizontal way, the tendon routing can be achieved by the use of one pulley only.

guidance to adjust the pulley's height.

7.2 Model validity and Further Investigations

As explained in (7.1.4, p.78), we encountered a relatively small error e_θ for the tip angle θ predicted by the classical beam theories. With this angle and the assumption of CC we were able to compute the tip position $\boldsymbol{p} = [v,x]^T$ with the use of (4.92). The maximum error between measured data and the CC approximation were found to be $e_v = 4\%$ for lateral displacement and $e_x = 12\%$ for the axial position. One reason for these errors may be geometrical inaccuracies made by the use of the CC assumption while undergoing load cases not covered in the present approach.

One method of investigating this approximation error could be the use of a beam structure, which is not compressible and underlies the Euler-Bernoulli theory. This is because in such a structure, shear and normal forces will not have any influences. With such a structure and the use of an appropriate pulley position one could ensure the introduction of an actuation moment only. Every occurring error in such an experiment could be assigned to inaccuracies resulting from the CC approximation. In this work, we designed a cantilever beam to use in such an experiment. It consists of a plate of stainless steel with a thickness of 1 mm, a length of 0.190 m and a width of 0.123 m. As the motor controllers where tuned to match the requirements of the compliant mechanism it was not trivial to test this cantilever beam on the present testbed. For reasons of time we shifted this work task to further work.

As mentioned above, the error e_x in axial direction was tree times as high as e_v. If these errors

only result from the CC approximation, one could assume, that they are at about the same value. Obviously they differ a lot and, therefore, normal forces not incorporated in the classical beam theories may play a role. The aforementioned experiment could also help in identifying those errors. The cantilever beam only underlies geometrical approximation errors, while the compliant mechanism includes every occurring error. As the geometries of these structures are similar in length and width, one could compute the difference in the errors, which could correspond to the error resulting from neglecting normal forces.

8 Conclusion

In the present work, we aimed to investigate the bending properties a compliant mechanism. Therefore, we established the equations of motion for both the Euler-Bernoulli and the Timoshenko beam theory, to allow for the use of comparatively thick beams with a low slenderness ratio *sr*. We showed, that for the actuation via tip moment only, there is no difference in the static responses for the Euler-Bernoulli and the Timoshenko theory. Furthermore, we introduced the SDE as a measurement of the statical failure between the classical beam theories undergoing shear. As a proof of the analytical solutions, we carried out a FEM analysis.

To allow for position control, we designed a position controller to command the tip angle θ. Therefore, we established a kinematic mapping between tip angle and actuator position with the use of the CC approximation for which we assumed validity when actuating via tip moment only.

A testbed was designed and built up to investigate statics and dynamics of one special mechanism under the load cases of a tip moment only and a transverse tip shear force. Material test were performed to evaluate the elastic properties of the compliant mechanism's continuum.

Within the experiments we were able to show a tip angel accuracy of 2% for the Timoshenko beam theory. With the use of the position controller, we were able to achieve an accuracy of 22%. We assume, that this failure could be reduced by tuning the controller gains and incorporate the tendon elasticity into to kinematic mapping.

Further work will be to evaluate other beam structures with different geometry and material. As well, a detailed dynamic analysis has to be carried out.

Bibliography

[1] W. M. Kier and K. K. Smith. Tongues, tentacles and trunks: The biomechanics of movement in muscular-hydrostats. *Zoological Journal of the Linnean Society*, 83:307–324, 1985.

[2] D. Trivedi, C. D. Rahn, W. M. Kier, and I. D. Walker. Soft robotics: Biological inspiration, state of the art, and future research. *Applied Bionics and Biomechanics*, 5:99–117, 2008.

[3] W. McMahan and B. A. Jones. Robotic manipulators inspired by cephalopod limbs. *Proceedings of the . . .*, 2011.

[4] R. J. Webster and B. A. Jones. Design and Kinematic Modeling of Constant Curvature Continuum Robots: A Review. *The International Journal of Robotics Research*, 29(13):1661–1683, June 2010.

[5] L. S. Cowan and I. D. Walker. Soft Continuum Robots-the Interaction of Continuous and Discrete Elements. In *ALIFE*, pages 126–133, 2008.

[6] N. Giri and I. Walker. Continuum robots and underactuated grasping. *Mechanical Sciences*, 2(1):51–58, February 2011.

[7] W. McMahan, V. Chitrakaran, M. Csencsits, D. Dawson, I. D. Walker, B. A. Jones, M. Pritts, D. Dienno, M. Grissom, and C. D. Rahn. Field trials and testing of the OctArm continuum manipulator. *Proceedings 2006 IEEE International Conference on Robotics and Automation, 2006. ICRA 2006.*, (May):2336–2341, 2006.

[8] B. Donald, L. Gariepy, and D. Rus. Distributed manipulation of multiple objects using ropes. In *Robotics and Automation, 2000. Proceedings. ICRA '00. IEEE International Conference on*, volume 1, pages 450–457, 2000.

[9] S. Hirose and M. Mori. Biologically inspired snake-like robots. *Robotics and Biomimetics, 2004. ROBIO . . .*, pages 1395–1422, 2004.

[10] C. Bergeles and G-Z. Yang. From passive tool holders to microsurgeons: safer, smaller, smarter surgical robots. *IEEE transactions on bio-medical engineering*, 61(5):1565–76, May 2014.

[11] I. A. Gravagne. Large deflection dynamics and control for planar continuum robots. *Mechatronics, IEEE/ASME . . .*, 8(2):299–307, 2003.

[12] K. Xu and N. Simaan. An investigation of the intrinsic force sensing capabilities of

continuum robots. *Robotics, IEEE Transactions on*, 24(3):576–587, 2008.

[13] U. Hagn, R. Konietschke, A. Tobergte, M. Nickl, S. Jörg, B. Kübler, G. Passig, M. Gröger, F. Fröhlich, U. Seibold, L. L. Tien, A. Albu-Schäffer, A. Nothhelfer, F. Hacker, M. Grebenstein, and G. Hirzinger. DLR MiroSurge: a versatile system for research in endoscopic telesurgery. *Int. J. Computer Assisted Radiology and Surgery*, 5(2):183–193, 2010.

[14] P. A. Garber and J. A. Rehg. The ecological role of the prehensile tail in white-faced capuchins (Cebus capucinus). *American Journal of Physical Anthropology*, 110(3):325–339, 1999.

[15] M. H. Raibert. *Legged robots that balance*. MIT press, 1986.

[16] Festo AG. BionicKangaroo - energieeffiziente Sprungkinematik nach natürlichem Vorbild @ONLINE, 2014.

[17] R. Cieslak and A. Morecki. Elephant trunk type elastic manipulator-a tool for bulk and liquid materials transportation. *Robotica*, (September 2000):11–16, 1999.

[18] R. V. Bostelman, J. S. Albus, and R. E. Graham. Robocrane and EMMA applied to waste storage tank remediation. *... Nucelar Society Seventh ...*, pages 1–6, 1997.

[19] G. Immega and K. Antonelli. The KSI Tentacle Manipulator. In *ICRA*, pages 3149–3154. IEEE Computer Society, 1995.

[20] F. Köckerling and W. Feil, editors. *Video-endoskopische Chirurgie : Grundlagen - Prinzipien - Perspektiven*. Barth, Heidelberg [u.a.], 1998.

[21] G. Chen, M. T. Pham, and T. Redarce. A semi-autonomous micro-robotic system for Colonoscopy. *Robotics and Biomimetics, ...*, pages 703–708, 2009.

[22] G. Chen, M. T. Pham, and T. Redarce. Development and kinematic analysis of a silicone-rubber bending tip for colonoscopy. *Intelligent Robots and Systems ...*, pages 168–173, 2006.

[23] G. Robinson and J. B. C. Davies. Continuum robots-a state of the art. *Robotics and Automation, 1999. ...*, 4(May):2849–2854, 1999.

[24] R. J. Webster and B. A. Jones. Design and kinematic modeling of constant curvature continuum robots: A review. *The International Journal of Robotics Research*, 2010.

[25] S. Haddadin, A. Albu-Schäffer, and G. Hirzinger. Safety Evaluation of Physical Human-Robot Interaction via Crash-Testing. In *Robotics: Science and Systems*, volume 3, pages 217–224. 2007.

[26] S. Haddadin, A. Albu-Schaffer, A. De Luca, and G. Hirzinger. Collision detection and reaction: A contribution to safe physical human-robot interaction. In *Intelligent Robots and Systems, 2008. IROS 2008. IEEE/RSJ International Conference on*, pages 3356–3363. IEEE, 2008.

[27] S. Haddadin, A. Albu-Schäffer, and G. Hirzinger. Requirements for safe robots: Measurements, analysis and new insights. *The International Journal of Robotics Research*, 28(11-12):1507–1527, 2009.

[28] G. Kunad, J. Mueglitz, P. Dautzenberg, and B. Neisius. Getriebebewegliche Instrumente fuer die Minimal Invasive Chirurgie. Technical report, 1994.

[29] A. Wimmer, B. Deutschmann, B. Kuebler, C. Rink, and G. Hirzinger. Spine-kinematics with constraint guidance for robot supported MIS-instruments. In *Robotics and Automation (ICRA), 2013 IEEE International Conference on*, pages 5453–5460, May 2013.

[30] V. C. Anderson. Tensor arm manipulator. *US Patent 3,497,083*, 1970.

[31] M. E. Rosheim. *Robot evolution*. 1994.

[32] D .B. Camarillo, C. F. Milne, C. R. Carlson, M. R. Zinn, and J. K. Salisbury. Mechanics Modeling of Tendon-Driven Continuum Manipulators. *IEEE Transactions on Robotics*, 24(6):1262–1273, December 2008.

[33] Y. Fu, X. Li, and Sh. Wang. Research on the axis shape of an active catheter. *The International Journal of . . .* , 4(1):69–76, 2008.

[34] T. Fukuda, K. Kosuge, F. Arai, M. Negoro, and K. Nakabayashi. Micro active catheter system with multi degrees of freedom. *Proceedings of the 1994 IEEE International Conference on Robotics and Automation*, pages 2290–2295, 1994.

[35] I. D. Walker, C. Carreras, R. McDonnell, and G. Grimes. Extension versus bending for continuum robots. *International Journal of Advanced Robotic Systems*, 3(2):171–178, 2006.

[36] Harvard Biodesign Lab. Soft Robotics@ONLINE.

[37] R. J. Webster, J. M. Romano, and N. J. Cowan. Mechanics of Precurved-Tube Continuum Robots. *IEEE Transactions on Robotics*, 25(1):67–78, 2009.

[38] M. Rolf and J.J. Steil. Constant curvature continuum kinematics as fast approximate model for the Bionic Handling Assistant. *2012 IEEE/RSJ International Conference on Intelligent Robots and Systems*, pages 3440–3446, October 2012.

[39] S. Neppalli and B. A. Jones. Design, construction, and analysis of a continuum robot. In *IROS*, pages 1503–1507. IEEE, 2007.

[40] B. A. Jones and I. D. Walker. Practical Kinematics for Real-Time Implementation of Continuum Robots. *IEEE Transactions on Robotics*, 22(6):1087–1099, December 2006.

[41] B. A. Jones, W. McMahan, and I. D. Walker. Practical Kinematics for Real-time Implementation of Continuum Robots. In *ICRA*, pages 1840–1847. IEEE, 2006.

[42] S. Iqbal, S. Mohammed, and Y. Amirat. A guaranteed approach for kinematic analysis of continuum robot based catheter. *2009 IEEE International Conference on Robotics and Biomimetics (ROBIO)*, pages 1573–1578, December 2009.

[43] M. W. Hannan and I. D. Walker. Novel kinematics for continuum robots. *Advances in Robot Kinematics*, pages 0–9, 2000.

[44] G. Immega and K. Antonelli. The KSI tentacle manipulator. *Proceedings of 1995 IEEE International Conference on Robotics and Automation*, 3:3149–3154, 1995.

[45] N. Simaan, R. Taylor, and P. Flint. A dexterous system for laryngeal surgery. *Robotics and Automation, 2004. . . .*, pages 351–357 Vol.1, 2004.

[46] N. Simaan, K. Xu, A. Kapoor, W. Wei, P. Kazanzides, P. Flint, and R. Taylor. Design and Integration of a Telerobotic System for Minimally Invasive Surgery of the Throat. *The International journal of robotics research*, 28(9):1134–1153, September 2009.

[47] W. McMahan, B. A. Jones, and I. D. Walker. Design and implementation of a multi-section continuum robot: Air-Octor. *2005 IEEE/RSJ International Conference on Intelligent Robots and Systems*, pages 2578–2585, 2005.

[48] B. A. Jones and I. D. Walker. Kinematics for multisection continuum robots. *IEEE Transactions on Robotics*, 22(1):43–55, February 2006.

[49] D. B. Camarillo, C. R. Carlson, and J. K. Salisbury. Configuration Tracking for Continuum

Manipulators With Coupled Tendon Drive. *IEEE Transactions on Robotics*, 25(4):798–808, August 2009.

[50] A. De Donno, F. Nageotte, Ph. Zanne, L. Zorn, and M. de Mathelin. Master/slave control of flexible instruments for minimally invasive surgery. *2013 IEEE/RSJ International Conference on Intelligent Robots and Systems*, pages 483–489, November 2013.

[51] A. De Donno, F. Nageotte, Ph. Zanne, L. Zorn, and M. de Mathelin. Introducing STRAS: A new flexible robotic system for minimally invasive surgery. *2013 IEEE International Conference on Robotics and Automation*, pages 1213–1220, May 2013.

[52] C. V. Riga, C. D. Bicknell, D. Wallace, M. Hamady, and N. Cheshire. The role of robotic endovascular catheters in fenestrated stent grafting. *Journal of Vascular Surgery*, 51(4):810–820, 2010.

[53] A. Degani, H. Choset, A. Wolf, and M. A. Zenati. Highly Articulated Robotic Probe for Minimally Invasive Surgery. In *ICRA*, pages 4167–4172. IEEE, 2006.

[54] P. Neuzil, S. Cerny S. Kralovec O. Svanidze J. Bohuslavec. Single-site access robot-assisted epicardial mapping with a snake robot: preparation and Wrst clinical experience. *J Robot Surg*, 7(2):102–111, 2012.

[55] P. Dario and M. C. Carrozza. A novel mechatronic tool for computer-assisted arthroscopy. *... in Biomedicine, IEEE ...*, 4(1):15–29, 2000.

[56] Y. Ganji, F. Janabi-Sharifi, and A. N. Cheema. Robot-assisted catheter manipulation for intracardiac navigation. *International journal of computer assisted radiology and surgery*, 4(4):307–15, June 2009.

[57] C. V. Riga, C. D. Bicknell, D. Wallace, M. Hamady, and N. Cheshire. Initial clinical application of a robotically steerable catheter system in endovascular aneurysm repair. *Journal of Endovascular Therapy*, 16(2):149–153, 2009.

[58] C. V. Riga, C. D. Bicknell, D. Wallace, M. Hamady, and N. Cheshire. Robot-assisted antegrade in-situ fenestrated stent grafting. *Cardiovasc Intervent Radiol*, 32(3):522–4, May 2009.

[59] Y. Haga, Y. Tanahashi, and M. Esashi. Small diameter active catheter using shape memory alloy. *Micro Electro Mechanical ...*, 1998.

[60] A. B. Lumsden, J. E. Anaya-Ayala, I. Birnbaum, M. G. Davies, J. Bismuth, Z. F. Cheema,

H. F. El Sayed, H. Seethamraju, M. Loebe, and M. Valderrabano. Robot-assisted stenting of a high-grade anastomotic pulmonary artery stenosis following single lung transplantation. *Journal of Endovascular Therapy*, 17(5):612–616, 2010.

[61] D. M. Balfe. Dysphagia after laryngeal surgery: Radiologic assessment. *Dysphagia*, 5(1):20–34, 1990.

[62] ASHA. Swallowing Problems (Dysphagia) After Head and Neck Cancer @ONLINE.

[63] R. Goldman, P. Allen, D. Fowler, and N. Simaan. Design, simulation and evaluation of kinematic alternatives for Insertable Robotic Effectors Platforms in Single Port Access Surgery. *2010 IEEE International Conference on Robotics and Automation*, pages 1053–1058, May 2010.

[64] A. De Donno, F. Nageotte, Ph. Zanne, L. Zorn, and M. de Mathelin. Introducing STRAS: A new flexible robotic system for minimally invasive surgery. In *ICRA*, pages 1213–1220. IEEE, 2013.

[65] S. A. Stuart. Nonlinear problems of elasticity. *Applied Mathematical Sciences*, 2.

[66] S. M. Han, H. Benaroya, and T. Wei. Dynamics of transversely vibrating beams using four engineering theories. *Journal of Sound and Vibration*, 225:935–988, 1999.

[67] S. P. Timoshenko. LXVI. On the correction for shear of the differential equation for transverse vibrations of prismatic bars. *..., and Dublin Philosophical Magazine and Journal ...*, pages 1–3, 1921.

[68] D. Gross, W. Hauger, J. Schröder, and W. A. Wall. *Technische Mechanik*. Springer-Lehrbuch. Springer, 2009.

[69] J. Gere and B. Goodno. *Mechanics of Materials*. Cengage Learning, 2012.

[70] A. E. H. Love. *A Treatise on the Mathematical Theory of Elasticity*. Cambridge University Press, 2013.

[71] R. D. Mindlin and H. Deresiewicz. Timoshenko's shear coefficient for flexural vibrations of beams. Technical report, DTIC Document, 1953.

[72] N. G. Stephen and M. Levinson. A second order beam theory. *Journal of Sound and Vibration*, 67:293–305, 1979.

[73] J. Honerkamp and H. Roemer. *Klassische theoretische physik*. Springer-Lehrbuch. Springer, Berlin u.a., 3., durchges. und erw. aufl. edition, 1993.

[74] L. Landau and Lifschitz J. M. *Lehrbuch der theoretischen Physik - Band 1: Mechanik*. Harri Deutsch, Harri Deutsch, 14 auflage. edition, 2007.

[75] K. Meyberg and Vachenauer P. *Höhere Mathematik - Differentialgleichungen, Funktionentheorie, Fourier-Analysis, Variationsrechnung*. Springer-Lehrbuch. Springer, Berlin [u.a.], 4., korrigierte aufl., 2. korrigierter nachdr. edition, 2006.

[76] W. Nolting. *Grundkurs theoretische Physik2: Analytische Mechanik*. Springer, Berlin [u.a.], 2011. Elektronische Ressource.

[77] R. Haberman. *Elementary applied partial differential equations*. Prentice Hall Englewood Cliff, NJ, 1983.

[78] A. Labuschagne, N. F. J. van Rensburg, and A. J. van der Merwe. Comparison of linear beam theories. *Mathematical and Computer Modelling*, 49(1-2):20–30, 2009.

[79] N. F. J. van Rensburg and A. J. van der Merwe. Natural frequencies and modes of a Timoshenko beam. *Wave Motion*, 44(1):58–69, 2006.

[80] H. Dubbel. *Taschenbuch für den Maschinenbau*. J. Springer, 1914.

[81] G. R. Cowper. The Shear Coefficient in Timoshenko's Beam Theory. *Journal of Applied Mechanics*, 33(2):335–340, 1966.

[82] A. J. Davies. *The Finite Element Method: An Introduction with Partial Differential Equations*. Oxford Univ. Press, Oxford [u.a.], 2. ed. edition, 2011.

[83] Y. W. Kwon and H. Bang. *The finite element method using MATLAB*. CRC press, 2000.

[84] W. Thomson. *Theory of Vibration with Applications*. Taylor & Francis, 1996.

[85] S. C. Jacobsen, H. Ko, E. K. Iversen, and C. C. Davis. Antagonistic control of a tendon driven manipulator. In *Robotics and Automation, 1989. Proceedings., 1989 IEEE International Conference on*, pages 1334–1339. IEEE, 1989.

[86] J. Reinecke, M. Chalon, W. Friedl, and M. Grebenstein. Guiding effects and friction modeling for tendon driven systems. In *Robotics and Automation (ICRA), 2014 IEEE International Conference on*, pages 6726–6732, May 2014.

[87] E. Wintermantel and S. W. Ha. *Medizintechnik: Interdisziplinarität, Biokompatibilität, Technologien, Implantate, Diagnostik, Werkstoffe, Business ; mit 200 Tabellen*. Springer, Berlin [u.a.], 4., überarb. und erw. aufl. edition, 2008.

[88] A. Frick and C. Stern. *Praktische Kunststoffprüfung*. Hanser, München, 2011.

[89] G. Menges, E. Haberstroh, and W. Michaeli. *Menges Werkstoffkunde Kunststoffe*. Hanser, München, 6. aufl. edition, 2011.

List of Figures

List of Tables